Electrostatically-Driven Dust Lofting and Migration on Small Bodies

by

Kristin D. Nichols

B.S., Texas A&M University, 2013

M.S., Texas A&M University, 2015

A thesis submitted to the

Faculty of the Graduate School of the

University of Colorado in partial fulfillment

of the requirement for the degree of

Doctor of Philosophy

Department of Aerospace Engineering Sciences

2021

Committee Members:

Dr. Daniel Scheeres

Dr. Christine Hartzell

Dr. Delores Knipp

Dr. Jay McMahon

Dr. Zoltan Sternovsky

Nichols, Kristin D. (Ph.D., Aerospace Engineering Sciences)

Electrostatically-Driven Dust Lofting and Migration on Small Bodies

Thesis directed by Dr. Daniel J. Scheeres

Electrostatic dust lofting may be a common occurrence on small bodies in the Solar System, whereby the upward electrostatic force on a grain overcomes the gravity and cohesion binding it to the surface. This phenomenon may redistribute and transport dust across the surface to produce features such as the dust ponds on Eros, or even to rid bodies of small particles completely. Classical models, which distribute charge evenly across a dust grain, predict electric field strengths which are insufficient to loft dust. However, recent studies have developed grain-scale charging models which assume unequal distribution of charge on a dust grain and account for the buildup of charge in the microcavities of regolith. These models predict electric field strengths orders of magnitude larger than classical models, which may explain how electrostatic dust lofting occurs.

This thesis extends the most recent experimental results and grain-scale simulations to a global, comprehensive small body environment to better understand the complex interactions affecting electrostatically-driven dust motion on small bodies. Specifically, this thesis develops a method of bounding initial grain parameters (charge and velocity) and surface conditions (regolith cohesion) which lead to electrostatic lofting using new grain-scale supercharging models. A survey of electrostatic lofting requirements and behaviors on asteroids such as Bennu, Itokawa, Ryugu, and Eros is performed using a three-dimensional small body environment model which accounts for a complex gravity field, solar radiation pressure, and electrostatics from the near-surface plasma sheath. Simulation results show that past periods of faster rotation may have depleted small particle populations from bodies such as Bennu and Ryugu. Additionally, there is a strong correlation of higher particle mobility and escape at lower solar elevation angles, implying that dustier times of

day exist in the morning and evening near the terminator regions. Finally, we find a preferential loss of small particles on smaller rubble-pile asteroids such as Bennu, Itokawa, and Ryugu, contrasted with retainment of these same particles on larger bodies such as Eros. Overall, this work informs future efforts which aim to better understand, model, predict, and observe electrostatic dust behavior on small bodies in the Solar System.

Acknowledgements

I would like to thank my advisor, Dr. Dan Scheeres, for navigating me in this journey to completing my Ph.D. Although there were several obstacles along the way, Dr. Scheeres's patience, expertise, connections, and guidance allowed me to finish my research and contribute to the asteroid community in a meaningful way.

I would like to also thank my committee: Dr. Christine Hartzell, Dr. Delores Knipp, Dr. Jay McMahon, and Dr. Zoltan Sternovsky for their persistent questions and feedback in an effort to make my work the best it could be.

A special thanks to Dr. Mike Zimmerman at the Johns Hopkins Applied Physics Laboratory, without whose discussions over the past five years, I would not have the understanding of plasma physics and grain-scale supercharging required of this research.

I would also like to thank Dan Mazanek and the NASA Space Technology Research Fellowship program for supporting me and my work financially. The connections made and lessons learned while participating in visiting technologist experiences will serve me for the rest of my career.

I would also like to thank Dr. Conor Benson, who began as a fellow graduate student but quickly became a dear friend as we both walked through the highs and lows of our Ph.D. programs together. Thank you for always listening to my sometimes silly questions and for reminding me of the fundamentals.

I'd also like to thank my husband, Allen Ream, for supporting me emotionally, mentally, and sometimes financially through this program. Our hikes, camping trips, and late nights watching Star Trek got me through some of the toughest times of this program.

I will forever be grateful for his patience and support as we put our lives on hold so that I could finish my degree, and look forward to beginning the next phase of our life together.

And finally I'd like to thank my parents, Kim and David Nichols, for their unwaivering support throughout the years, and for always giving me the best opportunities to learn, grow, and succeed through all the stages of my life.

Contents

Chapter

Tables

Table

Figures

Figure

Chapter 1

Introduction and Motivation

Increasingly over the past decade, scientific interest in asteroids and comets has led to the development of mission architectures for both robotic and crewed missions to explore these small primordial bodies. Such exploration helps scientists trace the history and evolution of the Solar System and possibly the origin of life on Earth. While missions to small bodies have traditionally been fly-by trajectories, recent missions have increasingly attempted to interact with the target body. In 2001 the NEAR spacecraft approached and landed on Eros, demonstrating for the first time the ability to navigate a descent to the surface of a small body. In 2005, Japan's Hayabusa spacecraft became the first to make a touch and go landing on an asteroid (Itokawa) to capture a sample for return to Earth. In 2018, Japan's Hayabusa2 spacecraft deployed rovers onto the surface of Ryugu and later used a kinetic penetrator to collect pristine regolith samples for return to Earth. Most recently, the OSIRIS-REx spacecraft touched down on asteroid Bennu in 2020 to collect surfaces samples for Earth return. Thus, it is becoming increasingly important to understand not only how dust dynamics shape the natural evolution of the body from a scientific perspective, but also how the dusty charged environment affects mission operations near the surface.

Understanding the dusty environments found at small bodies and moons has been a compelling area of research since the Lunar Horizon Glow was first observed during the Surveyor missions [37]. Seen as the spacecraft passed through local sunset, the Lunar Horizon Glow was thought to be caused by sunlight scattering off 10 micron particles hovering just above the lunar surface. Similar observations of light streaks above the lunar

horizon, or 'lunar streamers', were made by the Apollo astronauts [63]. Additionally, the Lunar Ejecta and Micrometeoroid (LEAM) instrument placed during the Apollo 17 mission recorded anomalous particle impacts near sunrise and sunset on the Moon [2]. After ruling out micrometeoroid bombardment as the sole contributor of such particles due to the high flux of grains observed, scientists hypothesized that electrostatic lofting from the surface could be an additional source of dust transport there [37]. While several studies since then have attempted to find the lunar cloud of lofted dust [1, 11, 15, 56], none have found that electrostatic dust transport was the cause of these observations. Nonetheless, observations such as these led scientists to examine the conditions under which electrostatic transport of dust can occur, and how it may shape the natural evolution of small bodies in the Solar System. Furthermore, exploration activities will undoubtedly disturb dust from the surface. Understanding the implications of this dusty environment and how best to operate in it during exploration missions, is key to meeting both scientific objectives and safety standards.

The surfaces of airless bodies such as the Moon and asteroids charge through interaction with the solar wind plasma and ultraviolet radiation from the Sun. The daysides of these bodies are generally positively charged due to the dominance of photoemission at the surface. Electrons from photoemission of the surface material are preferentially attracted back to the positively charged surface. As a result, there is a higher density of photoelectrons near the surface, causing a separation of charge in the region referred to as a plasma sheath. This electron density decreases with distance from the surface until it equals that of the ions to form a neutral plasma and gives rise to an electric field directed away from the surface.

A dust grain on the surface will charge due to currents from the plasma sheath, solar wind, and its own photoemission. Charged dust grains on the surface will thus feel an electrostatic force equal to the product of the dust grain charge and the local electric field

strength. Both the charge of the grain and the electric field will vary as a function of time and altitude (as the characteristics of the plasma environment change). Because the surface gravity is so low on the Moon and small bodies, some dust grains are able to electrostatically loft. Electrostatic lofting occurs when the upward electrostatic force on the dust grain is able to overcome the downward forces of gravity and cohesion holding it to the surface. In this way, electrostatically-driven dust motion is thought to be a source of regolith redistribution across and off the surfaces of small bodies.

Electrostatic dust lofting was first theorized to occur on the Moon [37]. However, given the lower surface gravity on asteroids, comets, and smaller moons, it was only natural to expect this phenomenon to occur on these bodies as well [29]. The most notable finding of such behavior is observation of the dust ponds at Eros. Believed to be pools of finer regolith at the bottom of craters, these ponded dust deposits are thought to be the products of preferential lofting and transport of small dust grains by electrostatic forces [38]. In contrast, no fine regolith is observed on the surfaces of rubble pile asteroids such as Itokawa, Bennu, and Ryugu [13, 28, 52], which may be linked to small particle depletion in the bodies' past.

Without definitive observational evidence, scientists turned to experimentation and numerical simulation to study the phenomena of electrostatic dust transport. Through various studies, electrostatically-driven dust motion has been shown to be extremely sensitive to initial conditions [7, 27, 29, 31]. As newer models emerge, dust lofting requirements are re-examined to determine initial dust parameters such as grain charge and ejection speed. One of the primary challenges in understanding electrostatic lofting and determining realistic lofting requirements has been modeling the electrostatic force. Hartzell and Scheeres [19] showed that the electric field strength thought to exist on the surface of small bodies is insufficient to loft dust grains, and thus some additional level of charging is necessary. Cohesion, in particular, appears to be a significant limiting factor in

determining which populations of grains can loft [21]. While classical shared charge models are unable to explain electrostatic lofting, newer patched charge models, which distribute charge unequally on the surface of a grain and account for charge buildup in the microcavities between grains, may be able to. These newer models predict grain-scale electric fields and charges that are orders of magnitude larger than classical predictions [44, 51]. Such magnitudes lead to larger electrostatic forces that enable dust grains to overcome the gravitational and cohesive forces binding them to the surface. Perhaps most interestingly, these studies show that the individually-lofted dust grains carry a negative charge [44], in contrast to the previous widely-held belief that dust grains were positively charged like the sunlit surface of the body they loft from. Overall, these newer experimental results by Wang et al. [51] and Schwann et al. [44], as well as the grain-scale simulations by Zimmerman et al. [62] show that such patched charge grain-scale models can explain how dust grains become lofted on small airless bodies.

Given the recent advancements in our understanding of electrostatic dust lofting in controlled laboratory settings, there exists a need to extend and apply these experimental results to the study of electrostatically-driven dust motion in the near-surface environment of small bodies.

1.1 Focus and Contributions of Study

The study here not only aims to understand and explain the natural evolution of small bodies and moons, but to also examine how unnatural disturbances such as those caused by exploration activities affect mission operations in the near-surface region. Overall, my research extends the most recent experimental results and grain-scale simulations to a more global, comprehensive small body environment model to better understand the complex interactions affecting dust behavior on small bodies in the Solar System. Additionally, my work bounds initial condition requirements for electrostatic

lofting of dust grains given these new grain-scale supercharging models. This work informs future efforts which aim to better understand, model, predict and observe electrostatic dust behavior on small bodies. Key contributions of this thesis include:

- Development of a three-dimensional small body environment model, which accounts for the unique gravity field of complex shape models, perturbations due to solar radiation pressure with consideration to eclipsing scenarios, cohesion of grains resting in regolith of various strengths, and the near-surface electric field using a monotonically-decreasing plasma sheath.
- A method of bounding initial grain parameters and surface conditions which lead to electrostatic dust lofting using new grain-scale supercharging models.
- A survey of electrostatic dust lofting requirements and behavior on asteroids such as (25143) Itokawa, (101955) Bennu, (162173) Ryugu, and (433) Eros.
- Simulation results which show that past periods of faster rotation may have depleted small particle populations from bodies such as Bennu and Ryugu.
- Simulation results which show a strong correlation of higher particle mobility and escape with lower solar elevation angle, implying dustier times of day exist in the morning and evening near the terminator regions.
- Simulation results which show a preferential loss of small particles ($\leq$5 micron) on smaller and faster rotating bodies such as Bennu, Itokawa, and Ryugu, contrasted with retainment of these same smaller particles on larger bodies such as Eros.

1.2 Thesis Statement

The preceding discussion leads to the following thesis statement:

Electrostatically-driven dust motion is highly sensitive to grain initial conditions and the forces under which its motion is prescribed. New grain-scale supercharging models, which predict electric field strengths and grain charges orders of magnitude larger than

classical models, may explain how dust becomes lofted on small bodies in the Solar System. Such models can be used to develop more realistic initial conditions for electrostatically-lofted dust particles and can even be used to bound surface conditions from which dust lofting can occur. Once a grain has been lofted from the surface, there are several environmental factors affecting its motion. Development of a comprehensive small body environment model which includes perturbations from all relevant forces can provide a framework from which to simulate and better understand the complex interactions affecting grain behavior in the near-surface region. From analysis of these results, predictions can be made about different particle population behaviors at specific bodies of interest such as (25143) Itokawa, (101955) Bennu, (162173) Ryugu and (433) Eros. Implications gleaned from this work can be used to update our understanding of the natural evolution of small bodies, as well as to inform the design of future mission operations on these bodies.

1.3 Arrangement of Thesis

This thesis is organized as follows:

Chapter 2 provides a literature review of previous investigations into the nature and feasibility of electrostatic dust motion, as well as a review of observations on the Moon and asteroids which motivate study of this phenomena.

Chapter 3 covers development of the small body environment model used to simulate electrostatically-driven dust grains. Each of the relevant sub-models are described in detail, including the gravitational model, the solar radiation pressure model, the electric field model, and grain charging model.

Chapter 4 examines electrostatic lofting requirements and their role in bounding grain initial conditions at the surface of small bodies. An analysis of the grain-scale

supercharging models is presented and used to determine grain conditions such as initial charge, ejection speed, and maximum regolith cohesion.

Chapter 5 provides the results of dust particle simulations using the small body environment model from Chapter 3 and the initial conditions generated using the methods presented in Chapter 4 for lofted dust. Both spherical and complex shape models are used to study a variety of parameters affecting grain behavior, such as grin size, primary body size, primary body spin rate, and solar elevation angle at the surface. Predictions on the behaviors of different dust particle populations at specific bodies of interest are given.

Chapter 6 provides a brief summary of the work and results covered in this thesis and gives avenues for future work and development on this topic.

1.4 Publications

Below are a list of papers, presentations, and posters given while undertaking this thesis work.

1.4.1 Journal Papers

- Nichols, K. D., D. J. Scheeres. (In Revision) *Planetary Science Journal*, "Electrostatic Lofting on Spherical Asteroids at Various Spin Rates."
- Nichols, K. D., D. J. Scheeres. (Accepted) *Astrophysical Journal*, "Electrostatic Lofting Conditions for Supercharged Dust."
- Nichols, K. D., D. J. Scheeres. (In Preparation) *Icarus*, "A Survey of Electrostatic Dust Lofting on Itokawa, Ryugu, and Eros using Grain-Scale Supercharging."

1.4.2 Conferences

- Nichols, K. D., D. J. Scheeres. Sept 25-29, 2017. Adelaide, Australia. *International Astronautical Congress*, "Dust Environment Models for Asteroid Surface Operations." Paper and Presentation.
- Nichols, K. D., D. J. Scheeres. Jul 14-22, 2018. Pasadena, California. *Committee on Space Research*, "Dust Levitation Dynamics on Small Airless Bodies." Poster.

- Nichols, K. D., D. J. Scheeres. Mar 18-22, 2019. Houston, Texas. *Lunar and Planetary Science Conference*, "New Electrostatic Charge Models Show Dust Lofting at Ryugu and Bennu." Presentation.

- Nichols, K. D., D. J. Scheeres. Jan 25-Feb 4, 2021. Sydney, Australia. *Committee on Space Research*, "Electrostatically Lofted Dust Behavior on Asteroids at Various Spin Rates and Primary Body Sizes." Presentation.

Chapter 2

Literature Review

This chapter provides an overview of relevant observational evidence, experimental results, and numerical studies pertaining to electrostatic dust lofting. The first and second sections detail observations and numerical simulations on the Moon and asteroids, respectively. Observational evidence remains the driving motivation for studying this phenomenon, while numerical simulations attempt to better understand the conditions under which it occurs and to replicate observations found in nature. The third section outlines experimental investigations which prove feasibility of electrostatically-driven dust motion in controlled environments. The final section gives the most recent advancements in the field, particularly with regard to the newer charge models, and provides both experimental and numerical simulation studies.

2.1 Lunar Observations and Numerical Simulations

Electrostatically-dominated movement of dust on the Moon has been theorized since the Surveyor spacecraft observed the Lunar Horizon Glow. Seen as a bright glowing crescent above the horizon as the spacecraft passed through local sunset, the glow was believed to be forward scattering of light by dust particles 5 to 10 microns in size hovering just above the surface [37]. Calculations of the particle flux due to micrometeoroid bombardment were not sufficient to explain the observed density of grains, and so electrostatic lofting was hypothesized to be responsible for the discrepancy. Later analysis of the Surveyor data by Glenar et al. [14] found that only one of the five observations could be confirmed as a type of horizon glow.

Similar to the Lunar Horizon Glow, Apollo 17 astronauts observed 'lunar streamers' or streaks of light roughly 5 to 10 kilometers above the lunar surface [63]. These observations were recorded in astronaut sketches and thought to be electrostatically-lofted dust particles (0.2 microns in diameter) at high altitudes. However, many investigations into this observed lunar dust cloud have found no evidence of its long-term existence [1, 11, 15, 56].

Further evidence was provided during the Apollo program when the Lunar Ejecta and Micrometeoroid (LEAM) instrument detected the highest flux of particle impacts at lunar sunrise and sunset. While the instrument was designed to detect cosmic dust particles, anomalous recordings of increased flux earlier and later in the day were interpreted as electrostatically-lofted dust grains reimpacting the surface [2].

Numerical study of these observations began with Criswell and De [8, 9] who studied the electrostatic environment near the terminator region of the Moon. They believed that the terminator region would be a likely place of electrostatic lofting because of the larger electric fields predicted to exist there due to the close proximity of sunlit and shadowed patches. Using a simple numerical model to calculate the electric field near a small rock partially in sunlight and partially in shadow (centimeter-sized variation)—both for the static and moving shadow case—they found fields strengths of up to 1000 V/m. Theoretically, this field strength would be sufficient to loft smaller dust particles such as those observed in the Lunar Horizon Glow. However, this value of the electric field is now believed to be an optimistic upper bound because neutralizing currents were neglected in their model. While modern simulations have shown a much more benign charging environments near the terminator [33, 36], Criswell and De's initial study inspired many others to follow.

Poppe and Horányi [34] studied the lunar plasma sheath using a 1D Particle-In-Cell (PIC) code with a non-Maxwellian distribution of photoelectrons. Assuming constant

gravity and discretized grain charging, they found dust levitation to occur. Evidence was also found for a non-monotonic plasma sheath above the lunar surface using a PIC code with measurements of the plasma potential from the Lunar Prospector mission [35].

While definitive evidence of electrostatic lofting of dust on the lunar surface appears to be weak, observations such as the Lunar Horizon Glow inspired scientists to explore the conditions under which electrostatically-driven dust motion can occur and how this type of dust transport may have shaped the natural evolution of the lunar surface.

2.2 Asteroid Observations and Numerical Simulations

Given the smaller mass of asteroids, it was natural to predict that electrostatic dust transport could also take place on these lower gravity bodies. Pascal Lee performed one of the first numerical studies of dust lofting on asteroids. Because asteroids tend to be deficient in dust grains ≤ 100 microns in size compared to lunar regolith, Lee performed a simple analysis to see if smaller grains could be preferentially lost by electrostatic lofting. Using a simplified model of gravity and electrostatics and neglecting cohesion and neutralizing currents, he found that electrostatic lofting was a viable means of redistributing regolith on the surface of asteroids [29]. However, he noted how sensitive the problem is to initial conditions and the models used, stating “the question lies perhaps more in the exact nature and intensity of the effects than in whether or not they occur” [29].

The first proper evidence of electrostatic dust transport on asteroids was the existence of ponded dust deposits observed on the surface of Eros by the NEAR Shoemaker space probe [38]. Because of their blue spectral signature (indicative of grains $\lesssim 50$ microns) and locations corresponding to regions of long terminator durations, these ponds were thought to be deposits of extremely fine dust grains that had been preferentially transported into craters via electrostatic lofting. Several numerical studies have since tested this theory [7, 27].

Colwell et al. [7] numerically simulated 2D dust lofting on the surface of Eros using a simplified, monotonically decreasing sheath potential model developed by Grard and Tunaley [16] and grain charging in a thermalized plasma by Havnes [24]. In the study, dust grains were launched over a range of arbitrary initial velocities and launch angles into the plasma sheath in the vicinity of a shadowed crater. Colwell et al. found that micron-sized particles were able to be levitated by the photoelectron layer and that there was a net transport of dust grains into shadowed regions, such as craters, where the electric field diminished.

Hughes et al. [27] extended the results of Colwell et al. [7] to three dimensions by launching particles in time-varying plasma sheaths over craters and other shadowed regions on the surface of Eros. Gravity was held constant in these simulations and the particle was given no charge at simulation start. Overall, they found that micron-sized grains were preferentially transported into craters, and that lofting of grains into topographic depressions occurred independent of stable levitation above the surface [27]. The authors noted that the "biggest source of uncertainty and the most important unknown" of the simulation were "the details of the electrostatic launching mechanism" [27]. Namely they put forth the next most important questions to be answered… "How do particles charge before they are launched? When and under what conditions are they most likely to launch? And how often is that launching likely to lead to stable levitation of a dust particle?" [27].

In contrast to Eros, in situ observations of the surfaces of Itokawa, Bennu, and Ryugu show no accumulation of fine dust grains [13, 28, 52]. These bodies are much smaller and less massive than Eros, which appears to play a role in dust grain transport across and off their surfaces. Additionally, past periods of faster rotation may provide insight into the current day surface conditions of smaller rubble-pile asteroids such as Bennu and Ryugu [25].

Nitter et al. [31] developed a more complex numerical model that describes the photoelectron sheath above the surface of a body using three possible variations in the potential profile and incorporates dust charging in an unthermalized plasma. Solving for the equilibrium charges of various particles on the surface of an asteroid, Nitter et al. simulated grain levitation in each of the sheaths modeled. However, they again noted the sensitivity of the problem to initial conditions, stating that "there are narrow ranges of dust particle size, initial charge, and initial velocity, which lead to suspension" [31]. And while they acknowledged the importance of grain properties, their study again neglected non-spherical grain shapes and the cohesive forces between the dust grain and the surface.

More recently, Hartzell and Scheeres [20] used the non-monotonic plasma sheath developed by Nitter et al. [31] to examine equilibrium heights and charges of levitating dust particles above the surface of the Moon, Eros, and Itokawa. Overall, they found that the grain velocities resulting in levitation are primarily influenced by grain size and not by the mass of the primary body or grain charge [20]. Additionally, Scheeres et al. [42] and Hartzell and Scheeres [19] showed analytically that cohesion is a particularly important factor to consider for the smallest grains on asteroids. When accounting for cohesion, gravity, and seismic shaking, the electric field strength required to loft micron-sized dust grains was shown to be dominated by cohesion and found to be at least an order of magnitude larger than the most optimistic estimates of the electric field in the lunar terminator region [19]. Thus, some additional source of charging is necessary to explain how dust lofting occurs.

2.3 Experimental Investigations

While electrostatic dust lofting hasn't been directly observed in situ on asteroids or the Moon, several terrestrial experiments have shown that it can occur under the right conditions. Sheridan et al. conducted one of the first experiments showing that electrostatic

lofting was possible [43]. In their experiment, a conducting sphere was covered in dust and rotated in a plasma with and without an electron beam. Individual dust grains were observed to jump off the surface when the plasma was turned on and increased in rate with an increase in the plasma density. Because dust shedding stopped when the plasma was turned off, it was concluded that the interaction between the dust grains and the plasma was responsible for the dust motion.

Sickafoose et al. [45] also performed studies on dust motion using an argon plasma sheath above a biased surface and found that many different types of particles levitate under a variety of plasma environments. In particular, they found that mechanical agitation was not necessary to loft grains if the plate potentials were high enough.

Wang et al. [50] modeled the light-dark terminator boundary of the lunar surface experimentally and found that the observed horizontal electric fields can be orders of magnitude larger than the vertical electric fields in the electron sheath above a photoemitting surface. Additionally, the progression of the light-dark boundary tends to increase the surface charge density of the lit surface as the region loses illumination (at least temporarily).

Experimental results by Hartzell et al. demonstrate the importance of cohesion in affecting the size of grains able to be electrostatically lofted [21]. In their experiment, Hartzell et al. [21] exposed a biased plate with piles of different sized grains to plasma and observed that intermediate-sized grains (15 micron) preferentially lofted due to their place between smaller grains (5 micron and 10 micron) dominated by cohesion and larger grains (20 micron and 25 micron) dominated by gravity. They showed that given a primary body and cohesive strength, there exists a grain size for which a minimum electric force is required for lofting [21].

2.4 Recent Advancements

From the experimental investigations and computational studies discussed, electrostatic dust lofting appears to be a viable phenomenon occurring on small bodies in the Solar System. However, as Hartzell and Scheeres [19] show, there is a discrepancy between the electric field strength required to launch particles and that thought to exist on the surfaces of small bodies, particularly when regolith cohesion is accounted for and dust grain charge is assumed to be uniformly distributed over the surface of each grain, as described by Gauss' law. Furthermore, given that dust lofting has been demonstrated experimentally, it is evident that some additional level of charging beyond that predicted by Gauss' law is needed to explain the observed electrostatic dust motion.

Recent studies suggest that newer charge models, which predict larger electric fields generated at the grain-scale, may be able to explain how dust becomes lofted on small bodies. Wang et al. [51] suggest a patched charge model, whereby charge from the emission and reabsorption of photoelectrons and/or secondary electrons is stored unevenly on the walls of microcavities formed between neighboring dust grains. This phenomenon was shown experimentally to generate unexpectedly large negative charges and significant grain-grain repulsive forces which enable dust to loft from the surface [51]. Zimmerman et al. [62] explores this theory of patched charge further by numerically simulating the grain-grain charging interactions. They find that the resulting grain-scale supercharging produces charge differences that exceed classical sheath predictions by several orders of magnitude, at times reaching the dielectric breakdown levels [62].

Even newer experimental results suggest that lofted particles only carry a negative charge, as opposed to the generally expected positive charge of photoemissive regolith [44]. In the experiment, dust particles were exposed to a variety of charging conditions, including a thermal plasma, electron beam, and ultraviolet radiation. To measure the polarity of the dust particles, positive and negative voltages were applied to a

gridded electrode above the dusty surface to attract charged particles; while a Faraday cup was used to measure the magnitudes of charges. The experiment showed that dust particles only detached from the surface when a positive voltage was applied to the electrode, indicating that lofted grains are negatively charged [44]. Additionally, no positive charges were recorded and measured charges were orders of magnitudes larger than those predicted using classical models [44]. These results align well with the patched charge model where large negative charge from photoelectrons and/or secondary electrons build up in the grain cavities [51].

Other studies such as Hood et al. [26] , Carrol et al. [6], and Orger et al. [32] investigate electrostatic dust lofting rates, which appear to slow over time, initial velocities, which appear to depend on a grain's shape, and dust lofting angles, which appear to have peak distribution at 45 degrees to the normal.

2.5 Summary

While observations such as the Lunar Horizon Glow on the Moon and ponded dust deposits on Eros suggest that electrostatically-driven dust motion may occur on small airless bodies, no direct proof of this phenomena have been made to date. Nonetheless, scientists have moved forward in an attempt to understand the conditions under which dust lofting can occur and the resulting effects of regolith redistribution on and off small body surfaces. Numerical studies have focused on replicating observations of dust at small bodies and developing better models of the plasma environment; while experimental studies have focused on proving that electrostatically-driven motion of dust is feasible. Additionally, experimental studies aim to measure what theory cannot explain—namely grain charging. In this way, theory and experimentation feedback into one another in an attempt to understand and explain observations of small body surfaces.

My research takes the newest advancements in grain-scale charging (both theoretical and experimental work) and applies them in a unique way to the study of dust transport and migration on small bodies. Using the results of our computational studies, we can make predictions about dust particle behavior and the surface conditions that allow electrostatic dust lofting to occur. These insights and predictions can then be tested by future missions making observations at these bodies.

Chapter 3

Small Body Environment Models

In this chapter, we develop the small body environment model (SBEM) which will be used to simulate dust grain lofting events in subsequent chapters. This comprehensive model, which accounts for all the relevant forces acting on a dust grain near the surface of a small body, is developed to better simulate, analyze, and understand the complex interactions affecting lofted dust behavior. The SBEM incorporates several individual models into a single simulation space, including a constant density polyhedron gravity model that accounts for complex shape models, a solar radiation pressure model that accounts for eclipsing scenarios, an electric field model that accounts for the near-surface plasma sheath generated on the dayside of an airless body, and a grain charging model that accounts for the various currents to and from a dust grain as it moves through the charged near-surface environment. Each of the separate models were implemented and verified separately before incorporation into the full SBEM model. In this way, as newer models are developed, they can be exchanged with older models in the SBEM. All the models are applied simultaneously to a single dust particle over a range of initial conditions (Chapter 4) to examine subsequent behavior and trends produced (Chapter 5). Each of the models are discussed in detail below, with the final dynamical equations of motion given at the end.

3.1 Gravitational Model

To account for the complex and irregular geometry of an asteroid, a constant density polyhedron model is implemented. In this model developed by Werner and Scheeres [53],

the small body is represented through a collection of vertices $\boldsymbol{P}_i$, edges $\mathcal{E}_{ij}$, and triangular facets $\mathcal{F}_{ijk}$. Given the position of a dust particle at a given time, the gravitational attraction it would feel from every point on the small body's surface is calculated. The equation for the potential function is given below, where the gravitational acceleration would simply be $\partial U/\partial \boldsymbol{r}$.

$$U(\boldsymbol{r}) = \frac{1}{2} G\rho \sum_{\mathcal{E}ij} \boldsymbol{r}_{\mathcal{E}ij} \cdot \boldsymbol{E}_{\mathcal{E}ij} \cdot \boldsymbol{r}_{\mathcal{E}ij} \cdot L_{\mathcal{E}ij} - \frac{1}{2} G\rho \sum_{\mathcal{F}ijk} \boldsymbol{r}_{\mathcal{F}ijk} \cdot \boldsymbol{F}_{\mathcal{F}ijk} \cdot \boldsymbol{r}_{\mathcal{F}ijk} \cdot \omega_{\mathcal{F}ijk} \quad (3.1)$$

Here, G is the gravitational constant, ρ is the bulk density of the small body (taken to be constant), $\boldsymbol{r}_{\mathcal{E}ij}$ and $\boldsymbol{r}_{\mathcal{F}ijk}$ are the vectors from the dust particle to any vertex of edge $\mathcal{E}_{ij}$ and face $\mathcal{F}_{ijk}$ respectively, $\boldsymbol{E}_{\mathcal{E}ij}$ and $\boldsymbol{F}_{\mathcal{F}ijk}$ are the dyads of edge $\mathcal{E}_{ij}$ and face $\mathcal{F}_{ijk}$ respectively,

$$\boldsymbol{E}_{\mathcal{E}ij} = \widehat{\boldsymbol{N}}_{\mathcal{F}ijk} \widehat{\boldsymbol{N}}_{\mathcal{E}ij}^T + \widehat{\boldsymbol{N}}_{\mathcal{F}ijk} \widehat{\boldsymbol{N}}_{\mathcal{E}ij}^T \quad (3.2)$$

$$\boldsymbol{F}_{\mathcal{F}ijk} = \widehat{\boldsymbol{N}}_{\mathcal{F}ijk} \widehat{\boldsymbol{N}}_{\mathcal{E}ij}^T \quad (3.3)$$

and $\widehat{\boldsymbol{N}}_{\mathcal{F}ijk}$ and $\widehat{\boldsymbol{N}}_{\mathcal{E}ij}$are the outward-pointing normals of each edge and facet. The per edge and per facet factor are given by

$$L_{\mathcal{E}ij} = ln\left(\frac{r_i + r_j + e_{ij}}{r_i + r_j - e_{ij}}\right) \quad (3.4)$$

$$\omega_{\mathcal{F}ijk} = 2\, atan\left(\frac{\boldsymbol{r}_i \cdot (\boldsymbol{r}_j \times \boldsymbol{r}_k)}{r_i r_j r_k + r_i(\boldsymbol{r}_j \cdot \boldsymbol{r}_k) + r_j(\boldsymbol{r}_k \cdot \boldsymbol{r}_i) + r_k(\boldsymbol{r}_i \cdot \boldsymbol{r}_j)}\right) \quad (3.5)$$

where $\boldsymbol{r}_i$ is the vector from vertex $\boldsymbol{P}_i$ to $\boldsymbol{r}_{\boldsymbol{i}}$ and e_{ij} is the length of the edge connecting vertex $\boldsymbol{P}_i$ to $\boldsymbol{P}_j$. Figure 3.1 (top) shows the gravitational acceleration evaluated over the surface of asteroid 1992SK with a bulk density of 2.3 g/cm^3 [5]. The local surface gravity is approximately 3×10^{-4} m/s^2.

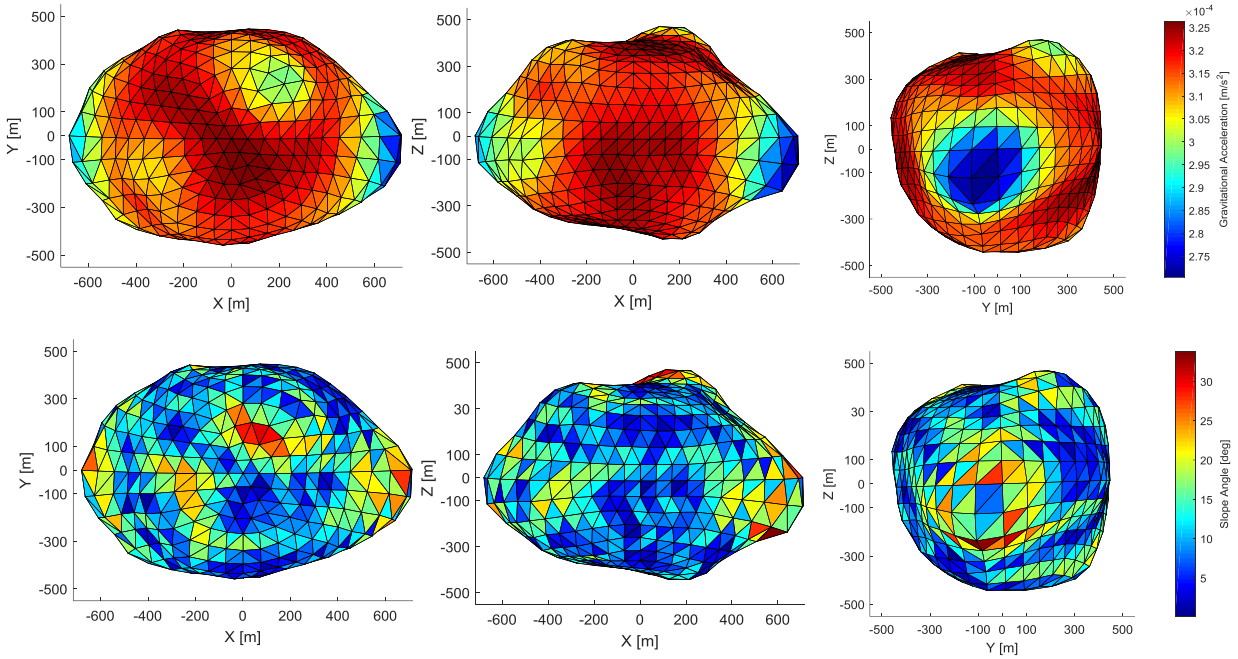

Figure 3.1: Gravitational acceleration (top) and slope angle (bottom) evaluated over the surface of 1992SK, shown in principal axis rotation.

In addition, the surface slope angle is defined as the angular offset between the face-normal vector and the local gravity unit vector. This angle can be used to evaluate the local topography of a body, particularly when investigating surface strength, gravitational potential lows, and regions of down sloping material.

$$\text{slope} = \text{acos}\left(-\widehat{\boldsymbol{N}}_{\mathcal{F}ijk} \cdot \hat{\boldsymbol{g}}\right) \qquad (3.6)$$

Evaluating the slope angle over the surface of asteroid 1992SK, Figure 3.1 (bottom) shows the local slope with a maximum of 31 degrees and a mean of 11 degrees. Both the surface gravity and slope surface plots match with the results found in Busch et al. [5].

Another convenience of the constant density polyhedron model is the ability to determine if a point is inside or outside the body. For a point inside the body, the sum of solid angles (defined as the Laplacian divided by $G\rho$) is -4π. For a point outside the body, it is zero. Using this fact, we can determine if a simulated dust grain has reimpacted the surface and stop the simulation if it has.

While the constant density polyhedron model and rotational terms (see equation 3.39) are used to simulate the gravity field throughout a dust grain's trajectory, an effective gravity is used when generating dust grain initial conditions. This effective gravity is calculated by dotting the gravity vector at the grain's initial location with the surface normal. Only surface normal forces are used in generating the initial upward velocity of a grain. Sections using an effective gravity will be denoted as such.

When examining different spin rates of small bodies in later sections, we only consider cases when the centripetal acceleration is smaller in magnitude than the surface gravity. Thus, the maximum spin rate ω_{max} of the primary body can be solved for using the equation below.

$$\omega_{max}^2 = \frac{4}{3}\pi G\rho \quad (3.7)$$

For a primary body density of 1.2 g/cm^3 [28, 52], the maximum spin rate gives a rotational period of approximately 3.01 hours. A conservative value of 3.1 hours will be used to simulate the fastest rotating bodies in this study.

3.2 Solar Radiation Pressure Model

Bodies in the vicinity of the Sun will experience a perturbation known as solar radiation pressure from the exchange of momentum between solar electromagnetic waves and the body. This perturbation is particularly significant for smaller objects, such as dust, for which the surface area to mass ratio is large. As will be discussed in Chapter 5, solar radiation pressure plays a major role in eliminating fine dust grains from the surface of small bodies over time. For the analysis presented here, a spherical dust shape is assumed, giving the following cannonball model [48].

$$\boldsymbol{a}_{SRP} = -p_{SRP} C_R \left(\frac{A_\odot}{m_d}\right) \frac{\boldsymbol{r}_{Sun/dust}}{|\boldsymbol{r}_{Sun/dust}|} \cdot \nu \quad (3.8)$$

Here, p_{SRP} is the solar radiation pressure (taken as 4.57×10^{-6} N/m^2 at 1 AU), C_R is the reflectivity (between 0 and 2), $A_\odot$ is the area exposed to the Sun, m_d is the mass of the dust particle, $\boldsymbol{r}_{Sun/dust}$ is the position of the Sun with respect to the dust particle, and ν is a coefficient used to switch the perturbation on and off. For the reflectivity, a value of 0 means that the object is fully translucent, and no momentum is imparted. A value of 1 means that the object fully absorbs the incoming radiation and all the momentum is transmitted. A value of 2 means the object reflects all the incoming radiation, resulting in twice the momentum transfer. For the study under consideration here, an intermediate value of 1 is chosen. Note that for micron-sized dust grains, the effective scattering cross section becomes significant and the radiation pressure should account for this dependence on grain size [4]. However, because we examine grain sizes 1 micron and above where this effect is negligible, we do not factor it into the current study.

There is an additional challenge of accounting for solar eclipsing when the dust particle passes behind the small body with respect to the Sun. To account for this eclipsing, and the resulting drop of the solar radiation pressure, an ellipsoid eclipsing model was implemented using the method in Xin and Scheeres [57]. In this model, the small body is represented as an ellipsoid

$$\frac{X'^2}{\alpha^2} + \frac{Y'^2}{\beta^2} + \frac{Z'^2}{\gamma^2} = 1 \qquad (3.9)$$

where each coordinate is given by

$$\begin{aligned} X' &= X + l_x \cdot s \\ Y' &= Y + l_y \cdot s \\ Z' &= Z + l_z \cdot s \end{aligned} \qquad (3.10)$$

Here $\{\alpha\ \beta\ \gamma\}$ are the ellipsoid radii normalized with respect to the longest axis of the ellipsoid, $\{X\ Y\ Z\}$ are the dust particle's positions with respect to the small body scaled by

the longest axis of the ellipsoid, and s is the half-line parameter. The normalized position vector of the Sun is given by

$$\frac{\boldsymbol{r}_{Sun/Ast}}{|\boldsymbol{r}_{Sun/Ast}|} = \begin{pmatrix} l_x \\ l_y \\ l_z \end{pmatrix} = \begin{pmatrix} \cos nt \\ \sin nt \\ 0 \end{pmatrix} \qquad (3.11)$$

where n is the mean motion of the small body around the Sun, assuming a circular orbit at 1 AU that is aligned with the ecliptic. Combining these equations gives the following quadratic equation of s for the intersection points of the half-line and the ellipsoid.

$$As^2 + 2Bs + C = 0 \qquad (3.12)$$

where

$$A = \frac{l_x^2}{\alpha^2} + \frac{l_y^2}{\beta^2} + \frac{l_z^2}{\gamma^2}$$

$$B = \frac{l_x X}{\alpha^2} + \frac{l_y Y}{\beta^2} + \frac{l_z Z}{\gamma^2} \qquad (3.13)$$

$$C = \frac{X^2}{\alpha^2} + \frac{Y^2}{\beta^2} + \frac{Z^2}{\gamma^2} - 1$$

This means that the dust particle will be in shadow, eclipsed by the small body, when there are two real positive roots for equation (3.12). Thus, the conditions for eclipsing are

$$\nu = \begin{cases} 0, & D > 0 \text{ and } B < 0 \\ 1, & \text{otherwise} \end{cases} \qquad (3.14)$$

where

$$D = B^2 - AC \qquad (3.15)$$

When $D > 0$ and $B < 0$, the ν coefficient is zero and the solar radiation pressure is turned off. Otherwise, the solar radiation pressure remains turned on with a ν coefficient of 1. In this way, the perturbation experienced by the dust particle from solar radiation pressure

can be switched on and off, depending on whether the dust particle is in light or shadow. Figure 3.2 shows a time history of a particle's trajectory (in pink) with the vector pointing from the dust grain to the Sun shown at each step in time. This dust particle-Sun vector is colored orange when solar radiation pressure is on and teal when solar radiation pressure is off.

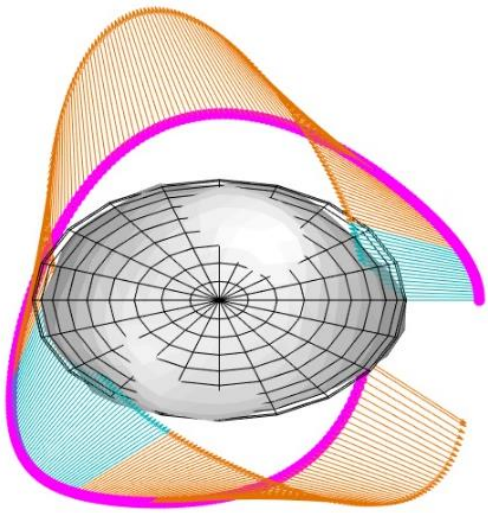

Figure 3.2: Dust particle trajectory (pink) shown in the XY-plane over time with the dust particle-Sun vector. Perturbation from solar radiation pressure is ON when this vector is orange and OFF when teal. The ellipsoid used to model the asteroid is gridded over asteroid 1992SK.

As illustrated, the ellipsoid eclipsing model can accurately determine whether the dust particle is in shadow or sunlight at any given point in its trajectory.

3.3 Electrostatics Model

The electrostatic force is the product of the dust particle charge and the local electric field strength, $F = Q_d E$. Assuming an electric field pointing outward normal to the surface of the small body, the acceleration of a charged dust grain in the presence of the electric field is

$$\boldsymbol{a}_{elect} = \frac{Q_d E}{m_d} \hat{\boldsymbol{r}}_{dust/Ast} \qquad (3.16)$$

Both the electric field model and the grain-charging model are discussed in this section. Note that the electrostatics model detailed in this chapter is used throughout the entirety of a dust grain's simulated trajectory in the SBEM. In contrast, the grain-scale supercharging model is only used to calculate dust grain initial conditions and is discussed in Chapter 4.

3.3.1 Electric Field Model

Small bodies and moons within the Solar System exist within the solar wind, a neutral plasma made up of roughly equal parts of electrons and ions that flow outward from the Sun. Because the lighter plasma electrons move much faster than the heavier plasma ions, the flux of electrons moving toward the surface is greater than the flux of ions, and the body's surface tends to charge negatively. However, an airless body's surface is also charged from incident rays of solar ultraviolet radiation hitting the surface. These ultraviolet rays cause electrons to be emitted from the surface in a process known as photoelectron emission, which tends to charge the surface positively. The charge of the surface will thus be a delicate balance of currents to and from the surface due to solar wind electrons, solar wind ions, and photoelectrons.

On the dayside of a small body, the surface tends to charge positively due to the dominance of photoemission. A layer of inbound and outbound electrons is formed above the surface, known as the photoelectron sheath. This sheath generates an electric field normal to the surface which acts to return negatively charged particles back to the surface and to accelerate positively charged particles away from the surface. On the nightside of a small body, the surface tends to charge negatively due to the absence of photoemission there. The charging of the terminator region—the region that divides day from night—remains a complex region of charging at low photoemissive angles.

In general, because the surface of a small body is charged, an electric field is generated and charged particles moving near the surface will experience a force

proportional to their charge and the strength of the electric field. The electric field strength is determined by assuming an electric potential profile shape (i.e. monotonic, non-monotonic, increasing, decreasing) and using the boundary conditions in the solar wind at infinity and on the surface of the small body to solve for the electric potential (and electric field) at every point in space between. The distribution of electrons discussed in this paper are considered to be Maxwellian. The distribution function is integrated over the three components of velocity to find the expected velocity value, which is then used to compute the plasma particle densities at all locations in space. This particle density distribution over space gives electric potential gradients, which are used to compute the electric field. Poisson's equation relates the electric potential to the charge density, and thus the electric field is simply the negative gradient of the electric potential.

$$\nabla^2\phi = -\frac{\rho}{\varepsilon} \qquad (3.17)$$

$$\text{where } \boldsymbol{E} = -\nabla\phi \qquad (3.18)$$

The work presented in this thesis uses an analytical monotonically-decreasing dayside sheath with an electric field directed away from the surface and field strength given as a function of altitude. This model was simpler to implement and quicker to run when compared to more complicated numerical models such as that presented in Nitter et al. [31].

Note that for all the simulations run in this thesis, we only model the plasma sheath on the dayside of the small body. While it has been shown that the nightside tends to charge negatively and develops a plasma sheath [17, 18, 61], it is standard practice to set the electrostatic force to zero once a grain passes into shadow for simplification [7, 27], as is done here. While setting the electrostatic force to zero in shadow does affect the ends of trajectories of a few particles lofted close to the terminator region (going into the nightside),

the overwhelming majority of particles are not affected and are sunlit throughout the entirety of their trajectories.

3.3.1.1 Analytical Dayside Sheath

The electric field model under consideration was developed by Grard and Tunaley [16] and has a monotonically-decreasing potential profile. This model was used by Colwell et al. [7] and Hughes et al. [27] to examine dust motion near craters on the asteroid Eros. In this model, the solar wind density is assumed to be constant and is not modified by interaction with the small body surface. This means that the photoelectron density, the only plasma species varying with altitude, creates the potential variation. This analytical sheath model, so called because of its analytical description of the electric field, provides a quick method of generating electric field data at each step in time within our SBEM. Note that this model only gives the electric field variation in the surface normal direction. No tangential electric field is given. The electric field strength E as a function of height h from the surface is given by

$$E(h) = E_0 \left(1 + \frac{h}{\sqrt{2}\lambda_{D0}}\right)^{-1} \qquad (3.19)$$

Here the electric field strength at the surface E_0 requires solution of the floating potential of the surface ϕ_s and the Debye length at the surface λ_{D0}. Both are dependent on the local solar elevation angle i_s measured from the horizon at the point of interest on the surface.

$$E_0 = \frac{2\sqrt{2}\phi_s}{\lambda_{D0}} \qquad (3.20)$$

The surface floating potential is solved for using a current balance between the photoemission particles and the solar wind electrons at the small body surface. This is shown in the relation below, which equates surface electron fluxes from photoemission and the solar wind.

$$J_{ph0}\, exp\left(\frac{-e\phi_s}{k_B T_{pe}}\right) \sin i_s = n_{sw}\sqrt{\frac{k_B T_{sw}}{2\pi m_e}}\left(1 + \frac{e\phi_s}{k_B T_{sw}}\right) \qquad (3.21)$$

Here J_{ph0} is the photoelectron emission flux of the surface material due to the Sun, taken to be $J_{ph0} = 2.8 \times 10^9/d^2$ electrons/(cm^{2}s) where d is the distance in AU's from the Sun. Also e is the charge of an electron, k_B is Boltzmann's constant, T_{pe} is the photoelectron temperature, n_{sw} is the solar wind electron density, T_{sw} is the solar wind electron temperature, and m_e is the mass of an electron. The Debye length at the surface is given by

$$\lambda_{D0} = \sqrt{\frac{\varepsilon_0 k_B T_{pe}}{n_{pe0} e^2}} \qquad (3.22)$$

Here ε_0 is the permittivity of free space and n_{pe0} is the photoelectron density at the surface, given as a function of the solar elevation angle below.

$$n_{pe0} = 2J_{ph0} \sin(i_s) / v_{pe} \qquad (3.23)$$

The average photoelectron emission velocity v_{pe} is given by

$$v_{pe} = \sqrt{\frac{2k_B T_{pe}}{m_e}} \qquad (3.24)$$

and the solar elevation angle i_s is measured from the local horizon.

$$\sin i_s = \hat{\boldsymbol{r}}_{Sun/Ast} \cdot \hat{\boldsymbol{n}} \qquad (3.25)$$

Note that the electric field is dependent on both the height from the surface and the solar elevation angle, which varies throughout the day. We only consider solar elevation angles above 10 degrees due to the limitations of this model [7]. As a result, the terminator regions are not well modeled electrostatically. The electrostatic force is computed and implemented at every point along a particle's trajectory, even when the particle is very far from the surface and the force is negligible. The only time the electrostatic force is expressly set to zero is when the particle travels into shadow on the nightside of the body.

The values stated in Colwell et al. [7] at a distance of 1 AU from the Sun were used in this work. We use an average photoelectron temperature of $k_B T_{pe}$= 2.2 eV as measured by Willis et al. [55] for lunar regolith, a solar wind electron density of n_{sw}= 5 electrons/cm^2, and an average solar wind electron temperature of $k_B T_{sw}$= 10 eV. The electric field strength in the near-surface region of a small body at 1 AU is shown in Figure 3.3. as a function of height and solar elevation angle.

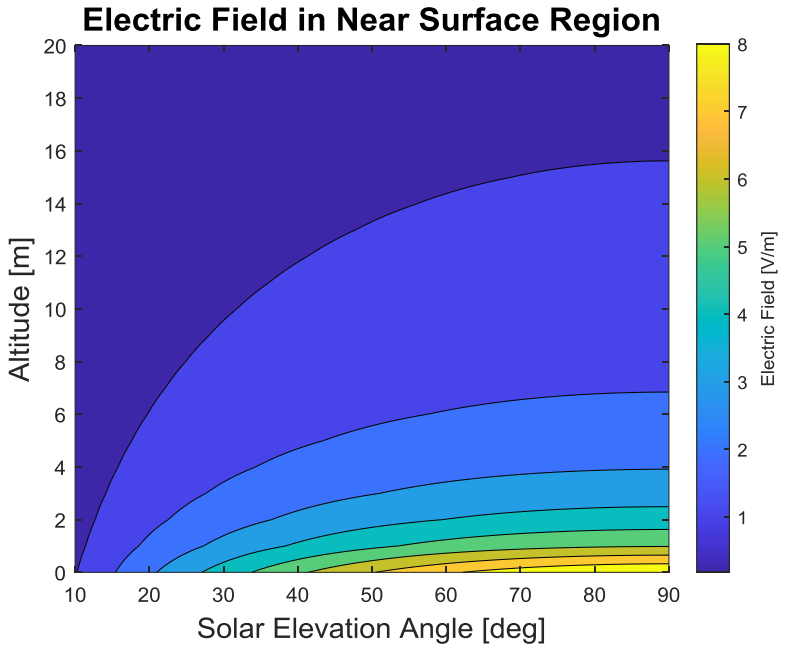

Figure 3.3: Electric field strength as a function of height and solar elevation angle for a small body surface at 1 AU.

As expected, the electric field strength falls off quickly as a function of height (goes as 1/h). A maximum electric field strength of 9 V/m at the surface is seen at local noon, while lower solar elevation angles will experience lower electric field strengths at the surface. Note that this model will tend to overestimate the effect of electrostatic forces. Future work should include incorporation of a more accurate non-monotonic plasma sheath profile such as that given in Nitter et al. [31], which predicts a maximum electric field strength near 3 V/m.

If we perform a series expansion of the electric field about a given solar elevation angle (θ below), we can approximate the tangential electric field at the surface as a function of the solar elevation angle. I've reproduced the calculations below and included a plot of the tangential electric field as a function of the solar elevation angle in Figure 3.4.

Defining our electric field function as the electric field in the surface normal direction,

$$F(\theta) = E(\theta)\,\hat{n}(\theta) \quad (3.26)$$

we then take the first and second derivatives with respect to the solar elevation angle.

$$\frac{\partial F}{\partial \theta} = \frac{\partial E}{\partial \theta}\,\hat{n} + E(\theta)\frac{\partial \hat{n}}{\partial \theta} = \frac{\partial E}{\partial \theta}\,\hat{n} + E(\theta)\,\hat{n}_{\perp} \quad (3.27)$$

$$\frac{\partial^2 F}{\partial \theta^2} = \frac{\partial^2 E}{\partial \theta^2}\,\hat{n} + 2\frac{\partial E}{\partial \theta}\frac{\partial \hat{n}}{\partial \theta} + E(\theta)\frac{\partial^2 \hat{n}}{\partial \theta^2} = \frac{\partial^2 \hat{n}}{\partial \theta^2}\,\hat{n} + 2\frac{\partial E}{\partial \theta}\,\hat{n}_{\perp} - E(\theta)\,\hat{n} \quad (3.28)$$

$$\frac{\partial \hat{n}}{\partial \theta} = \hat{n}_{\perp} \quad (3.29)$$

$$\frac{\partial^2 \hat{n}}{\partial \theta^2} = -\hat{n} \quad (3.30)$$

Expanding about the solar elevation angle by an infinitesimal amount $\Delta\theta$, we find the following.

$$F(\theta + \Delta\theta) = E(\theta + \Delta\theta)\,\hat{n}(\theta + \Delta\theta)$$

$$= F(\theta) + \frac{\partial F}{\partial \theta}\Delta\theta + \frac{1}{2}\frac{\partial^2 F}{\partial \theta^2}\Delta\theta^2 + \cdots$$

$$= E(\theta)\,\hat{n}(\theta) + \left(\frac{\partial E}{\partial \theta}\,\hat{n} + E(\theta)\,\hat{n}_{\perp}\right)\Delta\theta + \frac{1}{2}\left[\frac{\partial^2 E}{\partial \theta^2}\,\hat{n} + 2\frac{\partial E}{\partial \theta}\hat{n}_{\perp} - E(\theta)\,\hat{n}\right]\Delta\theta^2 + \cdots \quad (3.31)$$

Dotting this function with either the normal $\hat{n}$ or tangential $\hat{n}_{\perp}$ direction, we find the associated components of the electric field as a function of solar elevation angle.

$$F(\theta + \Delta\theta)\cdot\hat{n} = E(\theta) + \frac{\partial E}{\partial \theta}\Delta\theta + \frac{1}{2}\frac{\partial^2 E}{\partial \theta^2}\Delta\theta^2 - \frac{1}{2}E(\theta)\Delta\theta^2 + \cdots \quad (3.32)$$

$$F(\theta + \Delta\theta)\cdot\hat{n}_{\perp} = E(\theta)\Delta\theta + \frac{\partial E}{\partial \theta}\Delta\theta^2 + \cdots \quad (3.33)$$

In Figure 3.4 below, the electric field at the surface is plotted, along with the approximated lateral electric field and the slope of the electric field.

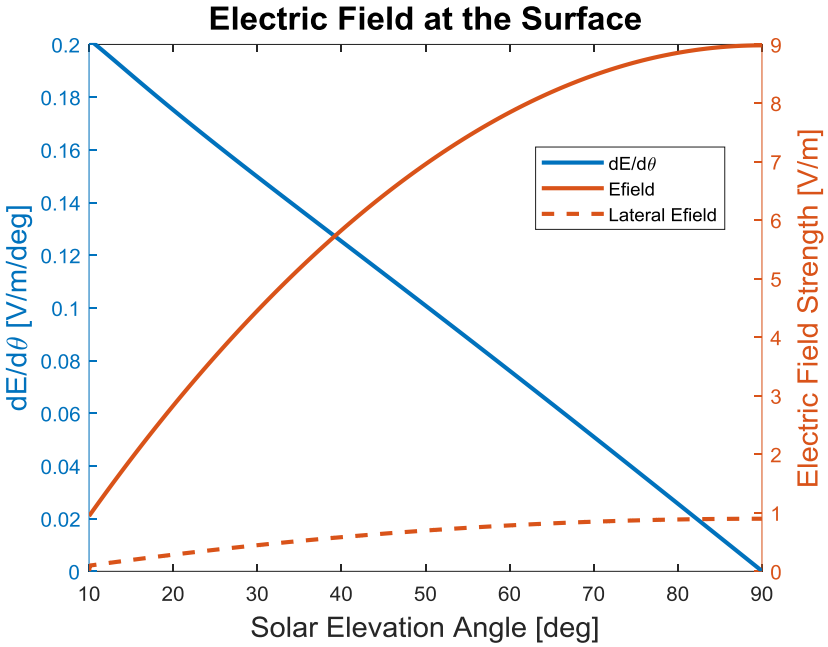

Figure 3.4:.Electric field at the surface and the lateral electric field as a function of solar elevation angle.

From this, we see that the lateral field at the surface is greatest at the subsolar point where it reaches a strength of 1 V/m. This strength decreases as you move closer to the terminator regions (to lower solar elevation angles). Thus, the lateral electric field will affect dust grain motion the most near local noon. Hartzell [22] showed that the tangential electric field accelerates grains towards the terminator, but does not significantly alter the trajectories of grains in their two-dimensional asteroid simulation. We do not model the tangential electric field in our study; however, it should be included in future studies.

The equilibrium dust potential ϕ_d can help to explain general dust behavior in the plasma sheath. It is calculated by setting the current to the grain (equation 3.37) equal to zero and solving for the dust potential. Figure 3.5 gives the equilibrium dust potential at local noon at a distance of 1 AU as a function of altitude.

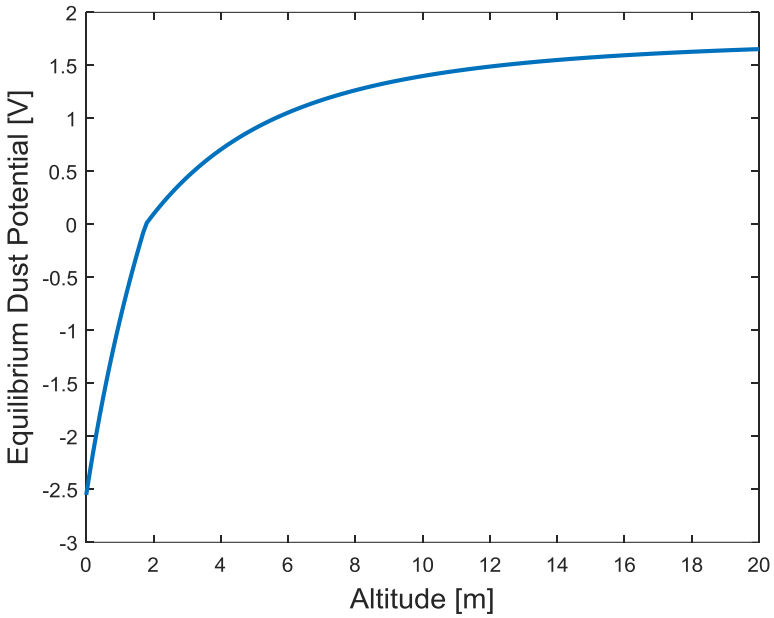

Figure 3.5: Equilibrium dust potential at local noon at a distance of 1 AU as a function of height.

Looking at the equilibrium dust potential, we see that within about a Debye length (1.38 meters) of the surface, the particle is negatively charged from the collection of photoelectrons in the sheath. At larger distances from the surface, the particle charges positively due to photoemission of the particle itself from solar wind electrons. We will continue to explore how the plasma sheath affects grain charging in later sections.

3.3.1.2 Facet Tracking Method and Altitude Calculation

The electric field model discussed above requires accurate calculation of the grain's altitude above the surface at all points throughout its trajectory. We developed a method which tracks the specific facet directly beneath the dust particle at any time and uses that facet's electric field to calculate the electric field strength at the particle's height. The specific implementation is described in detail below.

First, the distances between the particle's current location and all the facet centers are calculated. These values are then sorted from minimum to maximum distance. The facet corresponding to the minimum distance is selected for a series of checks which ensure

that the particle is indeed within the triangular area of the selected facet. This check is necessary because minimum distances are calculated from the facet centers, which means that a particle could technically be located over one facet but slightly closer to another facet's center point. Using the vectors which define the selected facet's edges, a series of dot and cross products (equation 3.34) are used to determine if the particle is located within the facet's boundaries. Figure 3.6 gives a visual representation of the vector quantities under consideration for a given facet.

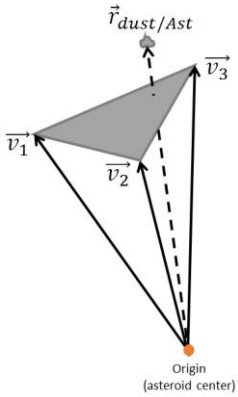

$$\boldsymbol{r}_{dust/Ast} \cdot (\boldsymbol{v}_1 \times \boldsymbol{v}_2) \geq 0$$
$$\boldsymbol{r}_{dust/Ast} \cdot (\boldsymbol{v}_2 \times \boldsymbol{v}_3) \geq 0 \qquad (3.34)$$
$$\boldsymbol{r}_{dust/Ast} \cdot (\boldsymbol{v}_3 \times \boldsymbol{v}_1) \geq 0$$

Figure 3.6: Vector quantities used to check if dust particle is within the area defined by the individual facet.

If the relations are all satisfied, then the particle lies within the area of the selected facet and the code moves on to determining the exact height above the surface. However, if one or more of the relations is not satisfied, then the particle does not lie within the facet's area. In this case, the facet with the next minimum distance is selected to be checked, and the process continues until the criteria is met.

As an illustration of why this change was needed, over the course of an example test trajectory, 130 points out of 374 points were found to be using an incorrect facet to compute the electric field strength. From the specific cases investigated, the previous algorithm did not switch over to a new facet early enough, which is logical since the distance to a new facet will decrease as it approaches the center point but may not be minimum compared to another facet center (depending on the specific topography of the surface). Note that while

the resulting change in electric field computed at each step may not change significantly because of this improved algorithm, it is a much more accurate computation of the surrounding plasma field. Future modifications to increase the fidelity of the electric field calculation may need this level of precision to be implemented.

Once the correct facet is found, the scalar height is calculated using the distance vector from the facet's center to the location of the dust particle and dotting it with the surface normal vector of the facet (equation 3.35). In this way, a scalar height normal to the surface is calculated. Figure 3.7 illustrates this height as the perpendicular distance from the facet's surface.

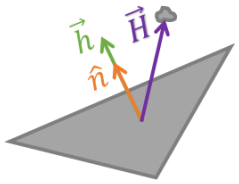

$$h = |\boldsymbol{h}| = |\boldsymbol{H} \cdot \hat{\boldsymbol{n}}| \quad (3.35)$$

Figure 3.7: The height at a given time is calculated as the perpendicular distance of the particle from the plane of the facet directly below it.

The facet location is used to determine the electric field strength at the surface (given the solar elevation angle at that location in time) and the height is then used to determine the electric field strength at a given distance from this surface value. In this way, the height and resulting electric field strength is calculated at each time step as the particle's position over the surface changes. By calculating the facet location and height this way, a more realistic value for the electric field strength is used in determination of the electrostatic force acting on the particle at each point in its trajectory.

For an example trajectory, Figure 3.8 below illustrates that despite how complicated the dust particle's trajectory gets, the surface facets directly below are always tracked. Note that the plasma sheath surrounding the small body rapidly decays with distance from the surface, and so the electric field will not affect particle motion significantly when it is tens

of meters off the surface. However, this figure nonetheless illustrates successful implementation of the algorithm.

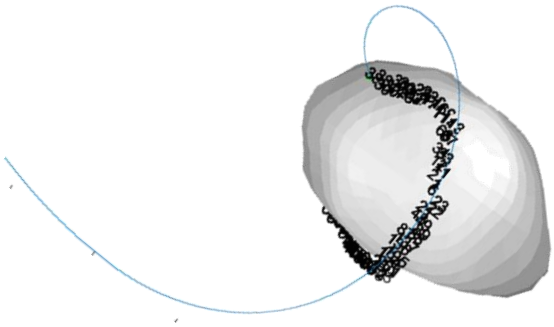

Figure 3.8: Example trajectory with the denoted surface facets used for computation of the electric field strength at each point in the particle's path about the small body.

Note that while the electric field is modeled in 1D vertically over a specific facet, as a grain travels across the surface of the small body, it will experience a variation in its electric field both vertically (as a function of height) and horizontally (as it encounters new facets pointing in different directions). Because the surface normal direction changes from one facet to another, the direction of the outward pointing electric field also changes depending on which facet a grain is over. In this way we are able to apply a 1D plasma sheath model in a 3D small body environment. Note that the changes in the electric field will be discontinuous at the edges of facets and there is no explicit tangential electric field implemented in this model. A tangential electric field should be implemented in future work. Next, we look at the grain charging models to complete determination of the electrostatic force.

3.3.2 Dust Grain Charging

Recall that the electrostatic force is the product of the dust particle charge and the surrounding electric field, $F = Q_d E$. The equations in the previous section provide the equations needed to compute the electric field, but the charge of the dust particle still needs to be considered. A dust particle near the surface of an asteroid or moon will experience

currents due to its interaction with the near-surface plasma sheath, the solar wind, and its own photoemission. Thus, the currents flowing to and from the particle are due to photoelectrons in the sheath, solar wind electrons, solar wind ions, and dust particle photoemission. The time rate of change of the charge of the particle depends on the different currents to and from the particle, the magnitudes of which are dependent on the time-varying charge of the particle and the altitude of the particle. Because the particle charge is dependent on altitude, the charging rate and the equations of motion will be coupled.

$$\dot{Q}_d = \sum_i I_i \quad (3.36)$$

Recall that the electric field of the small body also varies in both altitude and time (through the solar elevation angle). The specific equations for dust grain charging in the plasma sheath are developed next. Grain-scale supercharging is discussed in the following chapter with methods of generating initial conditions.

3.3.2.1 Thermalized Electron Currents

For use with the analytical dayside model discussed in section 3.3.1, a fully thermalized plasma is used to develop the charging equations of motion and follows the work of Havnes et al. [24]. There are three main currents flowing to the dust particle in the model that affect its charge over time— the current of photoelectrons I_{pe} emitted by the grain, the current of photoelectrons $I_e$to the grain, and the current due to the collection of solar wind electrons I_{sw}. Note that the current due to solar wind ions is neglected in this model. Because dust grains exposed to the solar wind attain a positive charge from photoemission, their grain charge is moderated by the collection of solar wind electrons, and thus the current due to solar wind ions can be neglected [7]. In this way, the solar wind

electron current prevents grain charge from growing without bound outside the photoelectron sheath. The dust particle's charge changes over time as

$$\frac{dQ_d}{dt} = I_{pe} - I_e - I_{sw} \quad (3.37)$$

where the photoelectron current is the only one that changes as a function of height and solar elevation angle. All the currents are dependent on the electric potential of the dust particle ϕ_d, related to the particle's charge via the capacitance.

$$Q_d = 4\pi\varepsilon_0 r_d \phi_d \quad (3.38)$$

Each current source is described briefly in the following paragraphs.

The current of photoelectrons emitted by the dust particle due to incoming ultraviolet solar radiation is given by

$$I_{pe} = \pi r_d^2 e J_{ph0} \quad \text{for } \phi_d \leq 0$$
$$I_{pe} = \pi r_d^2 e J_{ph0} \exp\left(\frac{-e\phi_d}{k_B T_{pe}}\right) \quad \text{for } \phi_d > 0 \quad (3.39)$$

Recall that J_{ph0} is the photoelectron emission flux of the surface, k_B is Boltzmann's constant, and T_{pe} is the photoelectron temperature.

The current of photoelectrons to the particle (from the surface or other dust grains) is given by

$$I_e = \pi r_d^2 e n_{pe} \sqrt{\frac{8k_B T_{pe}}{\pi m_e}} \exp\left(\frac{e\phi_d}{k_B T_{pe}}\right) \quad \text{for } \phi_d \leq 0$$
$$I_e = \pi r_d^2 e n_{pe} \sqrt{\frac{8k_B T_{pe}}{\pi m_e}} \left(1 + \frac{e\phi_d}{k_B T_{pe}}\right) \quad \text{for } \phi_d > 0 \quad (3.40)$$

Here the photoelectron density at the surface n_{pe0} is used to determine the photoelectron density at any height h above the surface using the following relation.

$$n_{pe}(h) = n_{pe0}\left(1 + \frac{h}{\sqrt{2}\lambda_{D0}}\right)^{-2} \quad (3.41)$$

Recall that λ_{D0} is the Debye length at the surface, given by equation 3.20.

And finally, the current due to the collection of solar wind electrons is given by

$$I_{sw} = \pi r_d^2 e n_{sw}\sqrt{\frac{8k_B T_{sw}}{\pi m_e}}\exp\left(\frac{e\phi_d}{k_B T_{sw}}\right) \quad \text{for } \phi_d \leq 0$$

$$I_{sw} = \pi r_d^2 e n_{sw}\sqrt{\frac{8k_B T_{sw}}{\pi m_e}}\left(1 + \frac{e\phi_d}{k_B T_{sw}}\right) \quad \text{for } \phi_d > 0 \quad (3.42)$$

Here n_{sw} is the solar wind electron density and T_{sw} is the solar wind electron temperature. Note, as mentioned above, the electron density on the surface is not constant with time, but instead varies as the small body rotates with respect to the Sun (n_{pe0} varies with i_s). Thus, the solar elevation angle must be computed at each step in time as well. Once the solar elevation angle is known, the photoelectron density at the surface and at the given height can be found, which enables calculation of the currents to/from the dust grain. This then provides us with a means to fully calculate a particle's charge Q_d by integrating the current equations over time. These current equations are computed at each step in time, and the resulting dust particle charge (equation 3.37) integrated simultaneously with the dynamic equations of motion (equation 3.46).

It should be noted that this grain charging model uses the traditional assumption that dust grains in sunlight should be positively charged from photoemission. In making this assumption, the model is able to neglect the current due to solar wind ions, and instead uses photoelectrons to limit charge growth outside the plasma sheath. However, because our dust grain initial conditions account for the buildup of charge in the microcavities between grains (i.e. from secondary electrons), we are finding that lofted grains have a negative charge (see Chapter 4 for details). Thus, we would expect plasma ions to affect charging of our lofted grain. Without ion current, the grain likely remains negative for a

longer period of time in our simulations than would be the case if it were included. Future work should implement a more complete plasma sheath and grain charging model such as that in Nitter et al. [31] which models all plasma species. However, the current model serves as a less computationally expensive (analytical) starting point in building the comprehensive model and simulation.

3.5 Single Particle Dynamics (Mass Orbiter Problem with Perturbations from SBEM)

Next, we develop the dynamical equations describing dust grain motion in the vicinity of a small body. Consider a dust particle orbiting an irregularly shaped body as illustrated in Figure 3.9. Note that the asteroid is assumed to have is spin axis about the z-direction. Thus, the inertial frame and body-fixed rotating frame are separated by a simple three rotation along the asteroid's z-axis.

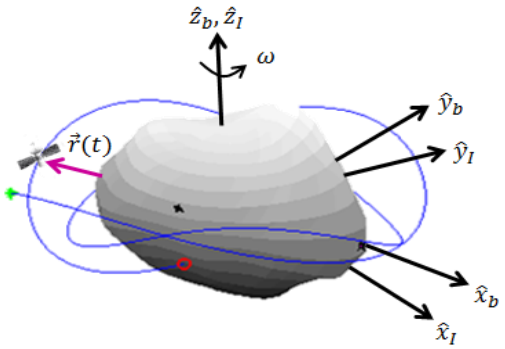

Spacecraft Position: $\boldsymbol{r} = \begin{bmatrix} x \\ y \\ z \end{bmatrix}$

Spacecraft Velocity: $\dot{\boldsymbol{r}} = \begin{bmatrix} \dot{x} \\ \dot{y} \\ \dot{z} \end{bmatrix}$

Spin-rate of Asteroid: $\boldsymbol{\omega} = \begin{bmatrix} 0 \\ 0 \\ \omega \end{bmatrix}$

Figure 3.9: Body-fixed rotating frame in the mass distribution orbiter problem.

Here, we parameterize the dust particle's position using coordinates in a body-fixed frame that rotates with the asteroid $\{\hat{\boldsymbol{x}}_B \ \hat{\boldsymbol{y}}_B \ \hat{\boldsymbol{z}}_B\}$. To develop the equations of motion, we use a Lagrangian formulation as follows.

Step 1: Form the Kinetic Energy (in body-fixed frame).

$$T(\boldsymbol{r},\dot{\boldsymbol{r}}) = \frac{1}{2}(\dot{\boldsymbol{r}} + \boldsymbol{\omega}\times\boldsymbol{r})\cdot(\dot{\boldsymbol{r}} + \boldsymbol{\omega}\times\boldsymbol{r})$$

$$= \tfrac{1}{2}\left[\dot{\boldsymbol{r}}\cdot\dot{\boldsymbol{r}} + 2\dot{\boldsymbol{r}}\cdot(\boldsymbol{\omega}\times\boldsymbol{r}) - (\boldsymbol{r}\cdot\boldsymbol{\omega})^{\mathbf{2}} + r^2\omega^2\right] \quad (3.43)$$

Step 2: Assume a form of the potential function (described by equation 3.1).

$$U(\boldsymbol{r}) = \frac{1}{2}G\rho\sum_{\varepsilon ij}\boldsymbol{r_{\varepsilon ij}}\cdot\boldsymbol{E_{\varepsilon ij}}\cdot\boldsymbol{r_{\varepsilon ij}}\cdot L_{\varepsilon ij} - \frac{1}{2}G\rho\sum_{Fijk}\boldsymbol{r_{\varepsilon ij}}\cdot\boldsymbol{F_{Fijk}}\cdot\boldsymbol{r_{Fijk}}\cdot\omega_{Fijk}$$

Step 3: Form the Lagrangian, defined as the sum of the kinetic energy and the potential function.

$$L(\boldsymbol{r},\dot{\boldsymbol{r}}) = T(\boldsymbol{r},\dot{\boldsymbol{r}}) + U(\boldsymbol{r})$$

$$= \frac{1}{2}\left[\dot{\boldsymbol{r}}\cdot\dot{\boldsymbol{r}} + 2\dot{\boldsymbol{r}}\cdot(\boldsymbol{\omega}\times\boldsymbol{r}) - (\boldsymbol{r}\cdot\boldsymbol{\omega})^{\mathbf{2}} + r^2\omega^2\right] + U(\boldsymbol{r})$$

$$L = \tfrac{1}{2}(x^2+y^2+z^2) + \omega^2\left(x\dot{y} - y\dot{x} + \tfrac{1}{2}x^2 + \tfrac{1}{2}y^2\right) + U(\boldsymbol{r}) \quad (3.44)$$

Step 4: Finally, perform $\frac{d}{dt}\left(\frac{\partial L}{\partial \dot{\boldsymbol{q}}}\right) = \frac{\partial L}{\partial \boldsymbol{q}}$ to form the equations of motion.

For $q_1 = x$: $\frac{d}{dt}\left(\frac{\partial L}{\partial \dot{x}}\right) = \frac{d}{dt}(\dot{x} - \omega^2 y) = \ddot{x} - \omega^2\dot{y}$ and $\frac{\partial L}{\partial x} = \omega^2\dot{y} + \omega^2 x + U_x$

$$\ddot{x} = 2\omega\dot{y} + \omega^2 x + U_x \quad (3.45a)$$

For $q_2 = y$: $\frac{d}{dt}\left(\frac{\partial L}{\partial \dot{y}}\right) = \frac{d}{dt}(\dot{y} + \omega^2 x) = \ddot{y} + \omega^2\dot{x}$ and $\frac{\partial L}{\partial y} = -\omega^2\dot{x} + \omega^2 y + U_y$

$$\ddot{y} = -2\omega\dot{\boldsymbol{x}} + \omega^2 y + U_y \quad (3.45b)$$

For $q_3 = z$: $\frac{d}{dt}\left(\frac{\partial L}{\partial \dot{z}}\right) = \frac{d}{dt}(\dot{z}) = \ddot{z}$ and $\frac{\partial L}{\partial z} = U_z$

$$\ddot{z} = U_z \quad (3.45c)$$

These equations of motion can then be integrated over time in the body-fixed frame to give a trajectory. Adding to these equations the perturbations due to the solar radiation pressure and electrostatic force, we get the full dynamical equations describing single particle motion in the small body environment model.

$$\begin{bmatrix}\ddot{x}\\ \ddot{y}\\ \ddot{z}\end{bmatrix} = \frac{\partial U_{poly}}{\partial \boldsymbol{r}} - \nu\, p_{SRP} C_R \frac{A_\odot}{m_d}\hat{\boldsymbol{r}}_{dust/Sun} + \frac{Q_d E}{m_d}\hat{\boldsymbol{r}}_{dust/Ast} + 2\omega_z \begin{bmatrix} v_y \\ -v_x \\ 0 \end{bmatrix} + \omega_z^2 \begin{bmatrix} x \\ y \\ 0 \end{bmatrix} \quad (3.46)$$

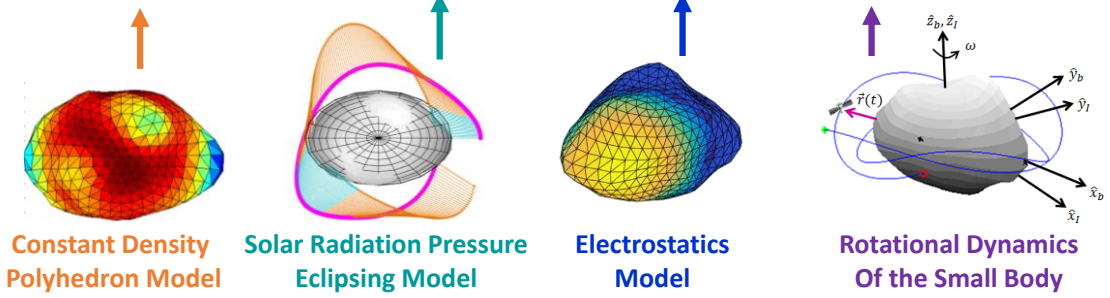

Figure 3.10: Equations of motion for a single dust grain moving in the small model environment model.

Here, ω_z is the spin rate of the small body, assumed to be about the z-axis, and $U_i = \partial U/\partial \boldsymbol{r}$ gives the gravitational acceleration of the dust particle. The perturbation due to solar radiation pressure $\boldsymbol{a}_{SRP}$ is given by the second term, and the electrostatic acceleration $\boldsymbol{a}_{Elect}$ is given by the third. The final two terms give the Coriolis and centripetal accelerations, which are present because we integrate in the body-fixed reference frame. These equations of motion are integrated simultaneously with the dust particle charging rate (equation 3.36). Doing so provides a particle charge over time that is used in computing the electrostatic perturbation. Recall that the electric field (Section 3.3.1) also varies in time (via solar elevation angle) and altitude.

3.6 Summary

Overall, we have described in detail the individual modes which comprise the small body environment model used to simulate electrostatically-lofted dust grains. The SBEM incorporates a constant density polyhedron model for gravity (and reimpact conditions), a solar radiation pressure model with consideration to eclipsing scenarios, a near-surface electric field model, and a model for grain charging. Developing the dynamical equations describing single particle motion in the vicinity of a body and adding the relevant

perturbations from the SBEM, gives us the full dynamical equations of motion shown in equation 3.46. These equations are integrated simultaneously over time with the grain charging equations to propagate electrostatically-driven dust motion in the near-surface region of small bodies. The next chapter details the models used to describe grain-scale supercharging, as well as the methods developed to bound lofting requirements and generate initial conditions.

Chapter 4

Lofting Requirements & Initial Conditions

Electrostatic lofting of dust grains and their subsequent behavior is highly sensitive to initial conditions. In this chapter, we define electrostatic lofting dynamically with force balance and use this definition to solve for the lofting requirements grains must meet to separate from the surface. Additionally, we discuss the specific equations used to model regolith cohesive forces and grain-scale supercharging forces. In particular, advancements made in modeling grain-scale charging (discussed in section 2.4) are used to solve for maximum grain gap electric field conditions (at steady state), which can further be used to find maximum electrostatic forces, ejection speeds, and the associated maximum cohesive strengths that grains can overcome. In this way, lofting requirements are used in conjunction with new grain-scale supercharging models to bound grain initial conditions and surface conditions which lead to electrostatically-driven dust motion on small bodies. Note that in this section, the electric field refers to the grain-scale field in the microcavities between dust grains, as opposed to the global electric field acting outward normal to the surface (discussed in Section 3.3). The global electric field generated from the plasma sheath is implemented immediately after grain separation when the grain-scale forces no longer dominate.

4.1 Electrostatic Lofting Requirements

Electrostatic lofting occurs when the upward electrostatic force is able to overcome the downward forces of gravity and cohesion holding a dust grain to the surface. A free-body

diagram is given in Figure 4.1, showing all the general forces acting on a dust grain before lofting. A few simplifications are made for the lofting analysis. First, because the grain-scale electrostatic force is much larger than that due to the near-surface plasma sheath, we take the electrostatic force to be roughly equivalent to the grain-scale electrostatic force. Second, we have neglected the downward force from solar radiation pressure F_{SRP} when generating initial conditions. This decision was made in an effort to keep the initial conditions consistent across the body since solar radiation pressure will act in different directions depending on the grain's location and time of day (which affects the magnitude of the surface normal component). However, perturbations from solar radiation pressure are accounted for immediately after separation from the surface.

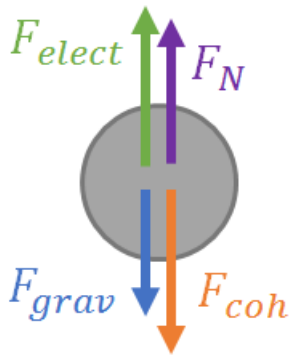

Figure 4.1: General free body diagram of a dust grain resting on the surface of a small body with the gravitational force F_{grav}, cohesive force F_{coh}, electrostatic force F_{elect}, and normal (restoring) force F_N shown.

Summing the forces acting on a dust grain resting on the surface of a body in the normal direction provides a general force balance when the dust grain is stationary.

$$ma = \sum F = F_{elect} + F_N - F_{grav} - F_{coh} = 0 \quad (4.1)$$

Here F_{elect} is the electrostatic force, F_N is the normal (restoring) force, F_{grav} is the gravitational force, and F_{coh} is the cohesive force. The normal force can only be non-

negative. Thus, solving for the normal force, we find the following inequality for the dust grain to be static.

$$F_N = F_{grav} + F_{coh} - F_{elect} \geq 0 \quad (4.2)$$

This means that while the normal force is greater than zero, the electrostatic force is less than the combined gravity and cohesion. As the electrostatic force grows, and just prior to separation, the normal force goes to zero and the force balance is

$$F_{elect} = F_{coh} + F_{grav} \quad (4.3)$$

At this point, the combined electrostatic and gravitational forces are equal to the cohesive strength. If the electrostatic force continues to increase, the strength of the cohesive force is then exceeded and, in this model, the contact between the grain and the surface (or a neighboring grain) is broken. As the cohesive force is only active over very small distances, this corresponds to the cohesive force disappearing, leading to the net acceleration being equal to the cohesive force divided by the particle mass.

While the model of the electrostatic force may change (grain charge, electric field, or both) as new experimental results emerge, the requirements for dust to become electrostatically lofted remain the same—the electrostatic force must overcome both gravity and cohesion to separate from the surface. After separation from the surface, the electric field from the global plasma sheath is applied to the charged dust grain in place of the larger grain-scale electric field, which only acts within a few grain radii. Note also that grains returning to the surface after lofting are not able to buildup sufficient grain-to-grain charge instantaneously to have an effect on their reimpact.

As derived above, the particle feels a net acceleration due to the loss of the cohesive force at separation from the surface. Thus, particles associated with larger cohesions will experience greater upward accelerations. See the following figure and equations for illustration.

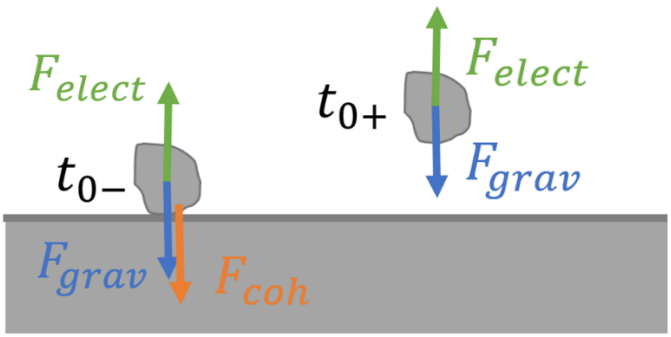

Figure 4.2: Free body diagram of the dust particle just before (t_{0-}) and just after (t_{0+}) separation from the small body surface.

At time t_{0-} just before separation from the surface, the particle feels a net acceleration of zero. The upward electrostatic force exactly cancels out the downward cohesive and gravitational forces.

$$\text{Particle resting on surface at } t_{0-}\text{: } \sum F(t_{0-}) = F_{elect} - F_{grav} - F_{coh} = 0 \qquad (4.4)$$

At time t_{0+} just after separation from the surface, the particle feels a net upward acceleration. Because the electrostatic and gravitational forces remain unchanged and only the cohesive force disappears with separation, the net upward force is equal to the cohesive force that had been binding the particle to the surface.

$$\text{Particle just after separation at } t_{0+}\text{: } \sum F(t_{0+}) = F_{elect} - F_{grav} = ma \qquad (4.5)$$

Solving for the extra acceleration felt by the particle at the instant of separation from the surface, we find the following relation. See equation 4 for the definition of the cohesive force used here.

$$a = \frac{F_{coh}}{m_d} = \frac{3}{2}\frac{\sigma_y}{\rho_d} r_d^{-1} = \frac{F_{elect} - F_{grav}}{m_d} = \frac{F_{elect}}{m_d} - g \qquad (4.6)$$

From this relation we see that for the same level of gravity, a larger, more massive particle will have a lower acceleration and a smaller, less massive particle will have a higher acceleration. Additionally, we see that for a given grain size, increasing the cohesive

strength of the material (σ_y) can lead to a higher acceleration, provided that sufficient electrical charge can be accumulated. These relationships and others will be further examined in Chapter 5 with discussion of lofted grain simulation results.

We move forward using the lofting requirements developed here to bound grain initial conditions using various models for the electrostatic and cohesive forces in the following sections.

4.2 Regolith Cohesion

Cohesion plays a major role in charged dust dynamics, as was shown computationally in [19] and experimentally in [21]. Even when accounting for grain-scale supercharging, cohesion appears to be a limiting factor in determining lofting requirements [62]. If a dust particle is unable to overcome the cohesive forces holding it to the surface, then electrostatic lofting cannot occur. Here we assume spherical grain particles, such that the cohesive force a particle feels on the surface can be modeled as

$$F_{coh} = \sigma_y A = \sigma_y\left(2\pi r_d^2\right) \qquad (4.7)$$

where σ_y is the cohesive strength of regolith given in Pascals and A represents the surface area of the grain resting in regolith [41]. For a spherical grain, we take the contact area to be half the surface area of a sphere. However, for non-spherical grains, this contact area will change depending on the shape of the grain and the contact points of the regolith it is resting in. For smaller contact areas, the cohesive force will decrease; while for larger contact areas, the cohesive force will increase. While we assume spherical grains in this study, it should be noted that we sample a wide range of cohesive forces to account for variability in these parameters. In other words, a single value of the cohesive force represents a variety of contact area and regolith strength pairs. In this way the results can

be applied to a variety of grain shape and regolith strength scenarios. This is particularly useful as the actual cohesive strength of regolith on asteroids is not known.

Note that because the cohesive force only acts on the grain while the particle is in contact with the surface, calculations involving cohesion are only used in determining initial condition requirements for dust lofting and is not actively modeled throughout the particle's trajectory.

4.3 Grain-Scale Supercharging

Traditionally, it has been difficult to show how dust grains are able to overcome cohesion using classical charge models, which distribute charge evenly across the surface of dust grains. However, recent advancements have led to development of the patched charge model which distributes charge unequally on the surfaces of grains and allows for accumulation of charge in the microcavities between grains [51]. Such models, which account for grain-scale charging, may explain how dust is able to overcome cohesion and gravity and loft in these conditions. In this study we assume grains resting in regolith charge according to this patched charge model. Specifically, we use the idealized scenario of two adjacent grains developed in Zimmerman et al. [62] where the surface of one sunlit grain photoemits electrons that are collected on the surface of a neighboring shadowed grain. This grain-scale supercharging produces a large electric field and grain charge that enables the dust grains to electrostatically loft from the surface. The details of this model are discussed next.

Zimmerman et al. [62] provides a few scenarios of dust grain interactions at the grain-scale that could lead to differential charging. See Figure 4.3 for reference.

A. Direct illumination of the topmost grain.

B. Direct illumination of small patches on the second layer of grains.

C. Illuminated patch adjacent to a shadowed facet.

D. Two illuminated facets adjacent to one another.

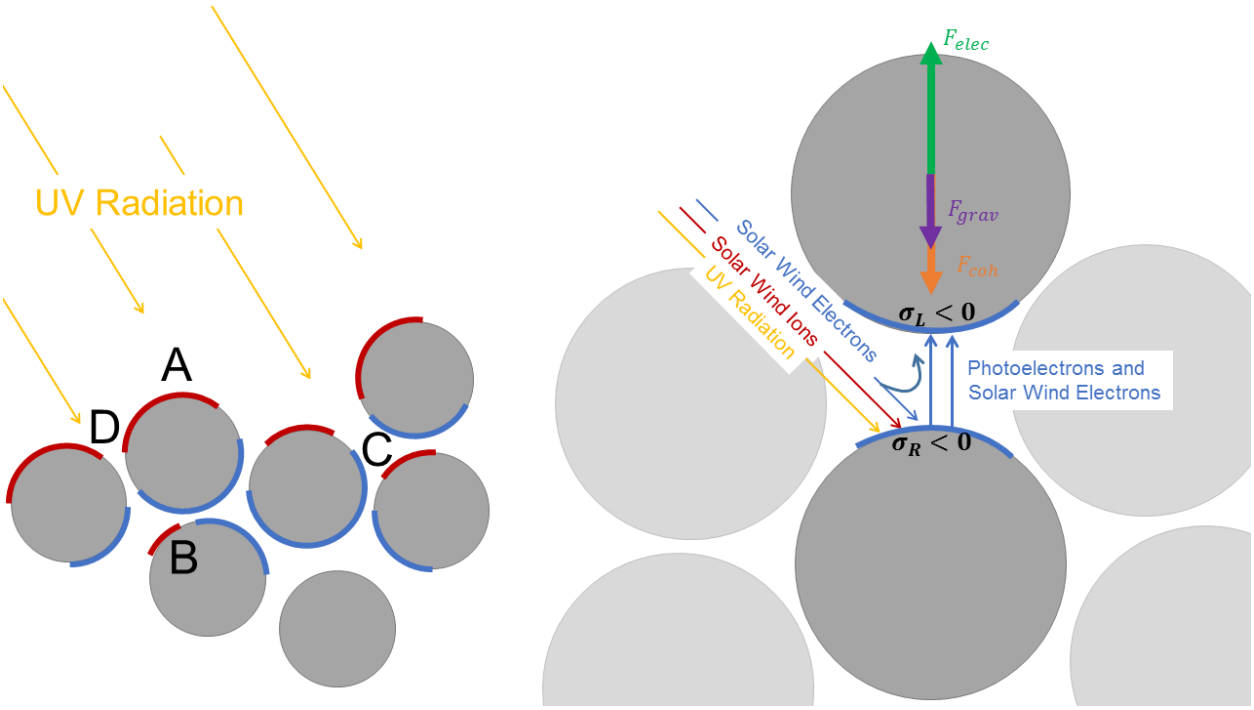

Figure 4.3: (Left) Scenarios of unequal charge distribution on dust grains at the surface. Red patches represent areas with positive charge (electron emitting surfaces), while blue patches represent areas with negative charge (electron receiving surfaces). (Right) Two negatively charged grains interacting near the surface. Forces acting on the dust grains are assumed to be collinear in this study, with the electrostatic force acting upwards (F_{elec}) and the gravitational (F_{grav}) and cohesive (F_{coh}) forces acting downwards. Note that depending on which model is used, the right grain can be positive (photoemission only) or negative (solar wind only and photoemission with solar wind). The photoemission with solar wind charging model is depicted here.

Parameters affecting the rate of electric field generation include: the characteristic scale length L of charge separation, grain charge Q_d, grain mass m_d, kinetic energy of the charged particles U, the emission flux J, the electric constant ε_0, and grain permittivity.

For the remainder of the analysis in this study, we will consider adjacent grains in scenario C, as is done in Zimmerman et al. [62]. Grains which charge negatively and repulse each other may lead to electrostatic lofting (shown in the right plot of Figure 4.3). Here we conservatively assume the forces are collinear with gravity and cohesion to simplify the problem and bound lofting requirements. Figure 4.4 shows the simplified geometry of two adjacent grains, whose charge areas are parallel.

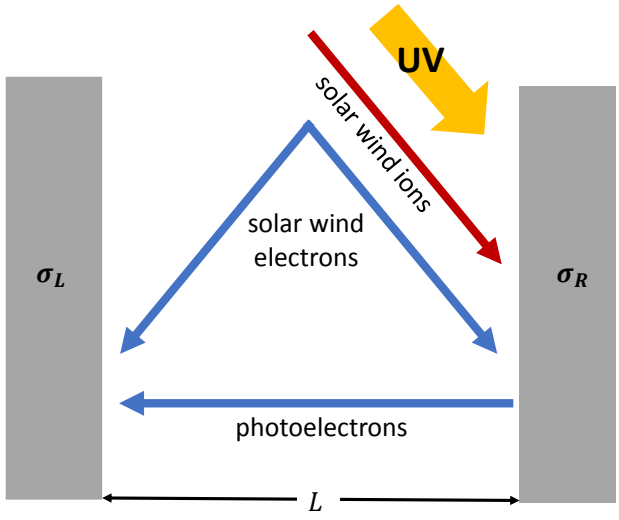

Figure 4.4: Idealized parallel surfaces charging on adjacent grains. Note that the solar wind ions are modeled as a (monoenergetic) beam incident only on the right wall, while the solar wind electrons and photoelectrons are omnidirectional (have an isotropic thermal distribution). [62]

The sign of the charge density will depend on the charge model used. For the photoemission model, the sunlit side constantly emits photoelectrons and gains a net positive charge, while the shadowed side collects an equal and opposite charge. This separation of charge produces an attractive electric field. However, for both the solar wind only model and the combined photoemission with solar wind model, the grain patches both

charge negatively, as will be shown below. In these cases, the resulting negative charge build-up on both patches is repulsive and may cause grains to electrostatically loft from the surface. Note that Zimmerman et al. [62] assumes a charge separation of $L = r_d/10$ and a charged patch area of L^2. We will use the numbers referenced in Zimmerman et al. [62] in any computations executed below, unless otherwise noted. See Table 4.1 for the relevant parameters.

Table 4.1: Parameters used in grain-scale supercharging equations. Note: A distance of 1AU is used where relevant.

Parameter	Symbol	Value
Freestream solar wind density	n_0	5×10^6 m^{-3}
Velocity of solar wind ions	v_{sw}	4×10^5 m/s
Velocity of solar wind electrons	v_{the}	$2x10^6$ m/s
Velocity of photoelectrons	v_{th}	6.5×10^5 m/s
Solar wind ion flux	J_i	3.2044×10^{-7} A/m^2
Solar wind electron flux	J_e	1.1359×10^{-6} A/m^2
Photoelectron flux	J_{pe}	4×10^{-6} A/m^2
Thermal kinetic energy of photoelectrons	U_{th}/e	1 eV
Grain conductivity	ϑ	10^{-13} Ω^{-1}m^{-1}

The first model Zimmerman et al. [62] develops is the photoemission only case, which assumes a Maxwellian distribution of electrons. For this case, the charge density changes as

$$\dot{\sigma} = J_{pe} \exp\left(-\frac{\Delta\sigma}{2\Sigma_p}\right) \qquad (4.8)$$

where $J_{pe} = 4 \times 10^{-6}$ A/m^2 is the photoelectron flux, σ is the grain charge density, and $\Sigma_p = \varepsilon_0 U_{th}/eL$ is the photoelectron charge density. Examining this photoemission only model, the total surface charge could theoretically grow without bound and is only limited

by the half rotation period of the primary body. While this model is too idealistic, it is a good place to build from.

To limit the charge growth in a realistic way, the effect of electrical conductivity of the grains is added. Draining of the surface charge through the grain is represented as a current density $j_\vartheta = \vartheta E_{int}$ where ϑ is the conductivity of the grain and E_{int} is the electric field inside the grain. In this idealized case (Figure 4.4), the grain-internal electric field would be equal and opposite to the electric field within the gap. As a result, the conductivity enters the charge equation as a sink term, and the modified photoemission with conductivity charging model is as follows.

$$\dot{\sigma}_R = J_{pe} \exp\left(-\frac{\Delta\sigma}{2\Sigma_p}\right) - \frac{\vartheta}{2\varepsilon_0}\Delta\sigma \qquad (4.9a)$$

$$\dot{\sigma}_L = -J_{pe} \exp\left(-\frac{\Delta\sigma}{2\Sigma_p}\right) + \frac{\vartheta}{2\varepsilon_0}\Delta\sigma \qquad (4.9b)$$

$$\Delta\dot{\sigma} \equiv \dot{\sigma}_R - \dot{\sigma}_L = 2J_{pe} \exp\left(-\frac{\Delta\sigma}{2\Sigma_p}\right) - \frac{\vartheta}{\varepsilon_0}\Delta\sigma \qquad (4.9c)$$

Integrating these equations over time with each grain starting at zero charge, Figure 4.5 gives the charge densities and charge density rates of both grains as a function of time.

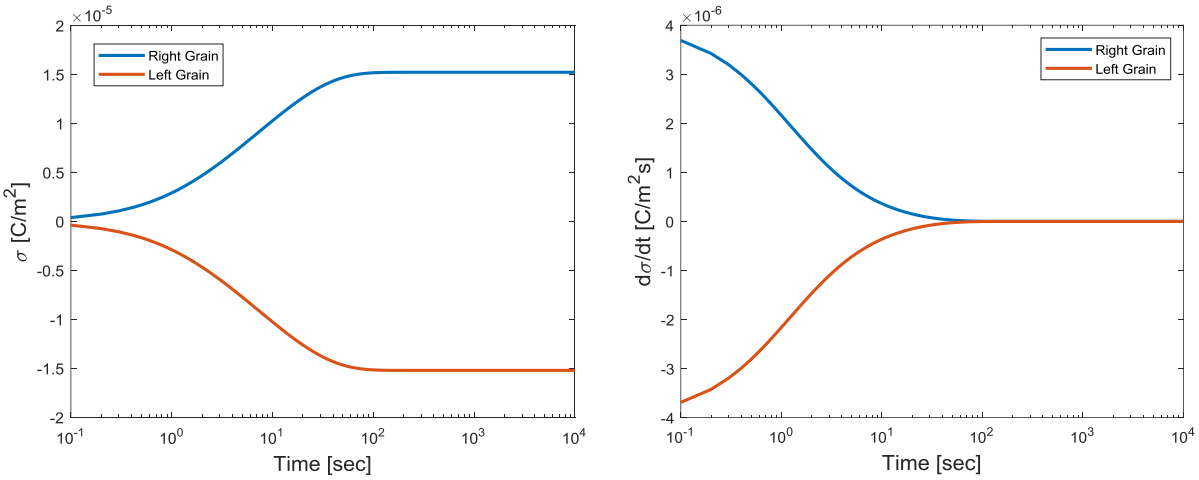

Figure 4.5: Charge density (left) and charge density rate (right) as functions of time for a 22-micron grain using the photoemission with conductivity model.

Here we see that the grains charge equally in magnitude but oppositely in sign—the right grain attains a positive charge density, while the left grain attains a negative charge density. Note that this would result in an attractive electrostatic force between grains.

Next, Zimmerman et al. [62] extends the idealized scenario to solar wind bombardment and derives the following charging equation accounting for solar wind and conductivity (without photoemission).

$$\dot{\sigma_R} = -J_e\left(2 - \exp\left(-\frac{\Delta\sigma}{\Sigma_e}\right)\right) + J_i - \frac{\vartheta}{2\varepsilon_0}\Delta\sigma \quad (4.10a)$$

$$\dot{\sigma_L} = -J_e \exp\left(-\frac{\Delta\sigma}{\Sigma_e}\right) + \frac{\vartheta}{2\varepsilon_0}\Delta\sigma \quad (4.10b)$$

$$\Delta\dot{\sigma} = 2J_e \exp\left(-\frac{\Delta\sigma}{\Sigma_e}\right) + J_i - 2J_e - \frac{\vartheta}{\varepsilon_0}\Delta\sigma \quad (4.10c)$$

Here $J_e = 2\sqrt{\pi}n_0 e v_{sw}$ is the thermal electron flux, $\Sigma_e = \varepsilon_0 m_e v_{the}^2/eL$ is the solar wind charge density, and $J_i = n_0 e v_{sw}$ is the thermal ion flux. Integrating these equations over time and starting with a zero charge on each grain, Figure 4.6 give the charge densities and charge density rates of both grains as a function of time.

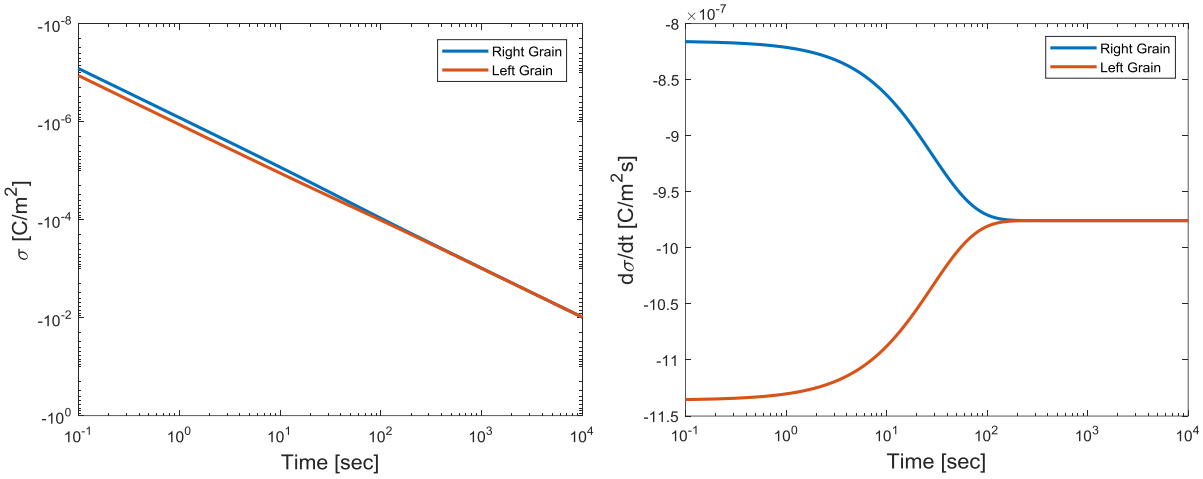

Figure 4.6: Charge density (left) and charge density rate (right) as functions of time for a 22-micron grain using the solar wind with conductivity model.

Here we see that both the right and left grains charge negatively, resulting in a repulsive electrostatic force. This type of repulsive force is what can lead to grain lofting. We also see that the charging rate slows near 10^2 seconds when equilibrium is reached.

Finally putting everything together, the wall-charging equation for simultaneous photoemission and solar wind bombardment with conductivity is

$$\dot{\sigma}_R = -J_e\left(2 - \exp\left(-\frac{\Delta\sigma}{\Sigma_e}\right)\right) + J_i + J_{pe}\exp\left(-\frac{\Delta\sigma}{2\Sigma_{pe}}\right) - \frac{\vartheta}{2\varepsilon_0}\Delta\sigma \quad (4.11a)$$

$$\dot{\sigma}_L = -J_e\exp\left(-\frac{\Delta\sigma}{\Sigma_e}\right) - J_{pe}\exp\left(-\frac{\Delta\sigma}{2\Sigma_{pe}}\right) + \frac{\vartheta}{2\varepsilon_0}\Delta\sigma \quad (4.11b)$$

$$\Delta\dot{\sigma} = 2J_e\exp\left(-\frac{\Delta\sigma}{\Sigma_e}\right) + 2J_{pe}\exp\left(-\frac{\Delta\sigma}{2\Sigma_{pe}}\right) + J_i - 2J_e - \frac{\vartheta}{\varepsilon_0}\Delta\sigma \quad (4.11c)$$

Starting with zero charge on both grains and integrating these equations over time, Figure 4.7 give the charge densities and charge density rates of both grains as a function of time.

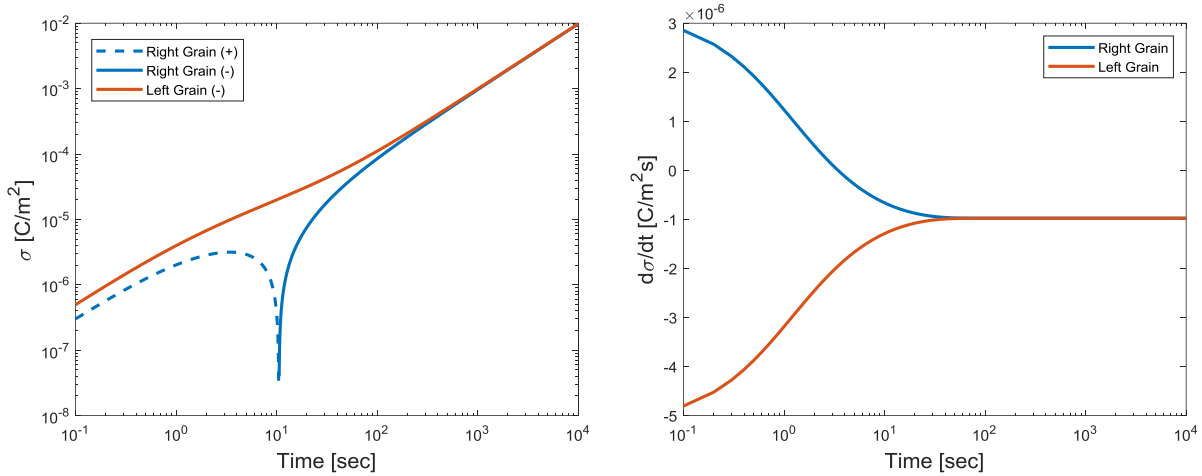

Figure 4.7: Charge density (left) and charge density rate (right) as functions of time for a 22-micron grain using the photoemission and solar wind with conductivity model.

Note in Figure 4.7 above that the absolute value of the charge density is plotted. At small times, the charge density of the right grain (in blue) is positive as photoemission acts to eliminate electrons from that grain. The downward spike indicates the time at which the right grain begins to charge negatively as the solar wind charging dominates. Both the

right and left grains in this model end up with negative charge densities as time increases. Again, we see that charging reaches an equilibrium prior to 10^2 seconds.

Both grains charging negatively is an interesting and nonintuitive result that appears to be an artifact of the unique interplay between photoemission and solar wind charging in the microcavities between grains, as modeled by Zimmerman et al. [62]. Performing a simple integration of the $\dot{\sigma}$ equations (4.11a and 4.11b) over time for the same 22-micron grain, Figure 4.8 gives the current density components over time. This enables us to directly see how the different particle populations are contributing to the charge densities of each grain over time.

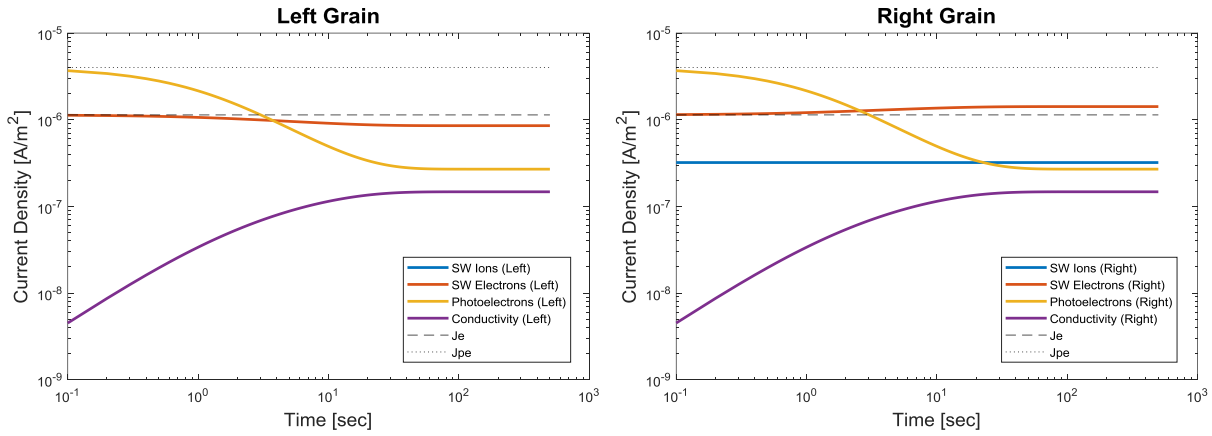

Figure 4.8: Current density component magnitudes over time for the left and right grains using the combined photoemission with solar wind supercharging model. The contribution from the solar wind ions is shown in blue, solar wind electrons in red, photoelectrons in yellow, and conductivity in purple. The solar wind electron flux J_e and photoelectron current flux J_{pe} are shown in dashed and dotted black lines, respectively, for reference. Note that only the magnitudes are plotted.

For the left grain, solar wind electrons (red) and photoelectrons (yellow) contribute to negative-charge build up; while conductivity (purple) inhibits it. For the right grain, the solar wind electrons (red) and conductivity (purple) contribute to negative-charge build up; while the photoelectrons (yellow) and solar wind ions (blue) inhibit it. Here we see that while the photoemission component dominates in the beginning, its significance diminishes over time. This is because photoemission reaches an equilibrium more quickly than solar wind electrons in this model. The solar wind electron component stays relatively stable

throughout the entirety of the integration and ends up dominating as time increases. These observations are also reflected in the left plot of Figure 4.7 when the right grain charge changes sign from positive to negative. The grain charges positively at early times when photoemission dominates, but ultimately charges negatively as the solar wind electrons dominate at later times. This is mathematically how the sun-lit grain charges negatively. Physically, this is a result of the grain-scale supercharging model developed by Zimmerman et al. [62].

For each of the models above, the electric field in the gap between grain patches is given by

$$E(t) = -\frac{\Delta\sigma(t)}{2\varepsilon_0} \quad (4.12)$$

where $\Delta\sigma(t)$ is the time-varying charge density difference between the two walls and ε_0 is the permittivity of free space. While the photoemission (without conductivity) case is unbounded, all the other charge density rate equations ($\Delta\dot{\sigma}$) given above will reach an equilibrium due to the conductivity sink term. This maximum charge density difference (related to the maximum gap electric field) can be solved for numerically by setting the charging rate $\Delta\dot{\sigma} = 0$ for a given grain radius and solving for the resulting charge density difference $\Delta\sigma$. These maximum gap electric field conditions are discussed in detail in Section 4.4.1. Figure 4.9 below shows the maximum gap electric field strength for the charge models discussed above. Note that various breakdown strengths are denoted on the plot. The effect of these breakdown levels will be discussed in more detail in Section 4.4.5 below.

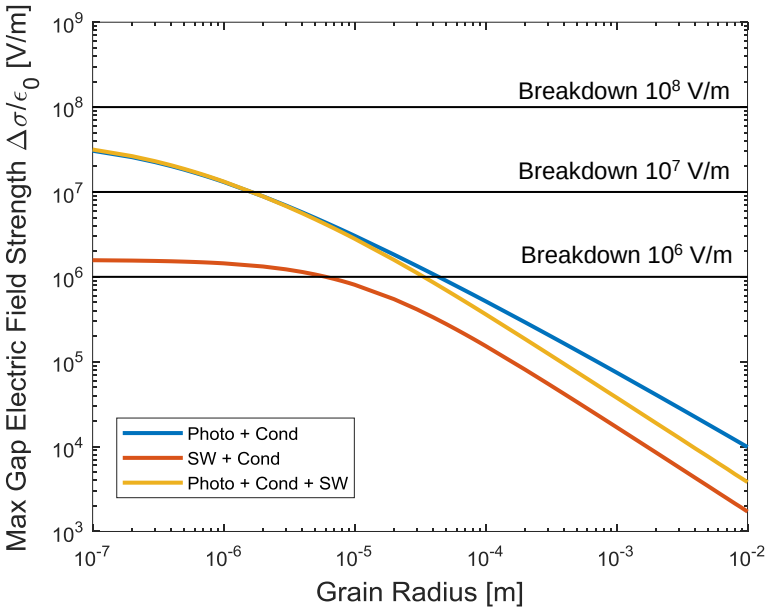

Figure 4.9: Maximum gap electric field strength as a function of grain radius for three different supercharging models—photoemission only is shown in blue, solar wind only in red, and photoemission with solar wind in yellow.

Next, we plot the associated charge densities on the right and left grain patches when the gap electric field is maximum for each of the three models. The results are plotted as a function of grain radius in Figure 4.10.

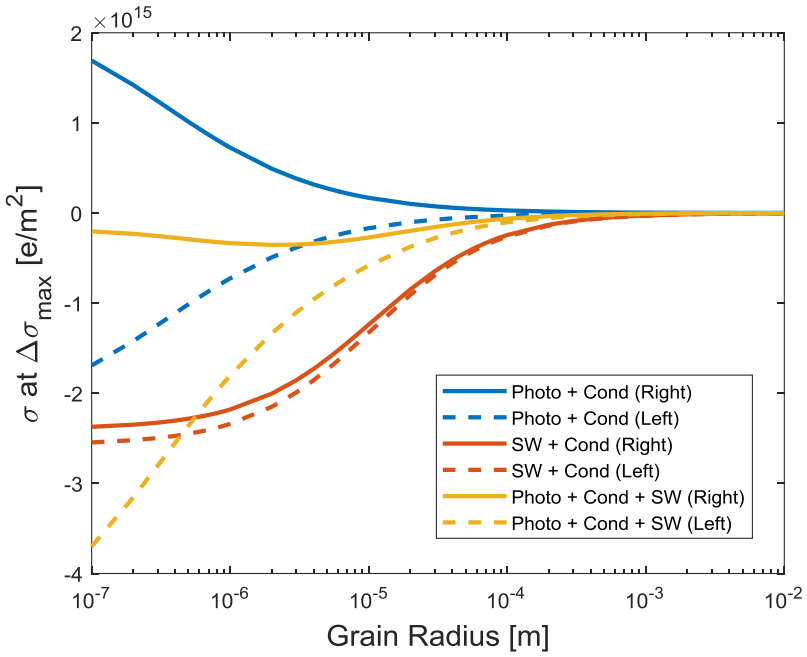

Figure 4.10: The associated grain charge densities when the gap electric field strength is maximum for three different models. The photoemission only model is plotted in blue, the solar wind only model is plotted in red, and the photoemission with solar wind model is plotted in yellow.

Note here that the photoemission only model produces an attractive electric field (grains are oppositely charged), while the solar wind only model and the photoemission with solar wind model produce repulsive electric fields (grains are like-charged). Also, as the grain size increases, the charge density at the maximum gap electric field condition approaches an asymptote.

Additionally, we can compute the time dependence of the electric field experienced by one wall as a result of the other wall by integrating any of the charge density equations above and dividing by the permittivity of free space ε_0.

$$E(t) = \frac{\sigma(t)}{2\varepsilon_0} \quad (4.13)$$

Here, the right wall experiences an electric field of $E = -\sigma_L/\varepsilon_0$ due to the charge density of the left wall, while the left wall experiences an electric field of $E = \sigma_R/\varepsilon_0$ due to the charge density of the right wall. Note the important difference between equations 4.12

and 4.13. In equation 4.12, a test particle placed between the two charged walls experiences an electric field dependent on the electric field of both walls ($\Delta\sigma$); while in equation 4.13, each wall only experiences an electric field from the opposing wall and is not influenced by its own electric field (σ).

We can also compute the time rate of change of the grain charge using the assumed charge patch area.

$$Q(t) = \sigma(t)L^2 \quad (4.14)$$

This further enables calculation of the electrostatic force felt between the adjacent grains.

$$F_{elec}(t) = Q(t)E(t) = \sigma_L(t)L^2\frac{\sigma_R(t)}{2\varepsilon_0} \quad (4.15)$$

Equating the electrostatic force to various external forces, Zimmerman et al. [62] numerically computes exposure times required to overcome various levels of cohesion and gravity on different primary bodies for each of the models above. The models dominated by photoemission reach maximum gap electric field strength within 10^2 seconds or less, while the solar wind only model reaches maximum gap electric field strength within 10^3 seconds or less [62]. Thus, grains undergoing this grain-scale supercharging reach their maximum gap electric field strengths relatively quickly—within minutes rather than hours. This suggests that grain charging is not limited to typical asteroid rotation periods, which are on the order of a few hours or longer. Instead grain-scale supercharging happens much more quickly, enabling grains to reach lofting requirements theoretically at many points throughout the local day, depending on local surface illumination conditions.

To verify that these models did indeed reach their maximum charge densities quickly, we integrated the charge densities over time for four different grain sizes—1 micron, 10 microns, 100 microns, and 1000 microns. The results are shown in Figure 4.11 below.

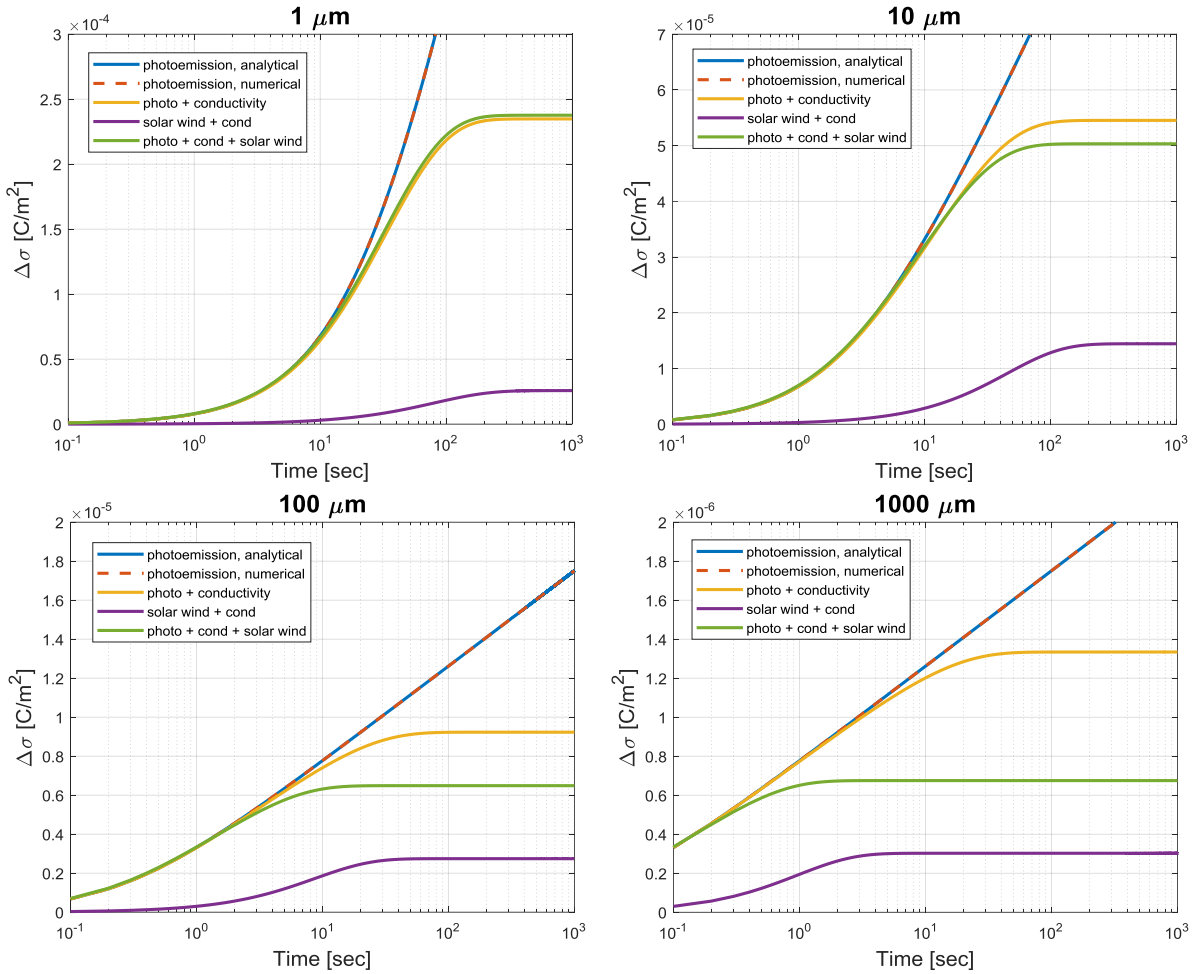

Figure 4.11: Charge density differences over time using the models described above for a range of particle sizes—1 micron, 10 microns, 100 microns, 1000 microns. The photoemission model is shown in yellow, the solar wind model in purple, and the combined photoemission with solar wind model in green. The unbounded photoemission only model (no conductivity) is shown in solid blue (analytical) and dashed red (numerical) for comparison.

As expected, maximum charge values are reached quickly—roughly within 10^2 seconds for all four cases. These results align with those presented in Zimmerman et al. [62] for exposure times.

From our evaluation here of the charging models presented in Zimmerman et al. [62], we are able to conclude that (1) this more realistic grain-scale model of charging leads to a maximum gap electric field strength as a function of grain size, and (2) the time to reach this maximum gap electric field strength is relatively short when compared to typical

asteroid rotation periods. This leads us to investigate in the following section how each of the charging models discussed above can be used to bound initial condition requirements such as charge and velocity for dust lofting on small bodies in the Solar System. Specifically, we examine simplified models for Bennu, Itokawa, Ryugu, Eros, and the Moon. Relevant parameters for each of the bodies are given in Table 4.2 below.

Table 4.2: Relevant parameters for the small bodies of interest.
Parameter references for Itokawa [13], Bennu [28], Ryugu [23, 52], Eros [58, 64], and the Moon [46, 54].

Body Name	**Mass**	**Mean Radius**	**Surface Gravity**	**Surface Escape Speed**
Itokawa	3.51×10^{10} kg	173 m	7.8×10^{-5} m/s^2	16 cm/s
Bennu	7.329×10^{10} kg	245 m	8.1×10^{-5} m/s^2	20 cm/s
Ryugu	4.50×10^{11} kg	460 m	1.4×10^{-4} m/s^2	36 cm/s
Eros	6.687×10^{15} kg	7311 m	8.3×10^{-3} m/s^2	11 m/s
Moon	7.34767×10^{22} kg	1737.7 km	1.6 m/s^2	2376 m/s

4.4. Initial Conditions for Supercharged Grains

Dust grain behavior is very sensitive to initial conditions, and thus a method of determining realistic lofting requirements using new grain-scale supercharging models is the focus of this section. As discussed previously, these lofting requirements are set by the local cohesive and gravitational environments at the surface, as discussed in Section 4.1.

First, we compare the supercharging models described above and solve for the maximum gap electric field conditions. We then develop a method of calculating dust grain initial conditions, such as charge and ejection speed, required for lofting under a variety of surface conditions. Finally, we examine the sensitivity that factors such as charge separation, regolith cohesion, and dielectric breakdown have on dust grain charging.

4.4.1 Maximum Gap Electric Field Conditions

Here we examine the two charging models which lead to a repulsive electrostatic force between grains—solar wind only (equation 4.10) and photoemission with solar wind (equation 4.11)—over a range of grain sizes, regolith cohesions, and primary body sizes. For the analysis in this subsection, we assume a grain charge separation of $L = r_d/10$, following Zimmerman et al. [62] for consistency.

First, we solve for the maximum gap electric field as a function of grain size, assuming the idealized geometry shown in Figure 4.4 above. Solving for the value of charge density $\Delta\sigma$ when the charge density rate $\Delta\dot{\sigma}$ goes to zero for the three models, we find the following trends in Figure 4.12.

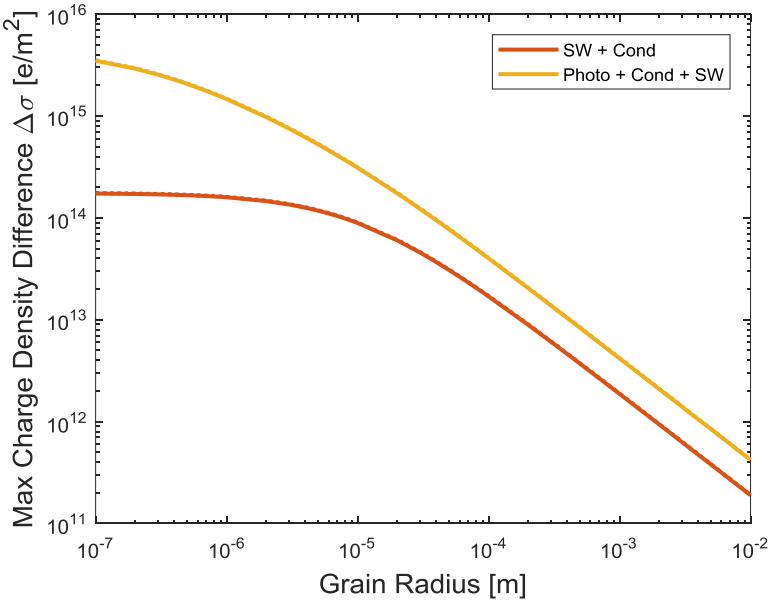

Figure 4.12: Maximum charge density difference for a range of grain sizes using two different charging models. The solar wind model is shown in red and the combined photoemission with solar wind model is shown in yellow.

From the figure above, we see that the maximum charge density difference decreases as grain size is increased. Assuming a charging area of L^2, we can then compute the associated charge a grain could acquire at these conditions using equation 4.14, $Q_{max} = \sigma_{max} L^2$. These grain charge values are plotted over a range of grain sizes in Figure 4.13.

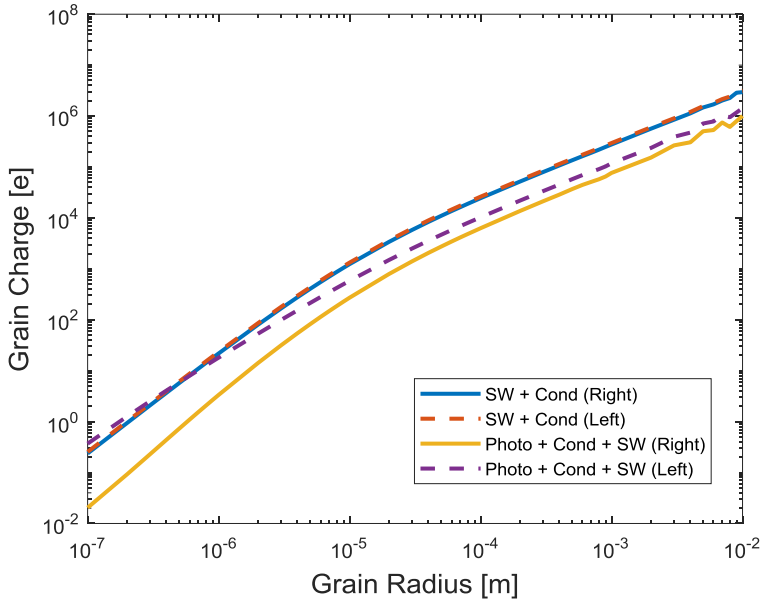

Figure 4.13: Right and left grain charge (associated with the maximum gap electric field) over a range of grain sizes using two different charging models. The solar wind model is shown in blue (right grain) and red (left grain), while the combined photoemission with solar wind model is shown in yellow (right grain) and purple (left grain). Note that the charges have a negative sign and only their magnitudes are plotted.

Note here that the individual charge densities are integrated forward in time until the maximum charge density difference is reached. As the grain size increases, this maximum gap charge difference occurs closer to the initial charge density difference. This explains why the trend lines in Figure 4.13 become more jagged at larger grain radii—the maximum charge density difference is less well defined for larger grains.

Overall, we see that the associated charge increases for increasing grain radii. For micron sized particles, the maximum grain charge is found to be on the order of 10^{-17} to 10^{-16} C, depending on which model is used. Again, it's also important to note the timescale over which these charge densities occur. From Section 4.3, we know that supercharging rates are maxed out very quickly, on the order of 10^2 seconds or less. Thus, we can assume that grains reach these charge values quickly. As a result, those that can overcome their local gravitational and cohesive environments may be able to loft at multiple points throughout the day.

4.4.2 Surface Conditions for Electrostatic Lofting

Next, we look at the conditions under which dust grains loft, namely how the electrostatic force compares to the forces of gravity and cohesion holding the grain to the surface. We note that at the moment just prior to lofting, the electrostatic force will exactly equal the combined cohesive and gravitational forces (see equation 4.3). Using this knowledge, we can solve for different lofting requirements.

Recall from equation 4.15 that we can calculate the electrostatic force using the charge densities of both walls (σ_L and σ_R) and the charged patch area (L^2). The electrostatic force associated with the maximum gap electric field strength can be computed in this same way using the maximum charge density difference plotted in Figure 4.12. The associated electrostatic force for each model over a range of grain radii is plotted in Figure 4.14 below. On the same plot we include gravitational forces for a range of small bodies (Bennu, Itokawa, Ryugu, Eros, and the Moon) assuming spherical dust grains, as well as a range of regolith cohesive forces.

Here the gravitational force is

$$F_{grav} = m_d g = \frac{4}{3}\pi r_d^3 \rho_d g \qquad (4.16)$$

where m_d is the grain mass, g is the gravitational acceleration at the surface, r_d is the grain radius, and ρ_d is the grain density (assumed to be 2.4 g/cm^3 to mimic the grain density of Bennu [28]). We do not account for rotation of the small body via the centripetal acceleration term in the results of this chapter. However, an effective gravity force that does account for the rotation is used in the small body simulation results discussed in Chapter 5. The cohesive force is calculated using equation 4.7 in Section 4.2. Recall that we assume half the grain surface area is in contact with the cohesive matrix of smaller grains, as described in Sánchez and Scheeres [41].

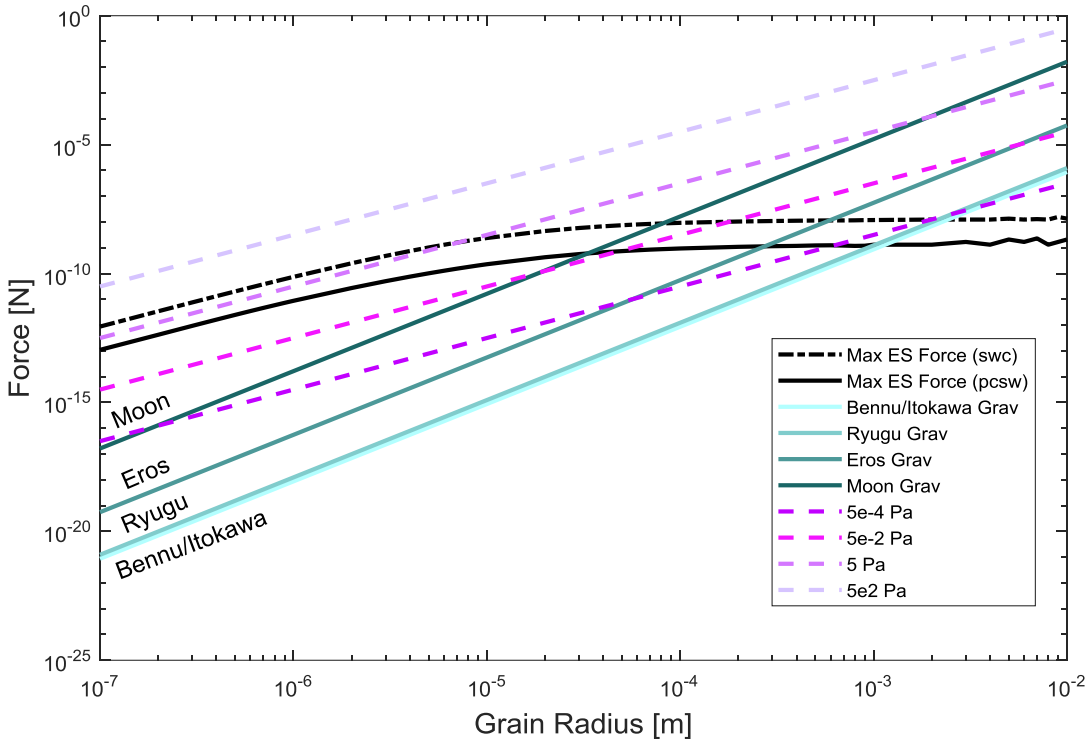

Figure 4.14: The electrostatic force associated with the maximum gap electric field over a range of grain sizes for two different charging models—solar wind only in a dash-dotted black line and combined photoemission with solar wind in a solid black line. A range of gravitational forces is plotted in various shades of solid teal, while a range of cohesive forces is plotted in various shades of dashed purple.

From this plot, we see that a limit exists, past which certain grain sizes will not be able to overcome the local cohesive or gravitational forces experienced at the surface. Any grain experiencing gravitational or cohesive forces above the electrostatic force lines plotted would not be loftable. For instance, for grains in the microns to tens of microns range, a combination of gravity and cohesion forces with magnitudes above 10^{-9} N would not be loftable.

Solution of the associated electrostatic force (Figure 4.14) also bounds the cohesive strength a grain can overcome on a given small body. Thus, if we insert the necessary parameters at the maximum gap electric field condition into equation 4.3, we can solve for this associated cohesive strength.

$$\sigma_{y,max\ \Delta\sigma} = \frac{F_{elec,max\ \Delta\sigma} - F_{grav}}{2\pi r_d^2} = \frac{\sigma_L \sigma_R}{4\pi\varepsilon_0}\left(\frac{L}{r_d}\right)^2 - \frac{2}{3}\rho_d g r_d = \frac{\sigma_L \sigma_R}{400\pi\varepsilon_0} - \frac{2}{3}\rho_d g r_d \qquad (4.17)$$

Recall here that σ_y refers to the cohesive strength of regolith, while σ refers to the charge density of a dust grain. The cohesive strengths associated with the maximum gap electric fields are plotted against grain size in Figure 4.15.

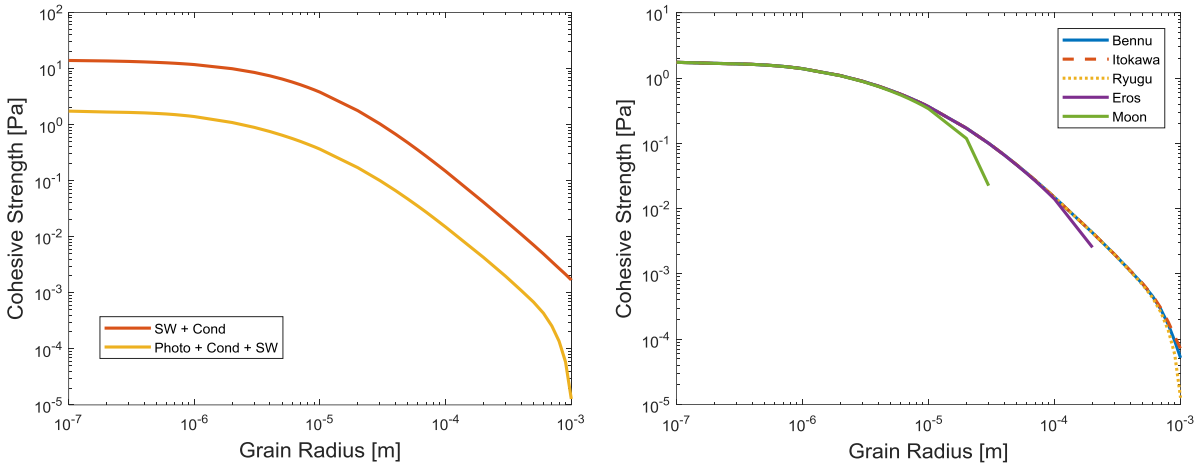

Figure 4.15: Cohesive strength (at maximum gap electric field condition) as a function of grain size. (Left) Values shown for two different charging models—solar wind in red and combined photoemission with solar wind in yellow—for grains on a single primary body, Ryugu. (Right) Values shown for grains on a variety of primary bodies—Bennu in blue, Itokawa in red, Ryugu in yellow, Eros in purple, and the Moon in green—for a single charging model (combined photoemission with solar wind).

The plot on the left gives the cohesive strengths for the two different charging models on a single primary body (Ryugu) at the maximum gap electric field condition, while the plot on the right gives the cohesive strengths for five different primary bodies using a single charging model (combined photoemission with solar wind). Overall, we see that the associated cohesion decreases with increasing grain size, which is primarily due to the charge density product term $\sigma_L \sigma_R$ (both decrease with increasing grain size). Note also that the data terminates when the gravity term is large enough so that the cohesion goes to zero. This termination point bounds not only the effect of cohesion on dust lofting, but also of grain radius and primary body size, thus providing clarity on the unique interplay of the three parameters on dust lofting requirements.

We can also examine the same comparisons for accelerations that we did for forces, by dividing by the grain mass. These accelerations are shown in Figure 4.16. Recall we are using spherical grains with a grain density of 2.4 g/cm^3.

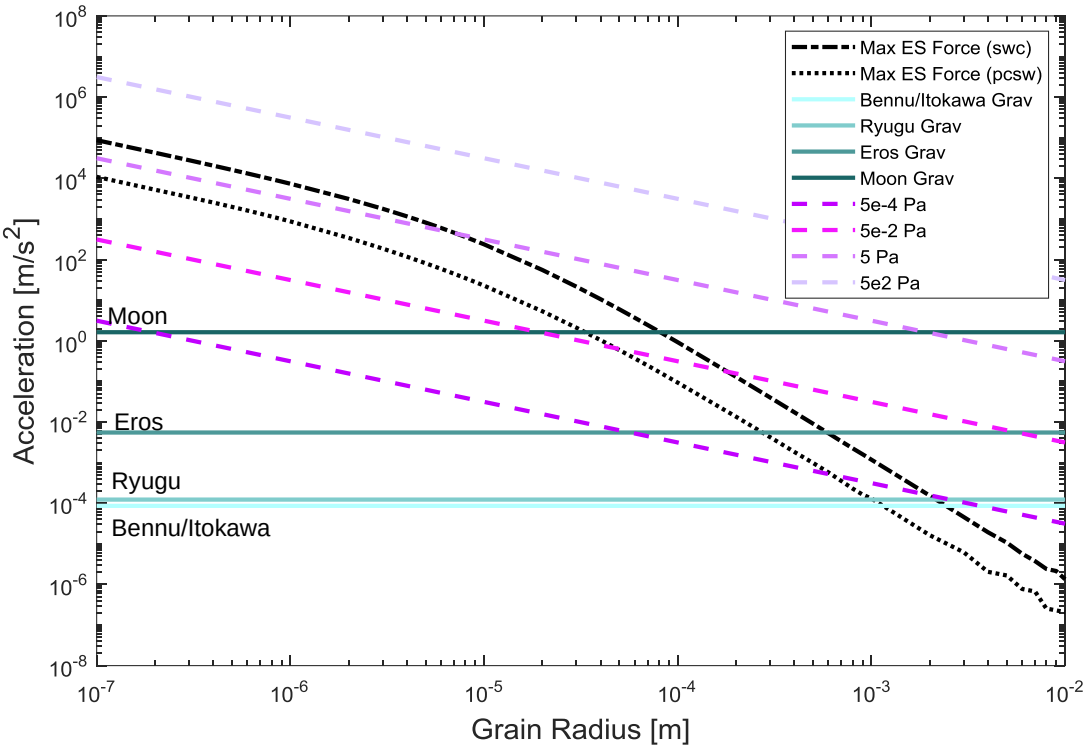

Figure 4.16: Electrostatic accelerations associated with the maximum gap electric field over a range of grain sizes for two different charging models—solar wind only in a dash-dotted black line and combined photoemission with solar wind in a solid black line. A range of gravitational accelerations is plotted in various shades of solid teal, while a range of cohesive accelerations is plotted in various shades of dashed purple.

Again, we note that any grains with combined gravitational and cohesive accelerations above the maximum electrostatic accelerations are not loftable. Furthermore, we see that electrostatic and cohesive accelerations decrease with increasing grain radii. This means that smaller grains can overcome larger cohesions and experience a larger initial acceleration at surface separation as a result. For instance, micron-sized grains can overcome cohesive forces with strengths near 5 Pa, whereas grains in the tens of microns range can only overcome cohesion strengths near 0.5 Pa.

Overall, in this section we have developed a method of solving for maximum gap electric field conditions for a variety of grain-scale charge models and used these conditions to bound lofting requirements for a range of grain sizes and surface properties. In the next section we will develop a method of computing lofting ejection speeds for these grains. Because the combined photoemission with solar wind model is the most complete of the charging models examined, we will use this model in the remainder of our analysis presented below.

4.4.3. Ejection Speed

Using the accelerations in Figure 4.16, we can directly calculate initial velocity conditions for electrostatic lofting of grains from the surface. In this section, we will use the combined photoemission with solar wind model for our analysis.

Recall that lofting of a grain occurs when the electrostatic force is greater in magnitude than the combined gravitational and cohesive forces holding the grain down to the surface (see Section 4.1). Here we assume the forces are aligned, as shown in Figure 4.3, which provides a conservative estimate for our results. From our knowledge of the force balance just prior to and immediately after a grain's separation from the surface (equations 4.4 and 4.5), we know that the net acceleration experienced by a lofted grain is related to the regolith cohesive strength it overcame.

$$a_{coh} = \frac{F_{coh}}{m_d} = \frac{3}{2}\frac{\sigma_y}{\rho_d r_d} \qquad (4.18)$$

Assuming supercharging only affects grain motion within a few radii of the surface and conservatively assuming a constant acceleration over this small distance, we can solve for the initial velocity of the grain once it breaks its cohesive bonds.

$$v_0 = \sqrt{2a_{coh}(xr_d)} = \sqrt{3x\frac{\sigma_y}{\rho_d}} \qquad (4.19)$$

Here we use the coefficient x to denote the number of grain radii over which the constant acceleration acts. For comparison, Figure 4.17 shows how the initial velocity would change for varying distances over which the supercharging acts ($1\,r_d, 2\,r_d, 3\,r_d$) for a range of grain sizes on asteroid Ryugu.

Examining the initial velocity requirement at maximum gap electric field conditions, we find the following relation with particle size.

$$v_{0,max\,\Delta\sigma} = \sqrt{3x\frac{\sigma_{y,max\,\Delta\sigma}}{\rho_d}} = \sqrt{\frac{3x}{4}\frac{\sigma_L\sigma_R}{\pi\varepsilon_0\rho_d}\left(\frac{L}{r_d}\right)^2 - 2xgr_d} \qquad (4.20)$$

Note here that the $\sigma_{y,max\,\Delta\sigma}$ term will also have dependence on the grain radius through the separation distance $L = r_d/10$, specifically in the Σ_{pe} and Σ_e terms within the charge density rates $\dot{\sigma}_R$ and $\dot{\sigma}_L$.

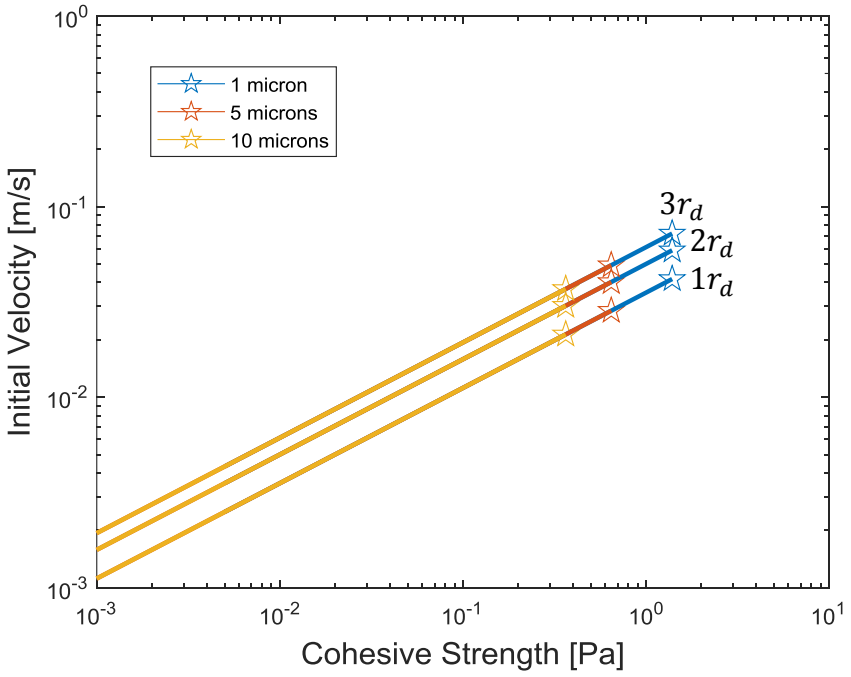

Figure 4.17: Initial velocity as a function of cohesive strength for different grain sizes. This data assumes three different distances over which the supercharging acceleration acts (see equation 4.17). The stars denote maximum gap electric field conditions for each of the three dust grain sizes. The maximum condition velocities use asteroid Ryugu as the primary body. Recall that these maximum condition solutions require selection of a primary body (see gravity dependence in equation 4.18).

From the plot above, we see that increasing the distance over which the supercharging acceleration occurs will increase the initial velocity of the grain slightly; however, overall, the values are comparable for each of the different distances. It's also interesting to note that in our formulation, the initial velocity calculation is independent of grain size, except when computing the initial velocity at maximum gap electric field conditions (i.e. placement of the stars in Figure 4.17). Note also that the maximum gap electric field conditions require selection of a primary body, as evidenced in the gravity dependence of equation 4.20. For the sake of Figure 4.17, we chose Ryugu as our primary body. Given the results of the plot above, we move forward using a distance of two grain radii ($x = 2$) over which the supercharging force acts.

Looking at the $v_{0,max\,\Delta\sigma}$ in more depth, we can separate this quantity into two separate parts.

$$v_{0,max\,\Delta\sigma} = \sqrt{\frac{3\sigma_L\sigma_R}{200\pi\varepsilon_0\rho_d} - 4gr_d} = \sqrt{V_{max}^2 - 4gr_d} = V_{max}\sqrt{1 - \frac{4gr_d}{V_{max}^2}} \qquad (4.21)$$

Here V_{max} represents the maximum initial velocity a lofted grain will experience without consideration to gravity

$$V_{max}^2 = \frac{3}{2}\frac{\sigma_L\sigma_R}{\pi\varepsilon_0\rho_d}\left(\frac{L}{r_d}\right)^2 = \frac{3\sigma_L\sigma_R}{200\pi\varepsilon_0\rho_d} \qquad (4.22)$$

while the remaining factor is a correction term that maintains a dependence on gravity. By separating the initial velocity into these two separate parts—one independent of gravity—we can generalize our initial velocity findings to a variety of small bodies. In fact, this V_{max} quantity is the largest contributor to the initial velocity and is plotted as a function of grain size in Figure 4.18 below.

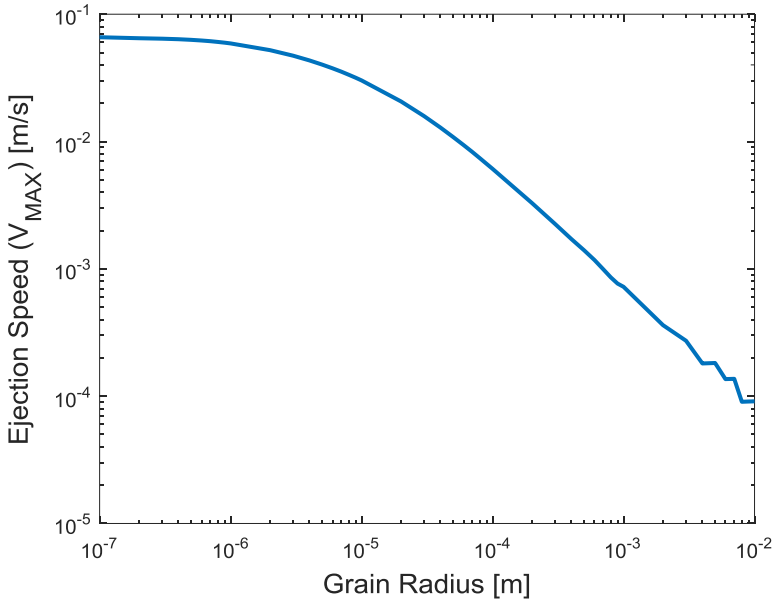

Figure 4.18: Initial velocity V_{max} as a function of grain radius. Note that V_{max} is the primary contributing factor to the initial velocity calculation at maximum gap electric field conditions and is independent of the gravity.

Here we see that the initial velocity decreases as grain size is increased, indicating that it should be easier for smaller grains to be lofted to escape. For Ryugu, the local escape speed from the surface is on the order of 0.4 m/s ignoring rotation (which will decrease it). Thus, the smallest grains are susceptible to being directly ejected. We note that once a particle is lofted, additional forces such as solar radiation pressure are also effective in stripping away smaller particles.

Next, we examine the second part of equation 4.21, specifically looking at when $\sqrt{1-\frac{4gr_d}{V_{max}^2}}$ goes to zero. This represents a grain which has acquired sufficient charge to exactly cancel gravity and cohesion, and as a result experiences zero initial velocity. Using this relation, we can solve for the maximum gravity allowable for a lofted dust grain. In this way we can constrain the size of primary body that grains of a given size could loft from.

$$g_{max} = \frac{V_{max}^2}{2xr_d} = \frac{V_{max}^2}{4r_d} \qquad (4.23)$$

This maximum gravity value is shown in Figure 4.19 below as a function of grain size.

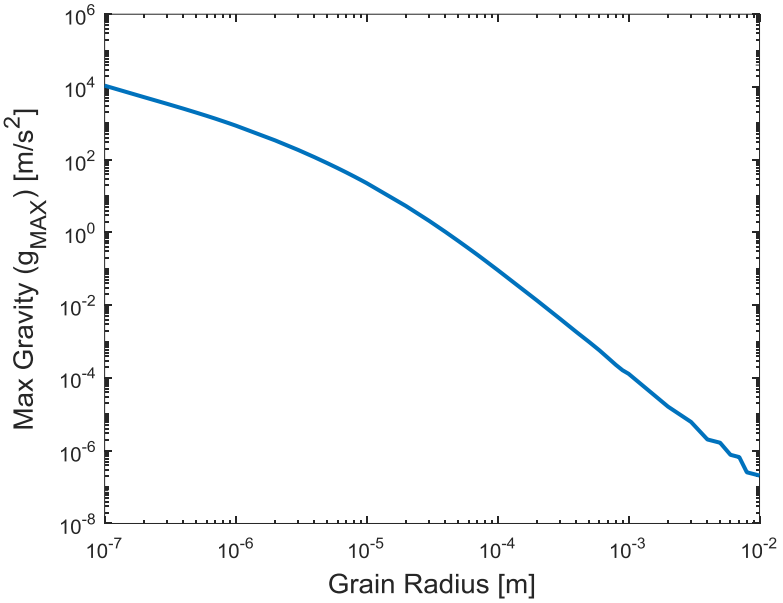

Figure 4.19: Maximum gravitational acceleration as a function of grain radius. This maximum gravity is associated with the moment when a grain's electrostatic force exactly cancels those of gravity and cohesion at the maximum gap electric field conditions (zero initial velocity).

Here we notice that the maximum gravity becomes large, making this a non-essential quantity and implying that the lofting speed is most strongly a function of the V_{max} parameter.

In this section we have developed a method of computing the initial speed with which lofted dust grains come off the surface. Additionally, we have computed this velocity at the maximum gap electric field condition, which bounds grain lofting initial conditions. We have also generalized the results to be independent of gravity for application to a wider range of bodies in the Solar System. In the next sections we will survey how certain parameters in the charging models affect grain charging.

4.4.4 Effect of Charge Separation

Here we examine how the characteristic scale length of charge separation L affects grain charging. Note that this study uses the combined photoemission with solar wind charging model.

Assuming again that the charge area on each grain is directly related to the charge separation through $A = L^2$, we vary the characteristic scale length L and compute the maximum charge density difference over a range of grain sizes. Figure 4.20 below gives the results for three different lengths—r_d, $r_d/10$, and $r_d/100$.

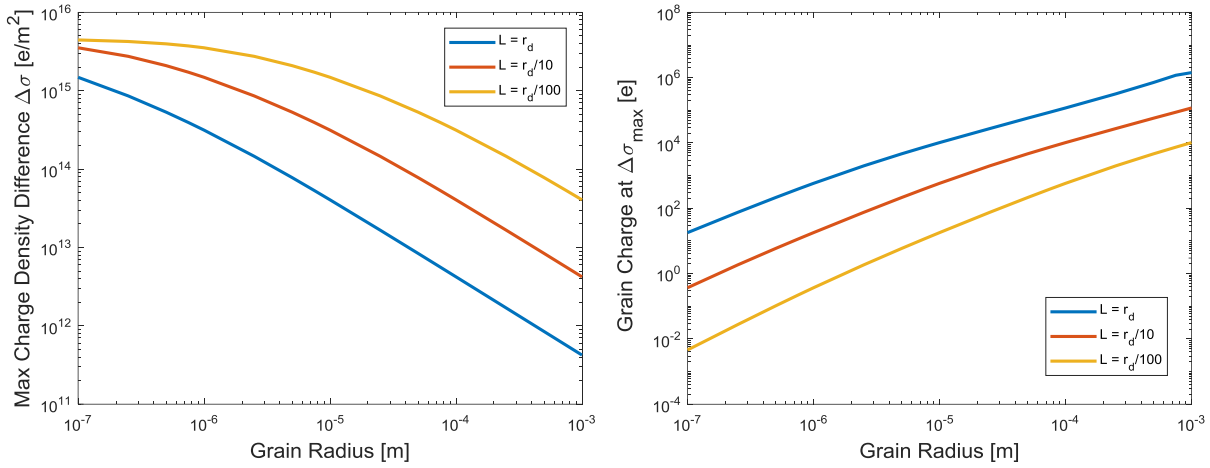

Figure 4.20: Maximum charge density difference (left) and the associated grain charge (right) versus grain radius for three different charge separation distances. A charge separation of $L = r_d$ is plotted in blue, $L = r_d/10$ in red, and $L = r_d/100$ in yellow.

Here in the left plot of Figure 4.20, we see that as the characteristic scale length for charge separation is decreased, the maximum charge density difference increases. Assuming that the charge area is related to the scale length as $A = L^2$, it is unsurprising that the maximum grain charge decreases with decreasing scale length, as shown in the right plot. Thus, grains with smaller charge separations will reach higher maximum charge density differences but acquire lower overall grain charges.

Solving for the associated electrostatic force, Figure 4.21 shows the results.

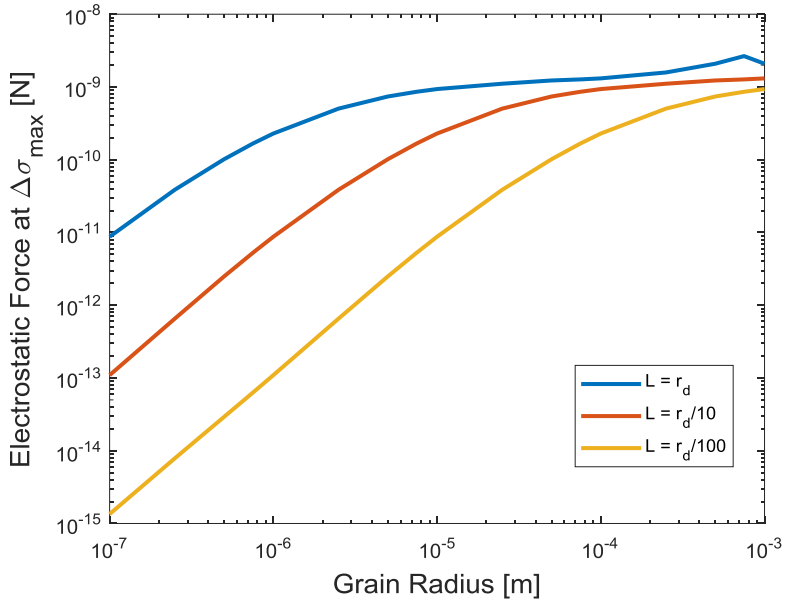

Figure 4.21: The electrostatic force associated with the maximum gap electric field as a function of grain radius for three different charge separation distances. A charge separation of $L = r_d$ is plotted in blue, $L = r_d/10$ in red, and $L = r_d/100$ in yellow.

Here we see that smaller charge separation yields smaller electrostatic forces. This means that grains with smaller charge separations will be more limited in the surface conditions they can overcome, when compared to grains with larger charge separations. As a result, grains with smaller charge separations won't be able to overcome the same cohesions as grains with larger charge separations, which will limit their upward lofting speed (see Figure 4.18). This effect, however, diminishes as grain size increases. Next, we look at the associated initial velocity as a function of grain size for the different charge separations in Figure 4.22.

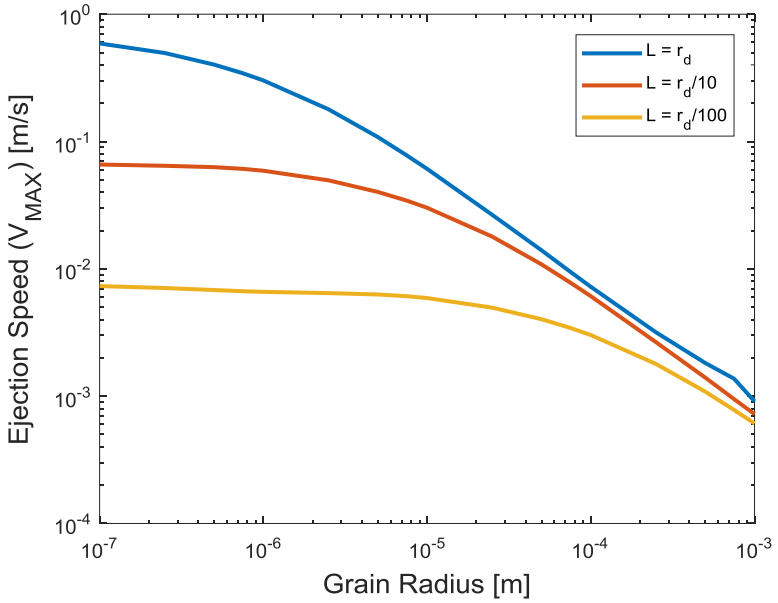

Figure 4.22: Maximum initial velocity V_{max} as a function of grain radius for a range of charge separation distances. Note that V_{max} is independent of primary body size (and gravity). A charge separation of $L = r_d$ is plotted in blue, $L = r_d/10$ in red, and $L = r_d/100$ in yellow.

We see that the associated lofting velocity decreases as the grain size increases. Additionally, as the charge separation distance decreases, the initial velocity also decreases. This is expected, as we noted from Figure 4.21, that grains with smaller charge separations will experience smaller electrostatic forces and will only be able to loft from regolith with lower cohesive strengths as a result. This is due to the fact that the initial velocity is directly related to the cohesive force (equation 4.19). However, this relationship fades as the grain size is increased, at which point the various charge separation distances produce equivalent results.

Overall, we find that more compactly situated grains (those with smaller charge separation) will reach higher maximum charge densities but lower overall grain charges. The effect of this on lofting means that grains with smaller charge separations will experience smaller electrostatic forces and will be more limited in the surface conditions they can loft from (lower cohesive strengths), when compared to grains with larger charge

separations. However, the effect of charge separation on the ability of grains to loft diminishes as grain size is increased.

4.4.5 Effect of Dielectric Breakdown

In this section, we examine how the dielectric breakdown strength affects charging behavior. Dielectric breakdown is an intrinsic property of the grain material. Breakdown occurs when the electric field inside the grain becomes large enough that the grain begins to act as a conductor and current is transferred from one wall to the other instantaneously. Breakdown strengths between 10^6 V/m and 10^8 V/m [3, 12, 47] are cited as realistic bounds for our study here. From Figure 4.9 above, we see that a breakdown level of 10^8 V/m should not affect the supercharging values. However, we will next analyze how breakdown levels of 10^6 V/m and 10^7 V/m affect grain charging and lofting.

Looking first at a breakdown strength of 10^7 V/m, we plot the maximum gap electric field strengths in Figure 4.23. Note that because the electric field inside the grain is equal and opposite to that in the gap between grains, this analysis can be performed using the gap electric field calculations.

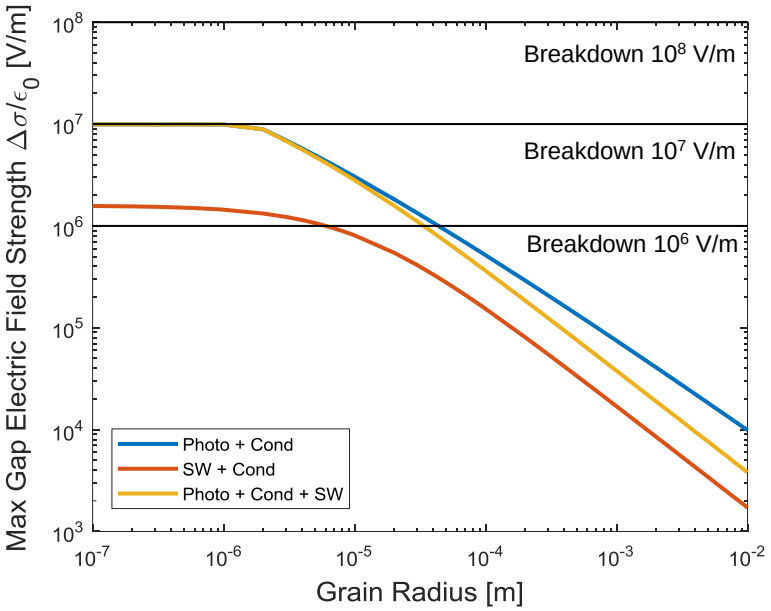

Figure 4.23: Maximum electric field strength as a function of grain radius for three different supercharging models—photoemission only is shown in blue, solar wind only in red, and photoemission with solar wind in yellow. Here a breakdown strength of 10^7 V/m is used as an upper bound on grain charging.

From this plot we see that only the photoemission and photoemission with solar models are affected by the breakdown strength for grain sizes below 2 microns in radius. Next, we plot the charge density associated with the maximum electric field and the resulting ejection speed in Figure 4.24. Note that only the ejection speeds for the solar wind only and the combined photoemission with solar wind models are given since those are the only models which can result in lofting.

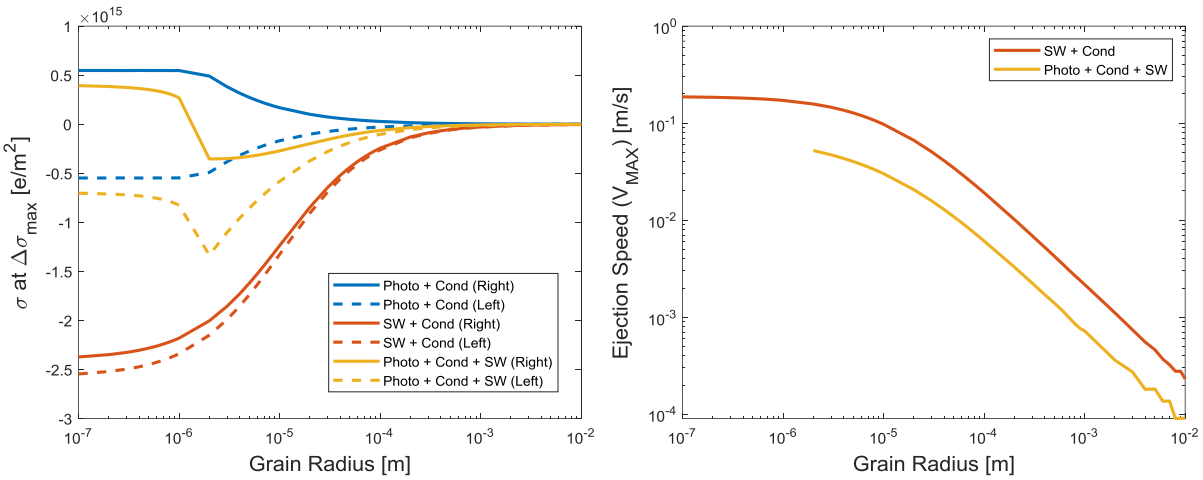

Figure 4.24: (Left) The associated grain charge densities when the electric field strength is maximum for three different models. The photoemission only model is plotted in blue, the solar wind only model is plotted in red, and the photoemission with solar wind model is plotted in yellow. (Right) Ejection velocity V_{max} as a function of grain radius. Here a breakdown strength of 10^7 V/m is used as an upper bound on grain charging.

For the photoemission only model in the left plot, the charge density magnitudes are decreased as a result of the breakdown strength (compare with Figure 4.10), and so the resulting attractive electrostatic force would be weaker. For the photoemission with solar wind model, we see that at small grain radii, accounting for dielectric breakdown results in a positive charge on the right grain, which produces an attractive (not repulsive) electrostatic force with the negatively charged left grain. Thus, the dielectric breakdown level affects the ability of the photoemission with solar wind model to loft grains at small radii and places a lower limit on the loftable grain size in these charging conditions. Looking at the right plot of Figure 4.24, this means that the ejection speeds associated with these non-lofting grain conditions (at small grain radii) are not applicable, and thus are not plotted. Next, we examine how the electrostatic force is affected when dielectric breakdown is accounted for in Figure 4.25.

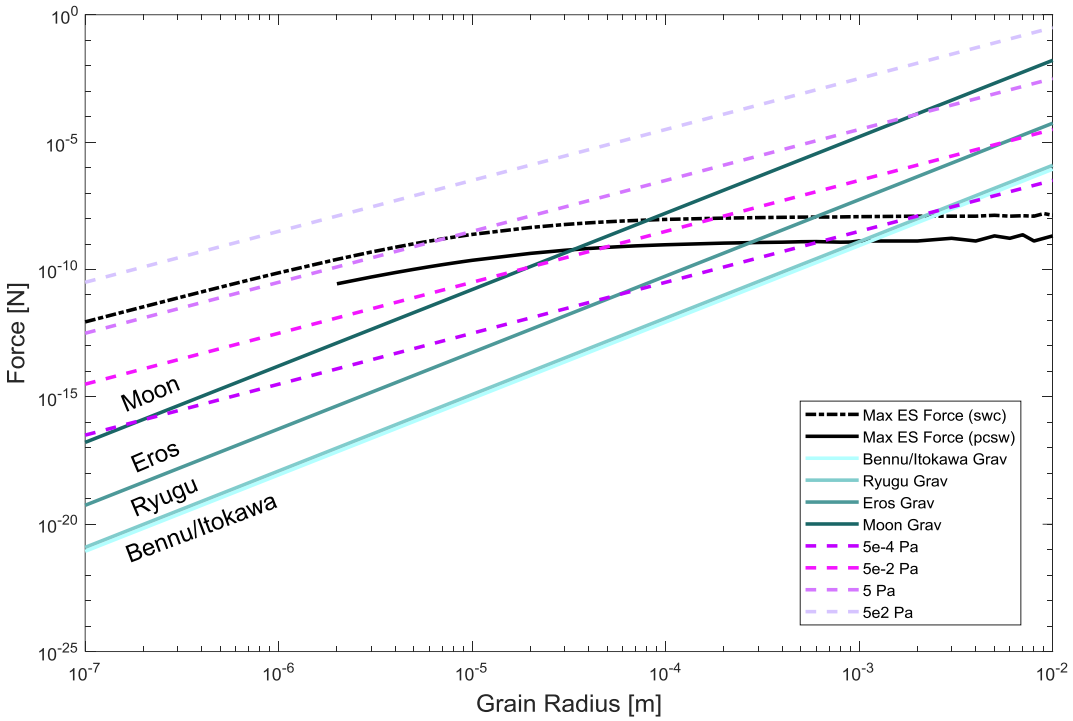

Figure 4.25: Electrostatic force over a range of grain sizes for two different charging models—solar wind only in a dash-dotted black line and combined photoemission with solar wind in a solid black line. A range of gravitational forces is plotted in various shades of solid teal, while a range of cohesive forces is plotted in various shades of dashed purple. Here a breakdown strength of 10^7 V/m is used as an upper bound on grain charging.

Here we see that the smaller grains affected by the dielectric breakdown will experience smaller electrostatic forces. As discussed in the previous plots, this means that the cohesive strengths that these grains can overcome will decrease.

Next looking at a breakdown strength of 10^6 V/m, Figure 4.26 gives the maximum electric field strengths for the three models.

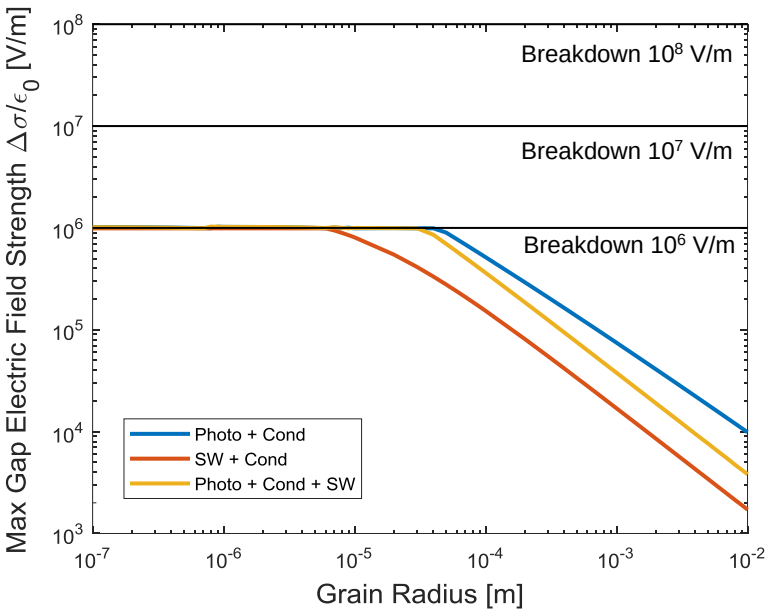

Figure 4.26: Maximum electric field strength as a function of grain radius for three different supercharging models—photoemission only is shown in blue, solar wind only in red, and photoemission with solar wind in yellow. Here a breakdown strength of 10^6 V/m is used as an upper bound on grain charging.

Here we see that all three models are affected by the dielectric breakdown for grain sizes up to several microns in radius for the solar wind model and up to several tens of microns in radius for the other two models. Next, we examine the charge densities of the grains and the ejection speeds in Figure 4.27.

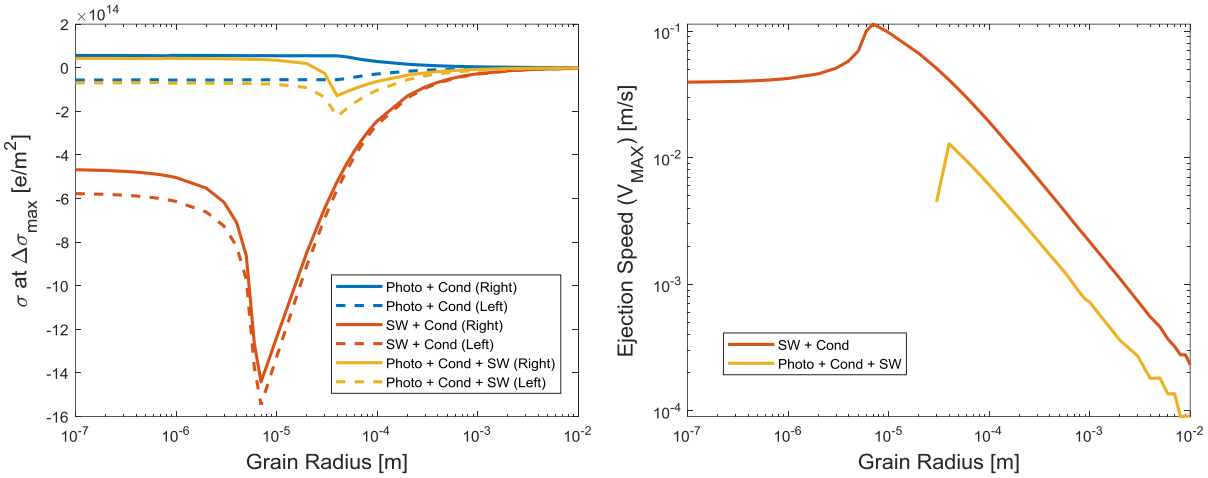

Figure 4.27: (Left) The associated grain charge densities when the electric field strength is maximum for three different models. The photoemission only model is plotted in blue, the solar wind only model is plotted in red, and the photoemission with solar wind model is plotted in yellow. (Right) Ejection velocity V_{max} as a function of grain radius. Here a breakdown strength of 10^6 V/m is used as an upper bound on grain charging.

For the photoemission only model, we see that the charge density magnitude is decreased for a wider range of grain sizes. While this model always results in oppositely charged grains and thus an attractive electric field (no grain lofting), the overall field magnitude is decreased as a result of the breakdown strength. For the combined photoemission with solar wind model, we again see that dielectric breakdown results in a population of smaller grains that aren't loftable. Up to around 30 microns, the grains are oppositely charged and so experience an attractive electrostatic force. For the solar wind only model, the grains are negatively charged and always experience a repulsive electrostatic force. However, dielectric breakdown lowers the magnitude of charge on the grains, which results in a lower overall electrostatic force. From Figure 4.28 below, we see that this affects the cohesive strength a grain can overcome.

Looking at the right plot of Figure 4.27, we see that there exists a range of grain sizes larger than those that aren't loftable and smaller than those unaffected by the breakdown strength (less than 7 microns for the solar wind only model and between 30-40 microns for the photoemission with solar wind model) whose ejection speed is affected by

the breakdown strength. For these grains, their ejection speed decreases due to dielectric breakdown, and thus these grains may not be able to overcome the same cohesive strengths as if dielectric breakdown is neglected. Figure 4.30 also illustrates this point.

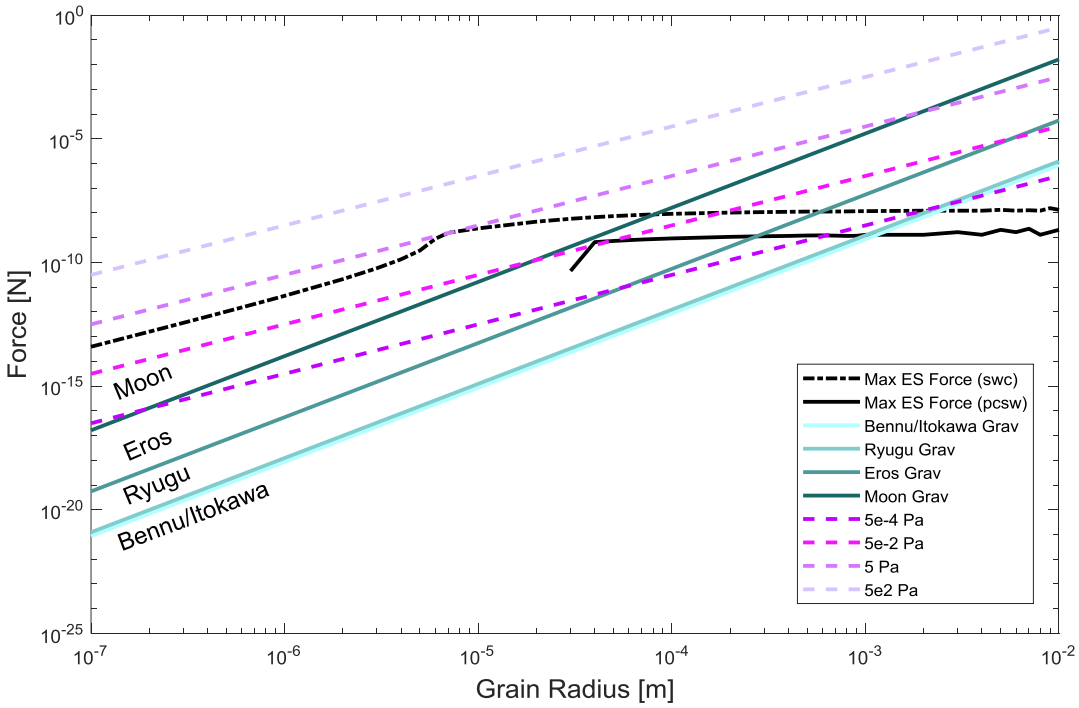

Figure 4.28: Electrostatic force over a range of grain sizes for two different charging models—solar wind only in a dash-dotted black line and combined photoemission with solar wind in a solid black line. A range of gravitational forces is plotted in various shades of solid teal, while a range of cohesive forces is plotted in various shades of dashed purple. Here a breakdown strength of 10^7 V/m is used as an upper bound on grain charging.

Overall dielectric breakdown acts to place a lower limit on the grain size that is loftable using the photoemission with solar wind model. For all three models, dielectric breakdown acts to limit grain charge and results in weaker electrostatic forces, which limits the cohesive strengths that grains can overcome.

4.5 Summary

In this chapter we examined new grain-scale supercharging models and used them to bound the initial conditions required for dust grain lofting. Specifically, we solve for

maximum gap electric field conditions over a range of grain sizes to bound local surface conditions required for lofting. We are not only able to solve for the associated grain charge, but also the associated maximum cohesive strength a grain can overcome. Furthermore, we use this information at the maximum gap electric field condition to compute the initial speed with which lofted grains are ejected from the surface. Given the escape speed and rotation rate of an asteroid, this information can be used to predict which grain populations are the most mobile and which may have been stripped away completely from the surface over the natural evolution of the body. By separating the initial velocity computation into two separate parts, we can generalize our results to a wider range of bodies due to the independence of one parameter to gravity. Overall, we have developed a simpler method of generating initial conditions for lofted grains while using supercharging models to account for grain-scale electric field generation.

Additionally, through examination of different variables affecting grain-scale charging—such as grain size, charge separation, regolith cohesion and primary body size—we can better understand and quantify how dust grains of different sizes and in different environments will be affected. Namely we find that grains with smaller charge separations (perhaps more compactly situated on the surface) will reach higher maximum charge densities, but lower overall grain charges. As a result, these grains will be more limited in the surface conditions they are able to loft from. We also examined the effect that the dielectric breakdown strength plays in grain charging. In particular, dielectric breakdown appears to place a lower limit on the size of grains that can be electrostatically lofted by limiting charge build-up.

Overall the analysis conducted in this chapter provides a more complete understanding of the new grain-scale supercharging models, the different parameters affecting grain charging, and how these models can be used to bound electrostatic lofting requirements for dust grains on small bodies in the Solar System.

Chapter 5

Dust Particle Behavior

In this section, we describe dust particle behavior simulated in the small body environment model using four main studies. The simulation parameters including the primary body and grain initial conditions are given at the beginning of each section. For all simulations, the small body environment model developed in Chapter 3 and the models pertaining to grain lofting initial conditions discussed in Chapter 4 are used, unless otherwise noted. In general, dust particle behavior is sensitive to a variety of initial conditions including grain charge, grain size, regolith cohesion, initial velocity from the surface, local gravity and spin rate, and the electric field strength and characteristics of the plasma sheath.

A quick note on the definitions used to describe different types of dust motion discussed in this chapter. *Launched* particles refer to dust grains given an initial upward velocity from the surface. These grains represent particles which have already separated from the surface and therefore do not take into account the cohesive properties of the regolith. *Lofted* particles refer to dust grains with no initial velocity. These grains must acquire sufficient charge to overcome the surface forces holding them to the regolith (can include gravity and cohesion). *Levitated* particles refer to dust grains which experience an oscillatory motion above the surface of the small body. Note that levitation occurs after particles have separated from the surface and describes a special type of motion that separated particles can exhibit; whereas launching and lofting refer more to the type of separation particles undergo from the surface. Only launched and lofted particle motions are examined in this thesis.

5.1 Complex 1992SK Launched Particle Simulation

In the first simulation, particles of various sizes were given an initial upward velocity from the surface of asteroid 1992SK and their subsequent motion recorded. Particle sizes were varied between 5 microns and 35 microns. Lee [29] notes that particles on asteroids will typically not exceed 50 to 150 microns, and so this range of sizes is applicable to that found in nature. A material density of 3.5 g/cm^3 was chosen such that it was denser than the bulk density of the asteroid (2.3 g/cm^3) [5]. Particle location across the surface was varied (see Figure 5.1), but the initial grain charge was kept the same for all particles tested. A value of 2.5×10^{-15} C was chosen based on experimental results found by Wang et al. [51]. The initial velocity was varied between 0.03 and 0.5 m/s, which represents a force imparted to the particle from exploration activities such as landing, anchoring, sampling, or otherwise disturbing the surface environment. However, this velocity also corresponds to experimental dust lofting observed experimentally by Wang et al. [51].

Table 5.1 summaries the values used in simulation for the small body, the dust particle, and the plasma sheath environment. Any plasma characteristics used were based on simulation parameters by Colwell et al. [7]. Initial condition parameters for the simulation include dust particle charge, velocity magnitude (normal to the local surface), and location on the asteroid, which inherently includes variation in gravity and electric field. Note that dust particles are launched with a nonzero initial velocity in this study, and that the methods developed in Chapter 4 to generate grain initial conditions were not used here. Instead, experimental result values from Wang et al. [51] were used.

Table 5.1: Simulation parameters for the small body, dust particle, and plasma sheath.

Parameter	Symbol	Value
Small Body Properties (Asteroid 1992SK)		
Size (approx.)	$r_{ast,x}$	715 m
	$r_{ast,y}$	460 m
	$r_{ast,z}$	470 m
Bulk Density	ρ	2.3 g/cm^3
Gravitational Parameter	μ	81.5462 m^3/s^2
Spin Period (about z-axis)	$T = \frac{2\pi}{\omega}$	7.3182 hours
Distance from Sun (circular orbit)	d	1 AU
Solar Pressure at 1AU	p_{SRP}	4.57×10^{-6} N/m^2
Dust Particle Properties		
Size (spherical)	r_d	5µm, 10µm, 35µm
Material Density	ρ_d	3.5 g/cm^3
Initial Charge	Q_{d0}	2.5×10^{-15} C
Reflectivity	C_R	1
Plasma Sheath Properties		
Average Photoelectron Temperature	$k_B T_{pe}$	2.2 eV
Photocurrent	I_{ph0}	$2.8 \times 10^9/d^2$ electrons/cm^{2}s
Average Solar Wind Electron Temperature	$k_B T_{sw}$	10 eV
Solar Wind Electron Density	n_{sw}	$5/d^2$ electrons/cm^3

Seventeen different initial locations on the surface were chosen for analysis, providing sufficient sampling of the conditions felt across the sunlit surface. Only particle

locations with surface electric field strengths greater than 0 were chosen, and so there is a bias that the points examined lie in only one hemisphere of the asteroid, as dictated by the sunlit portion of the asteroid. The seventeen position locations are denoted on top of the electric field map in Figure 5.1 below.

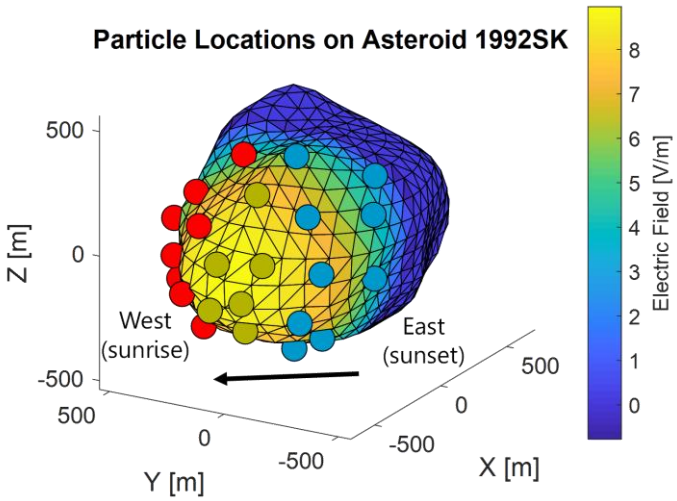

5.1: Launched particle locations on the surface of asteroid 1992SK. Locations are colored red, yellow, and blue corresponding to their relative longitudes—west, central, east respectively.

For analysis, I divided the points into 3 different longitudinal regions to quantify what role location played into the results—western (red), central (yellow), and eastern (blue).

5.1.1 Results for 5-, 10-, and 35-Micron Grains

For a particle size of 5 microns, Figure 5.2 gives the maximum altitude achieved over the course of a trajectory given a range of initial vertical velocities. Any particles that escaped the surface and did not reimpact are plotted at 600 meters altitude for visualization.

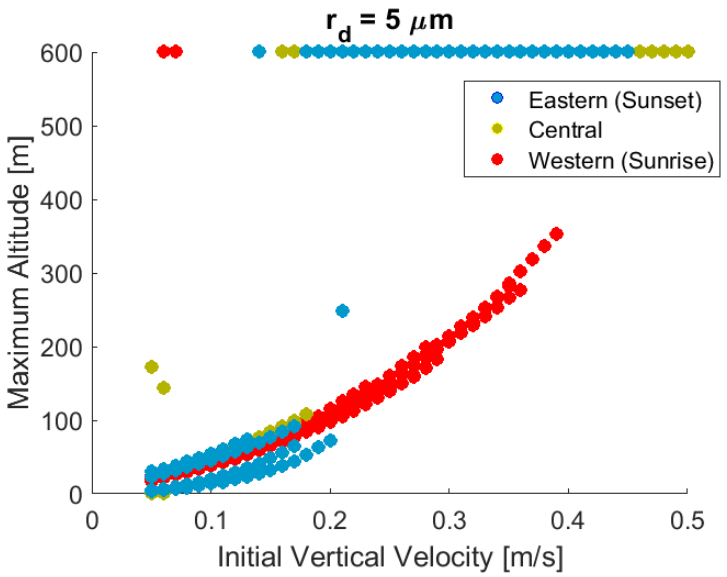

Figure 5.2: Maximum altitude reached by a 5 micron dust particle given a range of initial vertical velocities. Points represent a range of initial locations over the sunlit surface. Western particles are shown in red, central particles in yellow, and eastern particles in blue.

As illustrated, 5 micron particles appear to be highly sensitive to initial conditions on 1992SK, with particle escape beginning near 0.05 m/s and occurring over the entire gamut of velocities tested. While in general, initial velocities higher than those already proven to cause a particle to escape the surface would also cause the same particle to escape, this is not necessarily the case for these smaller particles. For instance, one particle case tested escaped at launch velocities of 0.075 m/s and 0.2 m/s but returned to the surface for launch velocities of 0.65 m/s and 0.1 m/s. This leads us to believe that these smaller, less massive particles are highly sensitive to the initial conditions, and in particular, are more heavily affected by the electrostatic forces acting near the surface.

Dividing the data up by latitude and longitude, we find that the strongest correlation is due to longitudinal variations. This observed longitudinal correlation is likely due to the fact that solar radiation pressure adds to the direction of motion for eastern particles and subtracts from the direction of motion for western particles, as described by the illustration below.

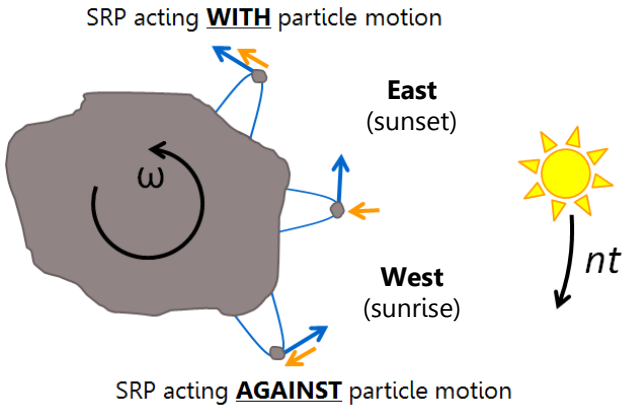

Figure 5.3: Effect of solar radiation pressure on particle trajectories at different longitudinal locations.

For a particle size of 10 microns, Figure 5.4 shows the maximum altitude reached given a range of initial vertical velocities. Particles that escaped the surface are again plotted at 600 meters altitude for visualization.

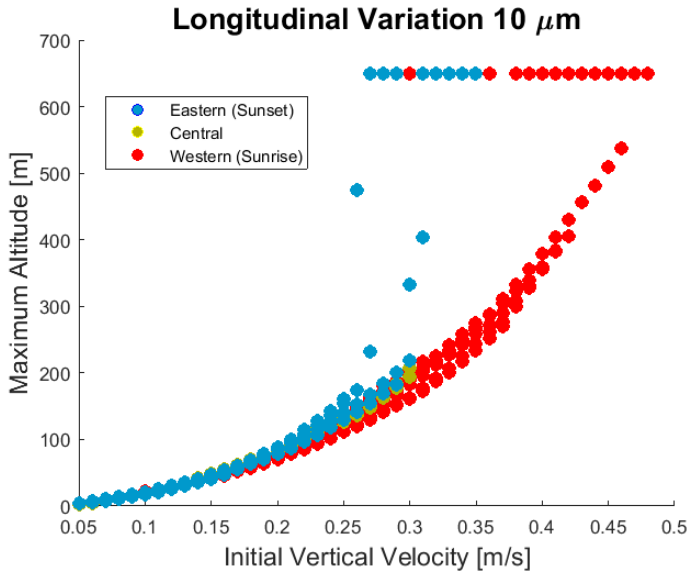

Figure 5.4: Maximum altitude reached by a 10 micron dust particle given a range of initial vertical velocities. Points represent a range of initial locations over the sunlit surface. Western particles are shown in red, central particles in yellow, and eastern particles in blue.

Compared with the results in Figure 5.2 for 5 micron particles, 10 micron particles appear to be less sensitive to initial conditions, with most particles following the same ballistic trajectory up to 0.2 m/s. This is likely a result of larger, more massive particles

being more heavily perturbed by the forces of gravity. This implies that the electrostatic force has a harder time influencing particles to escape once a certain size (and mass) of particle is reached.

For the given velocities simulated, 10 micron particles disturbed from the surface with velocities less than 0.3 m/s will return to the surface. Those with greater velocities are likely to escape, depending on their initial location on the surface. Here we see that eastern-located particles are likely to escape at lower initial velocities than western-located particles. This is likely due to the influence and direction of solar radiation pressure acting on the particle's trajectory.

The range of maximum altitudes reached for 35-micron particles are plotted in Figure 5.5 below, with particle locations denoted by color. Any particles that escaped the surface are plotted at 1200 meters altitude for visualization.

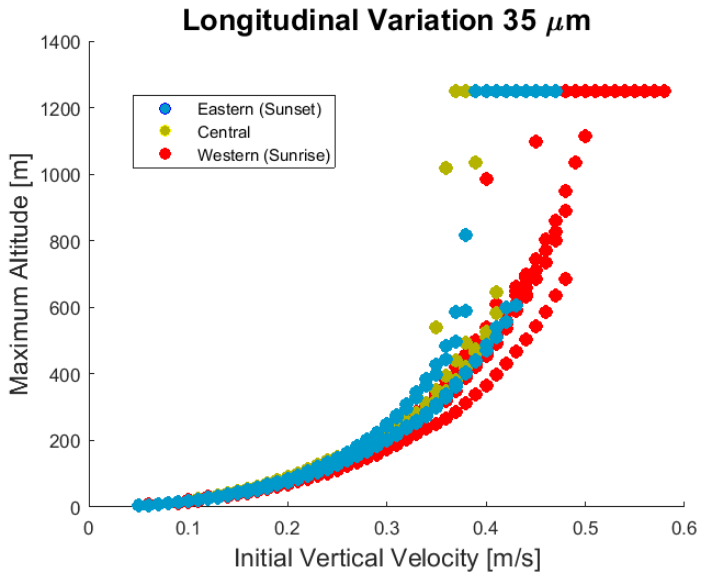

Figure 5.5: Maximum altitude reached by a 35 micron dust particle given a range of initial vertical velocities. Points represent a range of initial locations over the sunlit surface. Western particles are shown in red, central particles in yellow, and eastern particles in blue.

These particles exhibit more uniform behavior at lower initial velocities, and only show differences in motion at greater initial speeds. The 35 micron particles are also able to

travel to much greater maximum altitudes before returning to the surface than was observed for either 5 micron or 10 micron particles. This is because the larger particles feel the attractive force of gravity more greatly than the smaller particles and are less perturbed by local electrostatic forces.

Again, the launching location of these particles affects how high in altitude the particle can reach and for what initial speed it escapes the surface. Eastern particles are likely to escape at lower initial surface velocities than western particles due to solar radiation pressure perturbations.

5.1.2 Particle Size Dependence

Particle size is an exceedingly important factor in dust particle dynamics. Maximum altitude data for 5-micron, 10-micron, and 35-micron grains are plotted together in Figure 5.6 below for comparison.

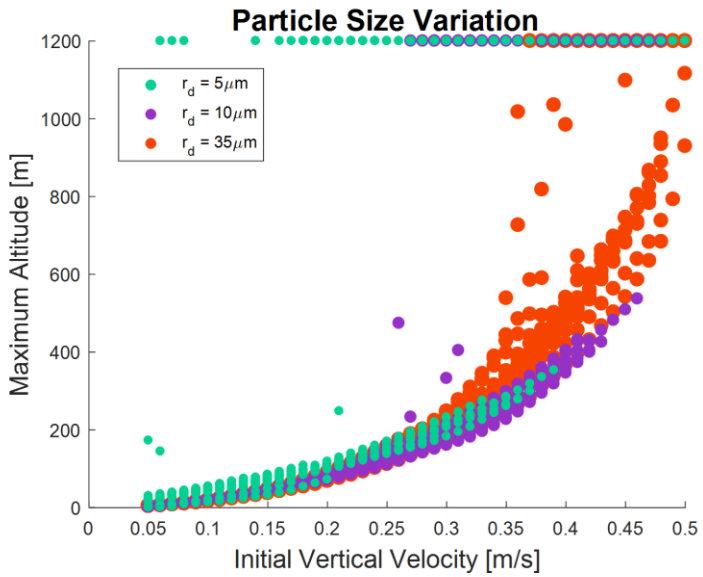

Figure 5.6: Maximum altitude reached for 5 micron (teal), 10 micron (purple), and 35 micron (orange) particles over a range of initial velocities.

Here we see that larger particles can sustain greater initial velocities, reaching greater maximum heights while still returning to the small body surface. Conversely,

smaller particles require much less initial velocity to completely escape from the surface of the asteroid, and in fact, are highly sensitive to the initial conditions.

In general, smaller, less massive particles are highly influenced by electrostatics and are more likely to be lost at very small disturbing velocities. Assuming these types of conditions are present on asteroids naturally (without exploration activities), we would not expect to find smaller particles to remain on the surface for long periods of time. Likely these particles would have been disturbed naturally and would have succumbed to the additive perturbations of solar radiation pressure such that escape from the asteroid was inevitable. These results are supported by the conditions observed experimentally by Wang et al. [51]. It should be noted that this type of analysis only simulates particles on the surface. Smaller-sized particles may still exist under the top layer of surface soil and be available for disturbance by exploration activities. However, once these particles are dislodged from the surface, they will likely escape and not come back down to interfere with exploration activities in the near-surface region.

Additionally, larger, more massive particles are more heavily influenced by gravitational accelerations and are likely to return to the surface once disturbed. Contrary to the motion of smaller particles, these larger particles persist in the asteroid environment for longer periods of time, reaching higher maximum altitudes, and requiring larger initial velocities for escape from the surface to occur. Thus, this larger particle population may create a dusty, charged working environment for exploration activities and has the potential to deposit returning dust particles on instrumentation.

5.1.3 Longitudinal Dependence

Next, we examine longitudinal variation for all particle sizes and how it affects dust particle behavior. The maximum altitude as a function of initial velocity is given in Figure 5.7, while particle trajectories in the body frame are shown in Figure 5.8.

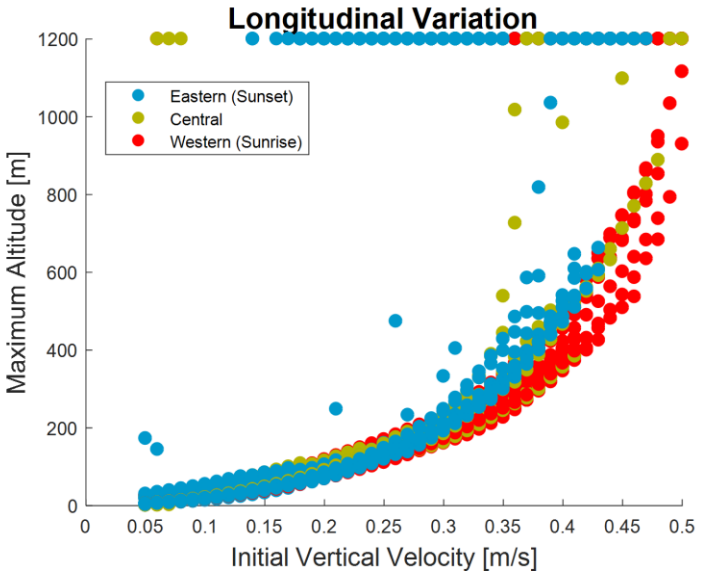

Figure 5.7: Maximum altitude reached for all particle sizes over a range of initial velocities, separated by color based on initial longitude. Western particles are shown in red, central particles in yellow, and eastern particles in blue.

Overall, we find that the areas with the greatest amount of levitating dust particles are those at the western (sunrise) side of the asteroid. This is where particles can reach higher maximum altitudes while still returning to the surface. Thus, cleaner areas near the eastern (sunset) side of the asteroid may be better for exploration operations which have the potential to stir up surface dust. In this sunset region, particles escape more quickly and more frequently and don't often return to the surface to cause a dusty environment. However, we also gathered data on particle trajectories and landing sites, which gives more insight into particle behavior than a single value of maximum altitude.

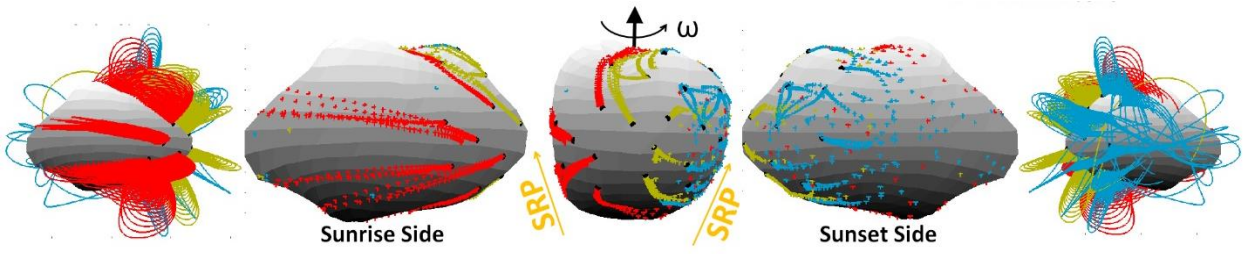

Figure 5.8: Trajectories of dust particle shown in the body frame. Particles in red originate on the western side, while particles in blue originate on the eastern side. Centrally located particles are shown in yellow.

From the trajectory data provided in Figure 5.8, it is evident that the trajectories of particles on the sunset side are more chaotic in nature than those on the sunrise side. While it was expected that solar radiation pressure would clear out particles on the sunset (blue) side more easily due to both solar radiation pressure and asteroid rotation acting in the same direction, it was not obvious that the trajectories of particles would become more chaotic and tangled. Recall that solar radiation pressure acts to increase the eccentricity of the particle's orbit, changing its shape and lowering its periapsis. Thus, particles will tend to re-impact closer to the initial launching site. However, when this effect is combined with the rotational dynamics of the small body (via particle launching conditions), the results are more complicated to explain.

On the sunrise (red) side, solar radiation pressure is acting against rotation of the asteroid and thus acts to slow the particle down. In this time, the body is rotating underneath the particle and the particle is able to reach greater reimpact distances because of a slowed trajectory combined with the direction of the body's rotation. On the sunset (blue) side, solar radiation pressure acts with the rotation of the asteroid and particle motion is accelerated, leading to more particle escapes. For the particles that are not able to escape, their reimpact site is closer to the initial launching site because of the lowered periapsis.

While it was originally believed that sunset would be the cleanest area for exploration activities to occur due to the higher likelihood of particle escapes, this may not be as obvious an answer as we thought since particle trajectories in this area are much less predictable. As I will discuss more in later studies, particles on the sunset side may have more time to charge throughout the day, meaning they are able to acquire sufficient charge to overcome gravity and cohesion to become lofted. As a result, this would create a messy environment to work in on the sunset side. In contrast, particles on the sunrise side may not have sufficient time to charge and so this area may be cleaner to work in.

5.1.4 Summary

In this study we have launched grains of various sizes from the rotating and electrically-charged surface environment of asteroid 1992SK. Launching velocities were chosen based on measurements taken experimentally by Wang et al. [51]. Cohesion is not considered in this study.

From the results we find that 1) smaller particles more easily escape than larger particles, 2) larger particles reach greater altitudes but tend to return to the surface to create a dusty working environment, and 3) sunset is likely to be a cleaner working area than sunrise because launched particles are able to escape more quickly and more frequently there due to solar radiation pressure. However, from particle trajectory and landing site data we find that trajectories are much more chaotic and tangled on the sunset side, while those on the sunrise side tend to be more streamlined and reimpact in a swept-back line from the initial launching location. We also find that particles on the sunset side tend to have more binary behavior in that they either escape quickly or experience a chaotic path back to reimpact. This reimpact location also tends to be closer to the particle's initial launching location than is observed for particles on the sunrise side.

While this study is an important first step in understanding the complex interactions of the small body environment and its effect on electrostatically-driven dust behavior, the next studies will incorporate the effect of varying particle charge, charging rates, and perhaps most importantly the cohesive strength of regolith.

5.2 Complex 1992SK Lofted Particle Simulation

In the next study, the same particle sizes and initial locations were used (see Table 5.1), but this time the initial charge rather than the initial velocity was varied. With a constant initial velocity of 0 m/s, the charge was changed ($Q_{d0} = 10^{-15}$ to 10^{-9} C) until lofting of the dust particle naturally occurred. In this way, we were able to study natural

dust lofting requirements and subsequent behavior, in contrast to artificially launching particles in the previous study. While this simulation still did not account for cohesion of the regolith material, examining the required initial conditions for separation from the surface was the next logical step in developing a realistic dust lofting simulation. Again, asteroid 1992SK with a bulk density of 2.3 g/cm^3 and spin period of 7.3182 hours was used as the primary body [5]. Dust particles ranged in size from 5 to 35 microns with a density of 3.5 g/cm^3 and were lofted from seventeen different locations on the sunlit face of the body.

Figure 5.9 shows the resulting particle charges required to loft grains naturally from the surface when only accounting for gravitational forces. The data is separated by grain size to show charge dependence. Escaped grains are plotted at 1800 meters for visualization.

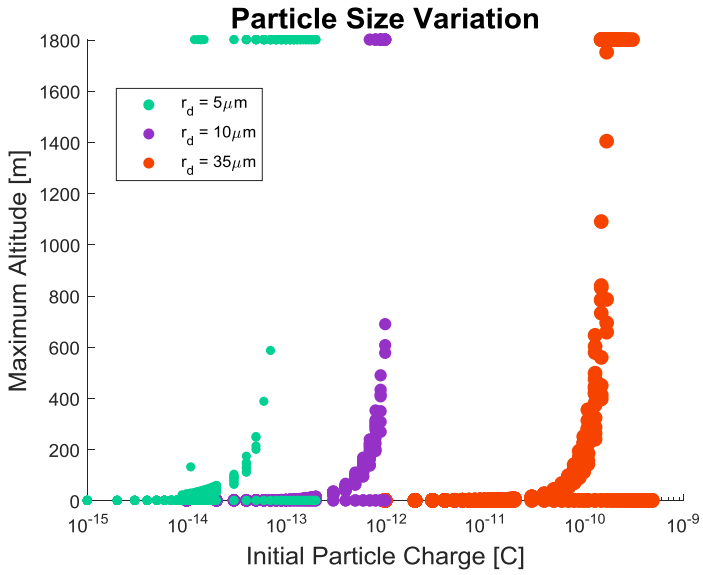

Figure 5.9: Initial particle charge required for electrostatic dust lofting (gravity only). 5 micron grains are shown in teal, 10 microns in purple, and 35 microns in orange.

From this plot, we see that there exists a range of initial particle charges that lead to naturally-lofted dust particles. These required particle charges are a function of particle size, which is unsurprising since gravitational attraction is related to the size of the particle through its mass (which goes as r_d^3). Thus, larger particles will require larger charges to

overcome their greater associated gravitational forces. However, the most striking result from Figure 5.9 is the magnitude of the required charge for lofting. The charges shown are orders of magnitude larger than even those found experimentally by Wang et al. [51], which are already orders of magnitude larger than those predicted using classical charge models. It's also important to note that these results do not even consider the additional (stronger) downward force of regolith cohesion. This suggests that if dust grains are to loft naturally in nature, there must be some other grain-scale mechanism at work to allow the electrostatic force to overcome both gravity and cohesion. This realization led to investigation of the supercharging model [62] in later studies to determine more realistic initial conditions for electrostatic dust lofting.

Particle trajectories and reimpact locations for the current study are shown in Figure 5.10.

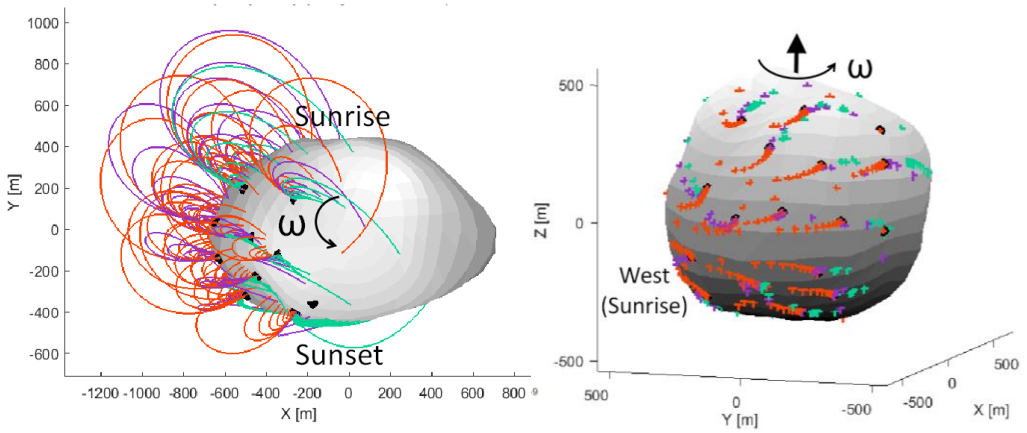

Figure 5.10: (Left) Dust particle trajectories shown in the body frame looking down the axis of rotation. (Right) Reimpact sites of non-escaping particles. 5 micron grains are shown in teal, 10 micron grains in purple, and 35 micron grains in orange.

Here we note that the reimpact locations look slightly different than those observed for the previous launching simulation (section 5.1). In particular, the dispersion of reimpact locations appears to be lower. This is because particles in the lofting simulation do not have their initial upward velocities supplemented by a launching speed. This type of behavior

may be more typical of lofted dust behavior found in nature. However, the addition of other forces such as cohesion and the grain-to-grain supercharging interaction still need to be considered to make this determination. The next study includes these considerations.

5.3 Spherical Asteroids of Varying Size and Spin Period (Ryugu-like, Bennu-like)

In this next study, we run a series of simulations which use initial conditions governed by grain-scale supercharging on the surface of spherical asteroids. Specifically, we investigate the effect of grain size, primary body spin rate, and primary body size on electrostatically-lofted dust particle behavior.

The primary bodies discussed in this study are represented using a spherical faceted shape model. A faceted model is implemented now so that future iterations of the simulation can be run using complex shape models for the asteroids under consideration. Note that the faceted nature of the model results in a small meter-level variation in the surface radius and will affect how altitude is determined. In the simulation, the dust grain's altitude over time is computed using the distance from the particle's location to the facet directly underneath it (as discussed in 3.3.3). When this altitude is plotted over time, it results in a bumpy altitude trajectory but is simply a product of the faceted model being used. The model is made up of 1016 vertices and 2028 facets, which gives an average facet area of 39 m^2. This facet area, however, will vary from facet to facet across the surface. While we use a faceted model that has the ability to take the form of a complex body, it is beneficial to start with a spherical shape model to understand how the basic structure, size and rotation of a body affects dust behavior without consideration to the unique shape of any one specific body. In this way we can extend these fundamental results to a variety of small bodies instead of just the bodies being examined.

The simulations begin at dust grain separation from the surface using initial conditions determined from the grain-scale supercharging model discussed in Section 4.4

above. The electrostatic force is directed along the surface outward normal from the facet directly underneath the particle. Subsequent dust grain behavior is observed and analyzed. Note that the grain's electrostatics are only affected by grain-scale supercharging leading up to lofting in generating grain initial conditions. Grains returning to the surface after lofting cannot build up sufficient grain-to-grain charge instantaneously to have an effect on their re-impact motion.

Supercharged grains reach their maximum gap electric field quickly—within minutes rather than hours—suggesting that grain charging is not limited by the rotation rate of the primary body. Instead, grains charge quickly (within 10^2 seconds) and can theoretically reach lofting requirements at several points throughout the local day, depending, of course, on local surface illumination conditions. In our simulation here, we loft dust grains from every illuminated facet on the sun-facing side of the primary body. Because the body is spherical, this enables us to simulate lofting from various latitudes throughout the local day and to track how the lofted time of day affects subsequent grain behavior at each latitude. Note that we only simulate a single lofting event for each grain—once a grain is lofted, it either reimpacts or escapes and the simulation stops. In theory, grains could be relofted once they've reimpacted the surface and/or hop across the surface multiple times; however, this is not modeled in the study and is instead left for future work.

Three dust grain sizes are studied—1 micron, 5 microns, and 10 microns. None of the 10-micron grains were seen to escape the body in the baseline case (a 500-meter spherical Ryugu-like asteroid), and so this was used as an upper bound of particle sizes in this study. A density of 1.2 g/cm^3 for the primary body composition and a dust grain density of 2.4 g/cm^3 were chosen based on findings in Lauretta et al. [28] and Watanabe et al. [52]. All bodies are simulated at a distance of 1 AU from the Sun. Two different rotation periods for the primary body were used—3.1 hours and 7.627 hours—as well as two different radii—500 meters (Ryugu-like) and 250 meters (Bennu-like). Specifically, we compare a

baseline case (500-meter body, 7.627-hour period) to a faster rotating case (500-meter body, 3.1-hour period) and to a smaller body size case (250-meter body, 7.627-hour period). In this way, we can isolate the factors of rotation speed and primary body size to discuss how each affects grain lofting and dynamics on different bodies in a more generalized way. These results can thus be applied to other cases. In this study, an effective gravity force is used in generating initial conditions to account for rotation of the small body. Table 5.2 provides relevant parameters, such as surface gravity and surface escape speed, for each of the bodies under consideration in this study.

Table 5.2: Relevant parameters for the small bodies of interest.

Case	Radius	Rotation Period	Mass	Surface Gravity	Surface Escape Speed
Baseline	500 m	7.627 hrs	6.2×10^{11} kg	1.7×10^{-4} m/s^2	41 cm/s
Faster Rotation	500 m	3.1 hrs	6.2×10^{11} kg	1.7×10^{-4} m/s^2	41 cm/s
Smaller Body	250 m	7.627 hrs	7.8×10^{10} kg	8.4×10^{-5} m/s^2	20 cm/s

For the given small body density, a maximum spin rate of 3.01 hours is required such that the centripetal acceleration is smaller in magnitude than the surface gravity (see equation 3.7). Here we chose to use a conservative value of 3.1 hours as the fastest rotation period. The 7.627-hour period models that of Ryugu's rotational period [52]. Note that Bennu's rotational period is 4.288 hours [28]. We don't discuss the data from this exact rotational period in this paper, simply because the results can be inferred from combining the conclusions of the faster rotating (500 m, 3.1 hr) and smaller body size (250 m, 7.627 hr) results discussed in the sections below. The initial conditions used for each dust grain are given in Table 5.3 using the methods discussed in Section 4.4 above.

Table 5.3: Dust grain initial conditions computed using the grain-scale supercharging model.

Grain Radius	Initial Charge	Ejection Speed	Cohesion
1 μm	-2.89e-18 C	5.9 cm/s	1.39 Pa
5 μm	-3.42e-17 C	4.0 cm/s	0.65 Pa
10 μm	-9.33e-17 C	3.0 cm/s	0.36 Pa

5.3.1 Escaped Grains

First, we look at the percentage of lofted grains that escaped the body. This statistic gives insight into the mobility of the different populations of dust grains and makes predictions about which populations may have been preferentially eliminated from the surface of these bodies over time. Table 5.4 gives particle escape statistics for each of the three small body cases and Figure 5.11 shows the initial locations of escaped grains. Both are organized by grain size.

Table 5.4: Escaped particle statistics by small body case and particle size.

Case	Total Locations	1 micron	5 microns	10 microns
Baseline	423	93 (22%)	141 (33%)	0 (0%)
Faster Rotation	423	94 (22%)	147 (35%)	63 (15%)
Smaller Body	423	94 (22%)	145 (34%)	158 (37%)

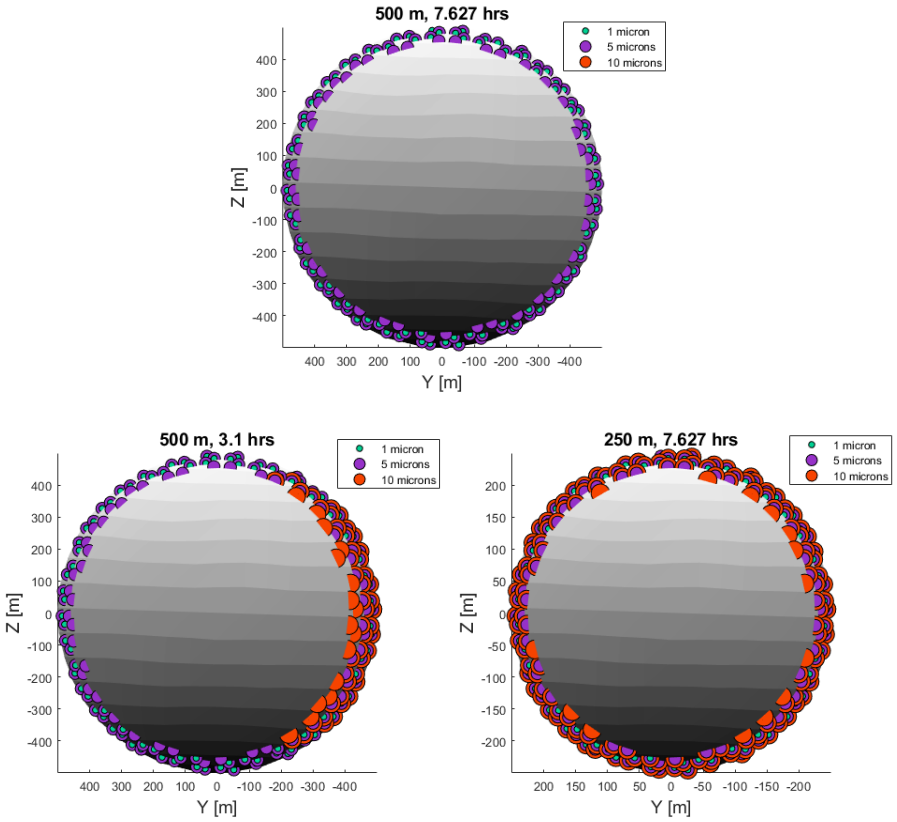

Figure 5.11: Initial locations of escaped grains on a) a 500-meter spherical asteroid with 7.627-hour rotation period, b) a 500-meter spherical asteroid with 3.1-hour rotation period, and a c) 250-meter spherical asteroid with a 7.627-hour rotation period. 1 micron grains are shown in teal, 5 micron grains in purple, and 10 micron grains in orange.

Looking at the baseline case (top plot of Figure 5.11), we see that grains near the terminator regions with lower solar elevation angles appear to escape, while those in the interior of the body reimpact the surface after lofting. This suggests that solar radiation pressure plays a major role in eliminating these grains from the surface of small bodies. Once grains are lofted at these lower solar elevation angles, solar radiation pressure can carry them farther from the body. Note that only 1 micron and 5 micron dust grains are escaping. None of the larger 10 micron grains were seen to escape.

Examining the faster rotating case (bottom left plot of Figure 5.11), we see that faster rotation has the effect of eliminating more grains from the surface due to the

increased rotational boost. This is illustrated most strikingly on the sunset side of the body where the larger 10-micron grains are able to escape.

For the smaller primary body case (bottom right plot of Figure 5.11), we see that decreasing the body's size has the effect of eliminating even more grains from the surface due to decreasing the body's mass. Grains on the surface of a smaller, less massive body will experience a smaller downward gravitational acceleration than those on the surface of a larger, more massive body. This is particularly evident for the larger 10-micron grains which experience greater escape rates overall in the smaller body case (when compared to the baseline case) and are able to escape from both the sunrise and sunset terminator regions of the body.

It's interesting overall to note that 5 micron grains appear to escape slightly more often than 1 micron grains (see Table 5.4). This is due to the varying electrostatic force over time, as is evident when examining the time rate of change of the charge for each case. Figure 5.12 below gives the acceleration magnitudes, acceleration slopes, and grain charges over time for two different sized particles lofted from the same location. This case, in particular, is one in which the 1-micron grain reimpacts the surface, while the 5-micron grain escapes the body completely.

The acceleration slope for each of the relevant forces—gravity, solar radiation pressure, and electrostatics—are calculated by taking the dot product of the acceleration vector with the surface normal vector of the facet directly under the dust grain.

$$\text{Acceleration Slope} \equiv \operatorname{acos}\left(\frac{\boldsymbol{a}}{|\boldsymbol{a}|} \cdot \hat{\boldsymbol{n}}\right)$$

An acceleration slope of 0 degrees corresponds to a force acting radially outward from the surface of the small body, while an acceleration slope of 180 degrees corresponds to a force acting radially inward towards the surface of the small body. Gravity, for instance, will always be pointing radially into the surface and will have a 180 degree acceleration slope

throughout the grain's trajectory. In contrast, the acceleration slope of solar radiation pressure will vary depending on the grain's location. For dayside trajectories, the acceleration slope of solar radiation pressure will vary between 90 degrees (sunrise and sunset at equator) and 180 degrees (local noon at equator). In general (and not accounting for grains with large altitudes off the surface), acceleration slopes between 0 and 90 degrees will tend to carry lofted grains farther from the surface, while those between 90 and 180 will tend to pull the grains back down.

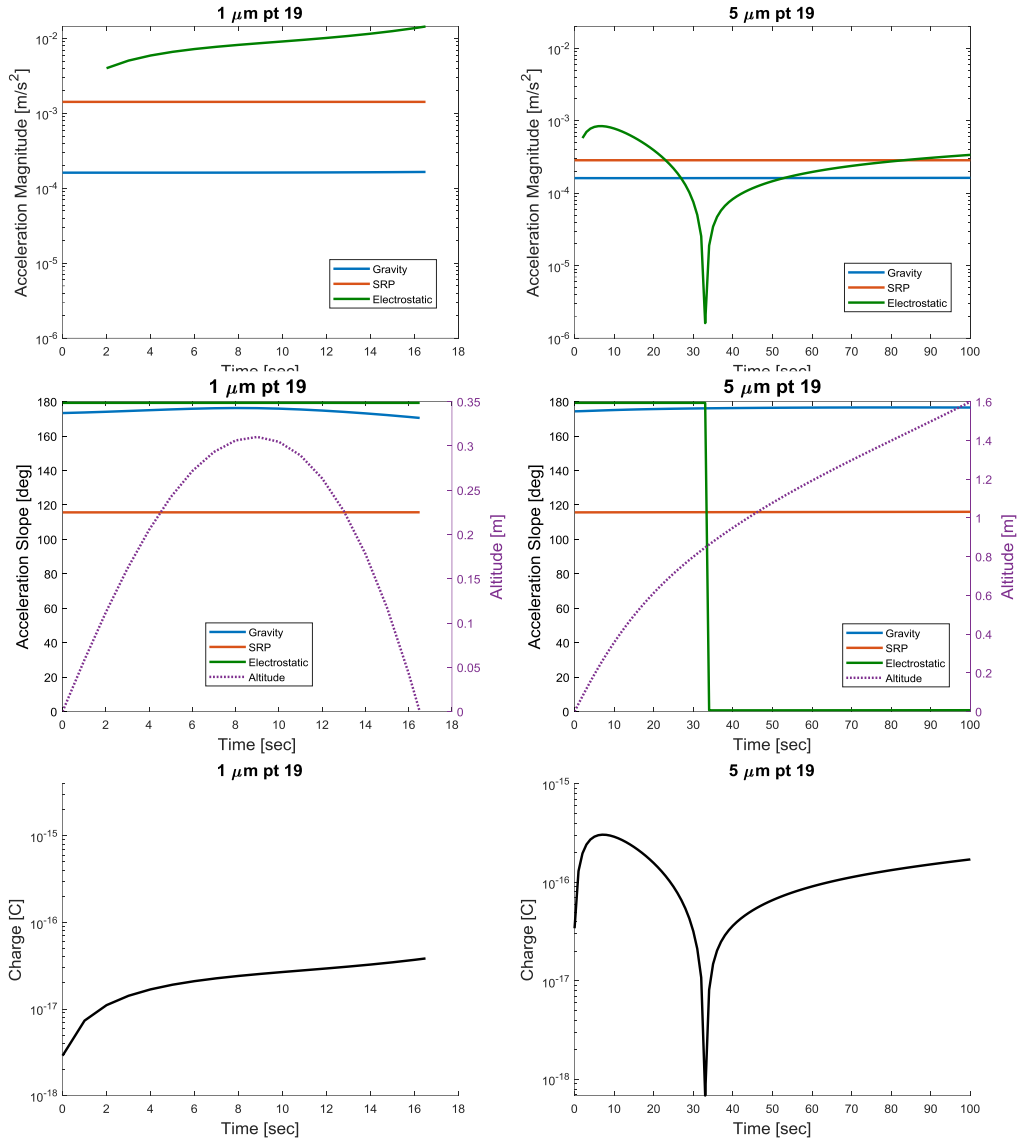

Figure 5.12: (top) Acceleration magnitudes, (center) acceleration slopes, and (bottom) charges over time for two lofted dust grains from the same location. Data for the 1-micron grain is on the left, while data for the 5-micron grain is on the right. Values for gravity are shown in blue, solar radiation pressure in red, and electrostatics in green. Grain altitude is given in purple and grain charge in black. Note that the grain charge shown is the absolute value of the charge.

Examining first the significance of solar radiation pressure, we note the difference in magnitudes of the accelerations due to solar radiation pressure between the 1-micron and 5-micron grains—1.42×10^{-3} m/s^2 and 2.85×10^{-4} m/s^2, respectively. Solar radiation pressure is nearly an order of magnitude larger for the 1-micron grain, and so it will be more difficult for the smaller grains to overcome the solar radiation pressure pushing them

back toward the surface. Thus, solar radiation pressure plays a more significant role in preventing these smaller grains from reaching higher altitudes where escape is possible. The influence of gravity is nearly the same for both grains with an acceleration magnitude of 1.63×10^{-4} m/s^2.

Examining next the role of electrostatic acceleration, we see that the 1-micron grain experiences a downward acceleration due to electrostatics throughout the entirety of its trajectory with a magnitude of 6.64×10^{-3} m/s^2. Its charge begins negative and continues to charge more negatively throughout its trajectory. In contrast, the 5-micron grain appears to undergo a sign change in its charge just after 30 seconds—from negative to positive—which flips the directionality of the electrostatic acceleration it experiences. As a result, the positively charged 5-micron grain begins to feel an upward acceleration from the plasma sheath, enabling it to travel higher above the surface where solar radiation pressure carries it farther and eventually pushes it to escape the body completely.

5.3.2 Reimpacting Grains

Next, we look at the grains which reimpacted the surface after lofting. Figure 5.13 gives the trajectories for each of the three cases, while Figure 5.14 shows the altitudes of lofted grains over time. Note again that the altitudes may appear bumpy due to the faceted nature of the asteroid shape model.

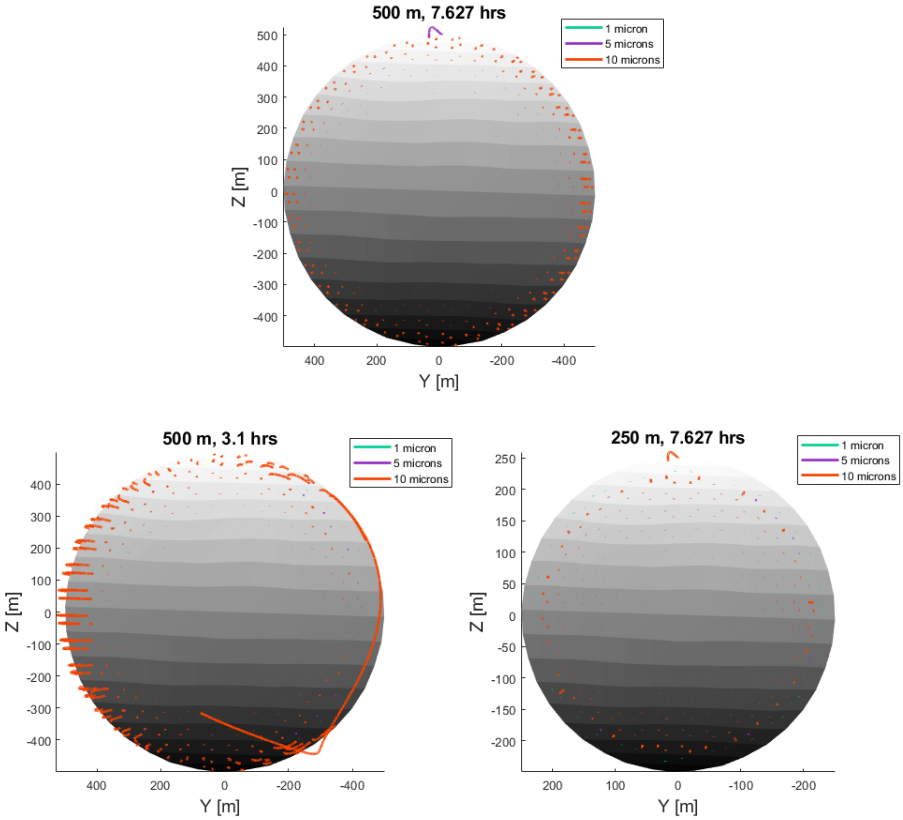

Figure 5.13: Trajectories of reimpacting dust grains on a) a 500-meter spherical asteroid with 7.627-hour rotation period, b) a 500-meter spherical asteroid with 3.1-hour rotation period, and a c) 250-meter spherical asteroid with a 7.627-hour rotation period. 1 micron grains are shown in teal, 5 micron grains in purple, and 10 micron grains in orange.

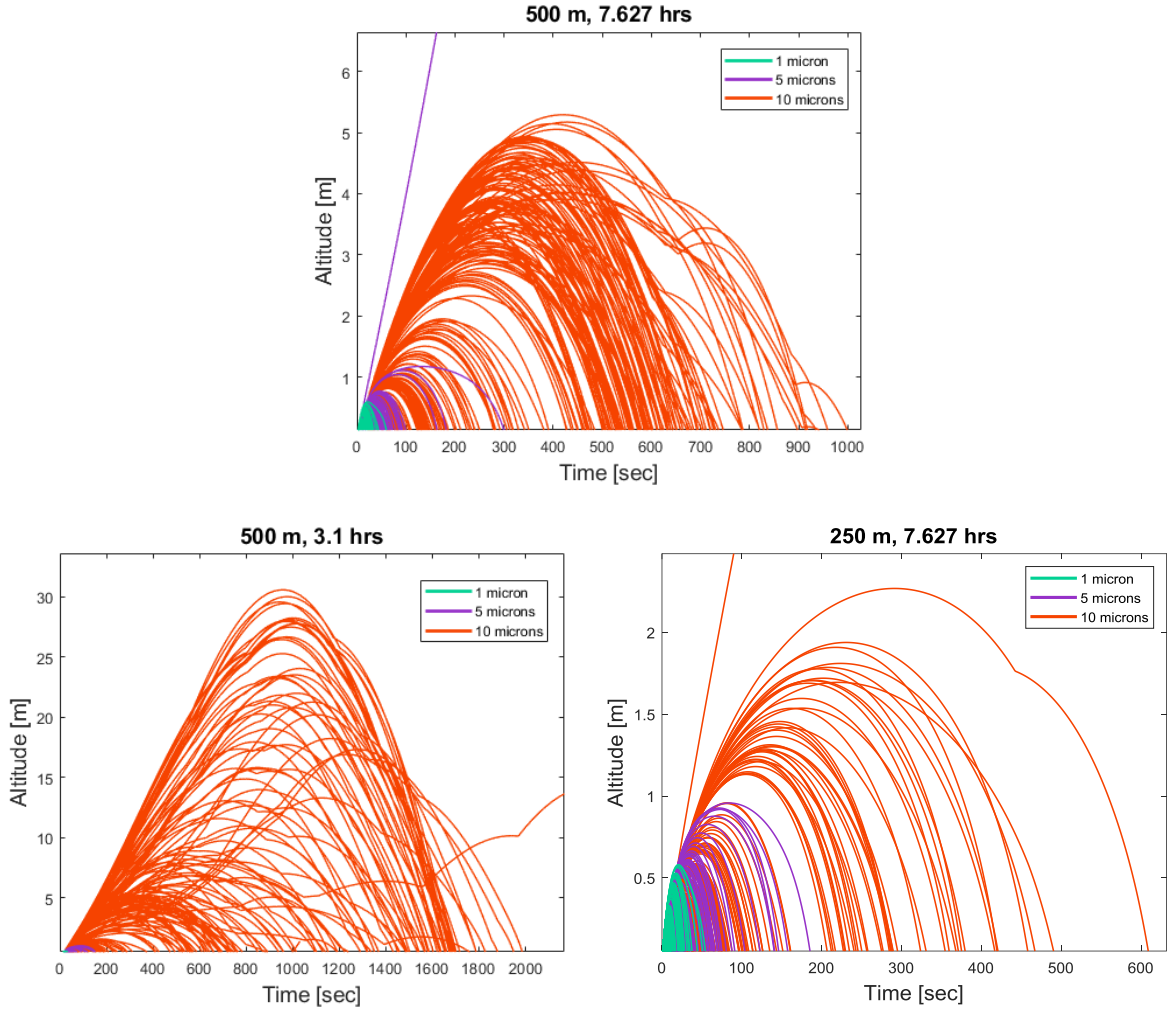

Figure 5.14: Altitudes over time of reimpacting dust grains on a) a 500-meter spherical asteroid with 7.627-hour rotation period, b) a 500-meter spherical asteroid with 3.1-hour rotation period, and a c) 250-meter spherical asteroid with a 7.627-hour rotation period. 1 micron grains are shown in teal, 5 micron grains in purple, and 10 micron grains in orange. Note that any outlier altitude is not fully shown and may appear to travel outside the plot window (includes 1-2 grains per figure).

Overall, we see that larger grains reach higher altitudes and travel for longer times than smaller grains. As discussed before, this is due to the more significant role of solar radiation pressure acting on smaller grains. Most reimpacting dust grain trajectories are smaller hops with altitudes under 30 meters for the larger grains and under 1 meter for the smaller grains. For the baseline case, most hops are below 6 meters. For the faster rotating case, lofted grains gain an additional rotational boost and reach altitudes up to 30 meters.

For the smaller body case, many more of these particles escape due to the lower surface gravity, and so the ones that remain on the surface don't have sufficient velocity to reach as high of altitudes. Most of these grains on the smaller body experience hops under 3 meters. Overall, the faster rotating case tends to produce the highest altitudes for reimpacting grains, while the smaller body case tends to produce the lowest.

Looking at the trajectory times, we see that most reimpacting trajectories occur within minutes. Larger grains reimpact the surface within 30 minutes or less, while smaller grains reimpact the surface within 3 minutes or less. As was the case for the trajectory altitudes, the faster rotating case produces the longest trajectories and the smaller body case produces the shortest trajectories, when compared to the baseline case. Additionally, the largest particles tend to have the longest trajectories, while the smallest particles tend to have the shortest. This implies that the larger 10-micron grains would be the population that has the potential to create a dusty working environment during surface operations.

5.3.3 Maximum Altitudes, Lateral Distances, and Solar Elevation Angles

Next, we look at the trends associated with the maximum altitudes, lateral distances and initial solar elevation angles of lofted dust. While we cannot in general say that solar elevation angle corresponds to time of day (it will depend on the shape of the primary body), because we are examining a spherical body in this study, lower solar elevation angles will correspond to earlier and later times in the day (near the sunrise and sunset terminator regions). Both maximum altitude and lateral distance are parameters used in this study as an indicator of mobility. They can be correlated with how far a particle of given attributes and initial conditions can be expected to travel across the surface. Figure 5.15 gives the maximum altitude as a function of solar elevation angle. Note that escaped

grains are plotted at 1 kilometer for visualization. Recall also that the solar elevation angle is measured from the local horizon. This means that an angle of 0 degrees corresponds to the terminator regions, while an angle of 90 degrees corresponds to areas experiencing local noon (Sun directly overhead).

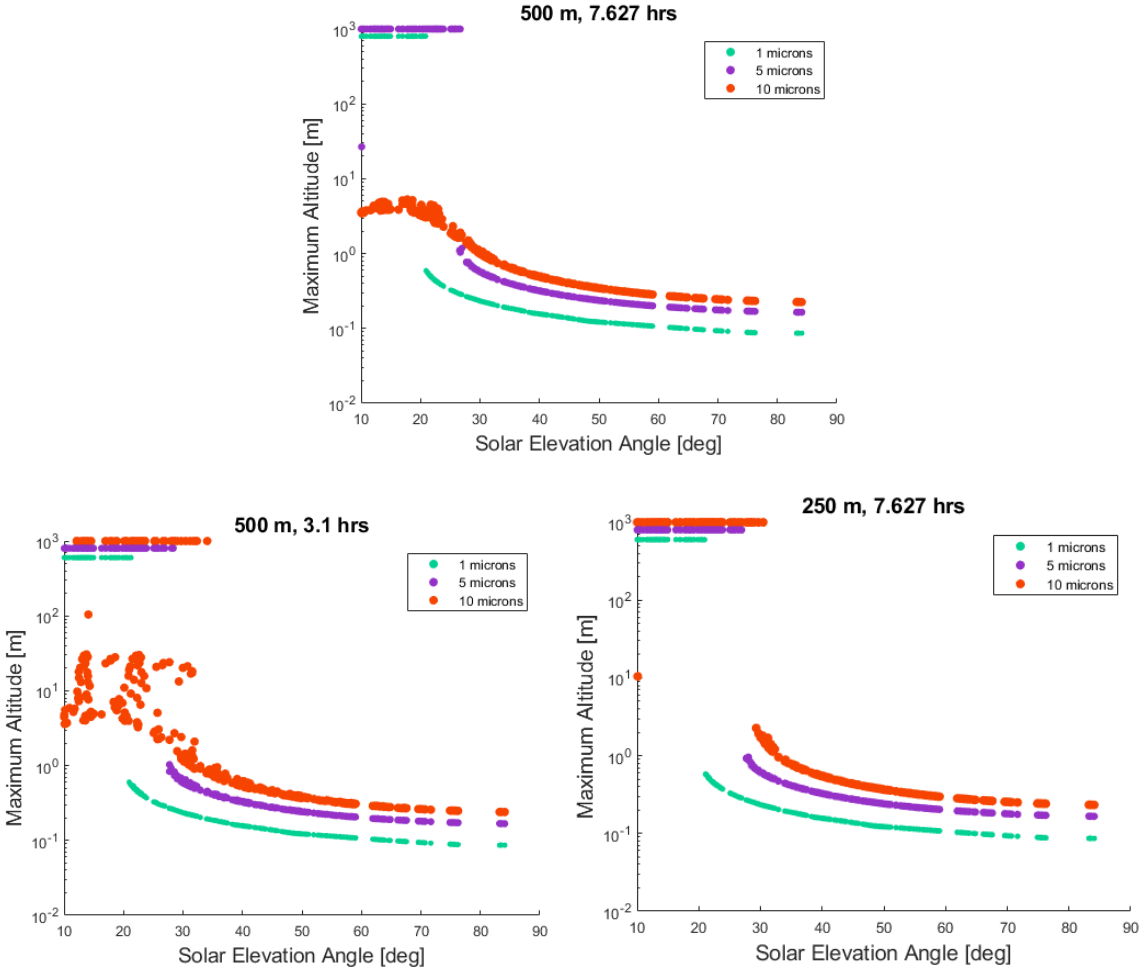

Figure 5.15: Maximum altitude reached as a function of initial solar elevation angle for dust grains lofting on a) a 500-meter spherical asteroid with 7.627-hour rotation period, b) a 500-meter spherical asteroid with 3.1-hour rotation period, and a c) 250-meter spherical asteroid with a 7.627-hour rotation period. 1 micron grains are shown in teal, 5 micron grains in purple, and 10 micron grains in orange. Note that escaped grains are plotted near 10^3 meters for visualization.

As expected, we see that grains lofted at lower solar elevation angles tend to escape more easily and have higher mobility in all three cases. This implies that earlier and later

in the local day are dustier. We also see that larger grains reach higher maximum altitudes (tens of meters) than smaller grains (tenths of meters) due to the effect of solar radiation pressure. Faster rotation appears to increase the vertical mobility of larger reimpacting grains, and decreased body size appears to eliminate nearly all grains at solar elevation angles below 20 degrees.

Because our baseline case is modeled after the asteroid Ryugu, we can make predictions about particle populations on the surface of this body and other similar bodies. Due to the higher escape rates experienced by smaller dust grains at lower solar elevation angles on our spherical Ryugu asteroid analog, we would not expect to find 1-micron and 5-micron grains on Ryugu. Over time these grains would be preferentially eliminated due to the fact that most locations on the surface experience lower solar elevation angles at some point during the local day. Furthermore, considering again the faster rotation case, if bodies like Ryugu experienced past period of rapid rotation, as scientist believed happened [25], then we would also predict that the 10-micron grains would also be preferentially lost over the time scale of asteroid evolution. Given the results of the smaller spherical body, paired with what we know about faster rotation increasing the mobility of grains, we also wouldn't expect to find 1 micron, 5 micron, or 10 micron grains on the top layer surface of Bennu, which has a 4.3 hour rotation period and is similar in size to the smaller body case. Overall,

these results reinforce the fact that we don't see finer regolith covering the surfaces of these smaller, rubble-pile asteroids [13, 52].

Next, we examine the lateral distance traveled as a function of solar elevation angle in Figure 5.16.

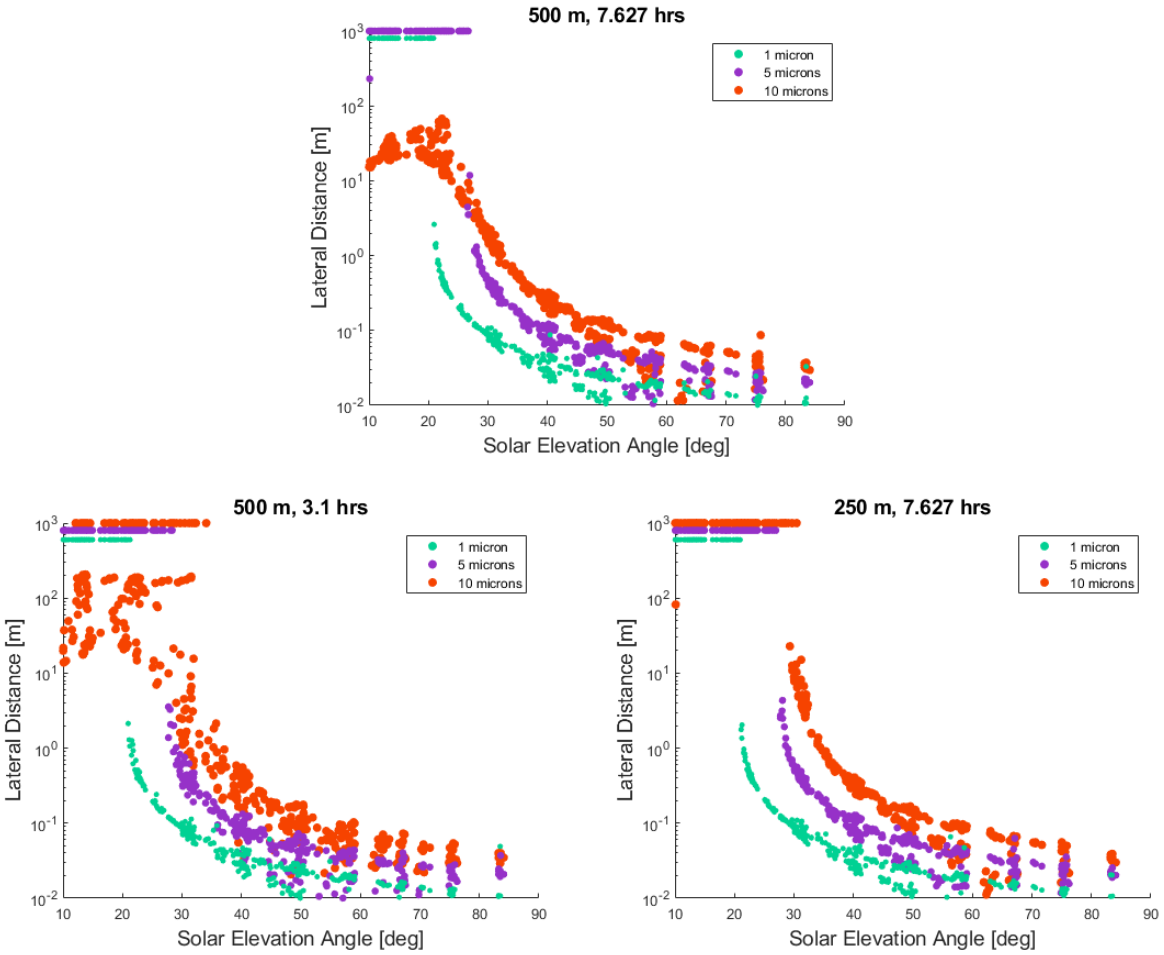

Figure 5.16: Lateral distance traveled as a function of initial solar elevation angle for dust grains lofting on a) a 500-meter spherical asteroid with 7.627-hour rotation period, b) a 500-meter spherical asteroid with 3.1-hour rotation period, and a c) 250-meter spherical asteroid with a 7.627-hour rotation period. 1-micron grains are shown in teal, 5-micron grains in purple, and 10-micron grains in orange. Note that escaped grains are plotted near 10^3 meters for visualization.

Overall, we see similar trends in mobility by grain size, as was seen in the maximum altitude plots above (Figure 5.15). The lateral distance data does appear to be more

dispersed, which means that there is a bit more variation in the distance traveled laterally by each grain. We also note that grains appear to move more laterally than they do vertically. This motion, of course, will likely be impeded by the local topographical features of a small body, such as boulders and craters, which are not modeled here.

In both Figures 5.15 and 5.16 (and throughout all the data), we see that larger grains tend to reach higher altitudes than smaller grains. Specifically, for reimpacting grains, we can examine a single location for three different sized grains to see the relative magnitudes of accelerations affecting grain behavior. Figure 5.17 shows the acceleration magnitudes for a 1-micron, 5-micron, and 10-micron grain lofted from the same location over the course of their trajectories.

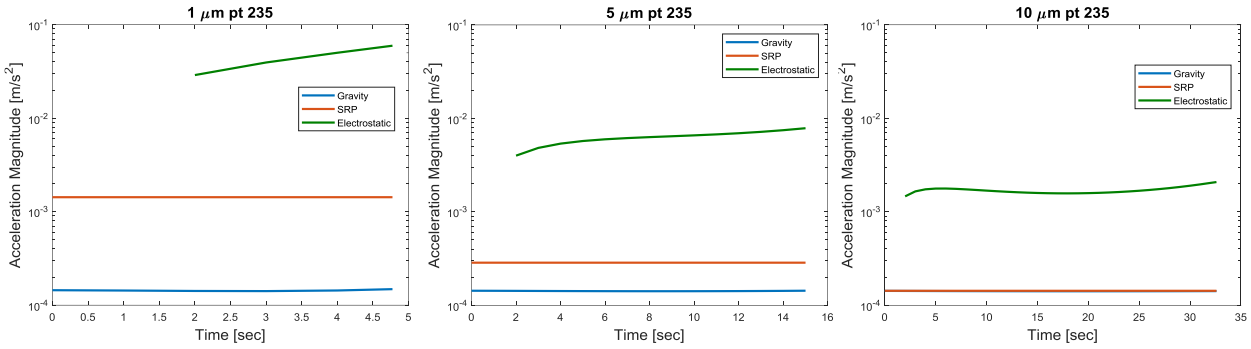

Figure 5.17: Acceleration magnitudes over time for each of the relevant perturbations—gravity (blue), electrostatics (green), and solar radiation pressure (red)—for a) a 1 micron grain, b) a 5 micron grain, and c) a 10 micron grain lofting from the same location.

Note that for this case, all three forces are acting nearly downward toward the surface. However, the larger grain experiences a smaller downward acceleration due to a lower solar radiation pressure acceleration (illustrated previously in Figure 5.12 for a different case) and a lower electrostatic acceleration. Recall that the electrostatic acceleration goes as $1/r_d^3$, and so larger grains will experience less acceleration even with a

similar electrostatic force to smaller grains. As a result, the larger grain is able to reach higher altitudes than the smaller grains.

5.3.4 Initial Latitudes, Initial Longitudes, and Delta-Longitudes

Next, we look at the trends associated with the initial latitudes, the initial longitudes, and the change in longitude that lofted grains experience. Delta-longitude is another parameter that we use to quantify lofted dust grain mobility. A delta-longitude of 0 degrees would represent a particle which hasn't moved from its initial longitude, while larger delta-longitudes indicate higher mobility. Figure 5.18 shows the delta-longitude as a function of initial latitude. Note that escaped grains are plotted at ±50 degrees delta-longitude, with the sign indicating their initial location—sunrise/west (-) or sunset/east (+).

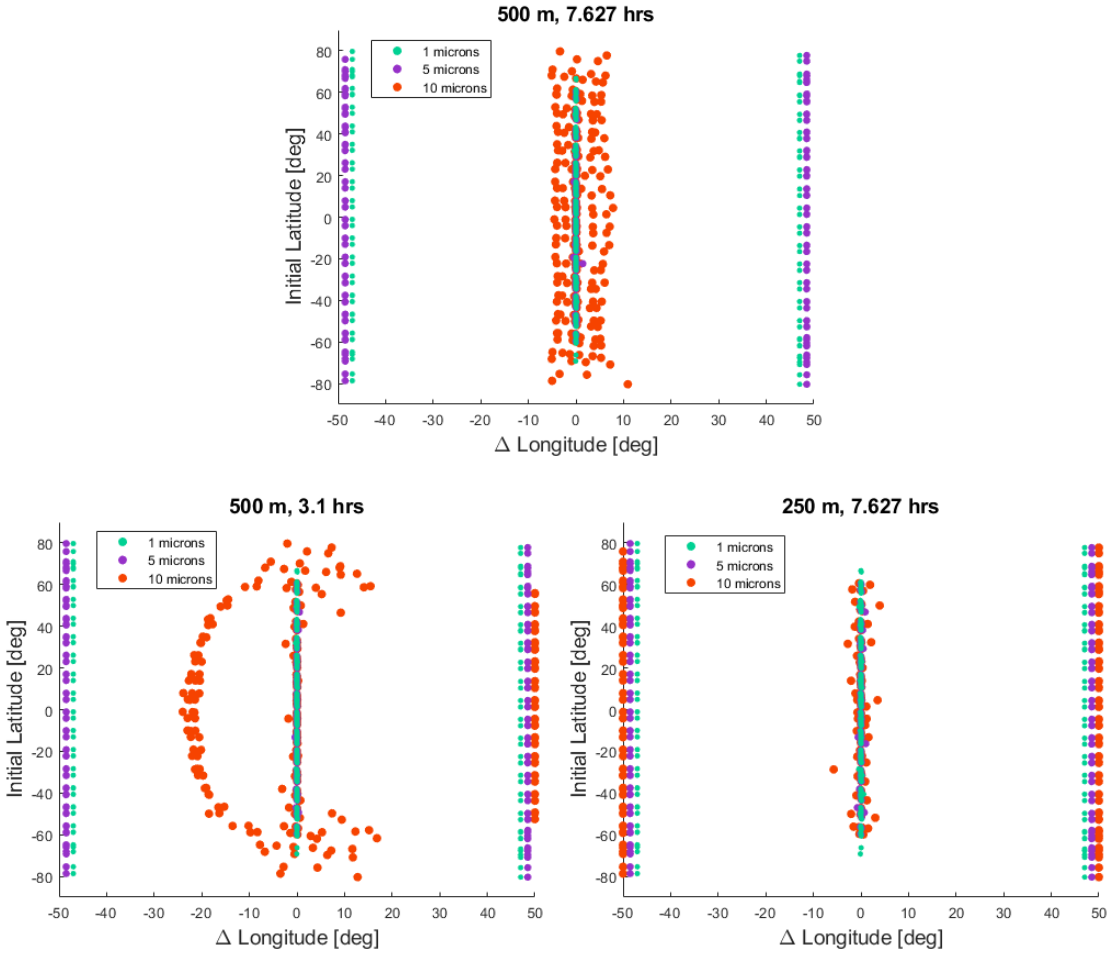

Figure 5.18: Delta-longitude as a function of initial latitude of dust grains lofting on a) a 500-meter spherical asteroid with 7.627-hour rotation period, b) a 500-meter spherical asteroid with 3.1-hour rotation period, and a c) 250-meter spherical asteroid with a 7.627-hour rotation period. 1 micron grains are shown in teal, 5 micron grains in purple, and 10 micron grains in orange. Note that escaped grains are plotted near ±50 degrees for visualization.

Overall, we see that grain escapes can occur at any of the latitudes we examined—there does not seem to be any hard limits with respect to grain escapes and initial latitudes. Looking at grain mobility, the smaller grains appear to only move within a degree of their initial lofting longitudes, while the larger grains have more mobility overall.

Looking specifically at the baseline case (top plot of Figure 5.18), we see that the larger reimpacting grains tend to move within a 10-degree arc of their initial location, while

the smaller and intermediate-sized grains typically move less than 1 degree of longitude. The data points are relatively evenly dispersed around the centerline.

Looking next at the faster rotating case (bottom left plot of Figure 5.18), we see very clearly that the faster rotation has a significant effect on particle behavior near the equator and predominantly that of the larger 10-micron grains. Increasing the rotation rate of the body increases the centripetal acceleration, in particular (see equation 3.36). This extra rotational boost, which is a factor of 6 when comparing the 3.1 hour period to the 7.627 hour period, enables lofted grains to reach higher altitudes. Once farther from the surface of the primary body, these particles are more readily swept away by solar radiation pressure and are unable to reimpact the surface. This is illustrated in the bottom left plot of Figure 5.18 where the larger lofted grains nearer the equator either travel up to 30 degrees of longitude before reimpact (left side of plot) or escape the body completely (right side of plot). The asymmetry of the plot is a function of the effect of solar radiation pressure (see Figure 5.3). On the sunrise side (westward-moving grains, negative delta-longitudes), solar radiation pressure acts against the tangential velocity of the grain to push it back into the surface and encourages reimpact. On the sunset side (eastward-moving grains, positive delta-longitudes), solar radiation pressure acts with the tangential velocity of the grain to carry the it farther from the surface and encourages escape. This manifests as the arc of reimpacting 10-micron grains on the left side of the plot and the absence of reimpacting 10-micron grains on the right side. Overall, the larger lofted grains are traveling larger distances when compared to the baseline case. Smaller lofted grains still appear to reimpact within a degree of their starting longitude.

Finally looking at the smaller primary body case (bottom right plot of Figure 5.18), we see that more grains escape overall. Given that the tangential velocity varies linearly with the radius and gravity varies cubically (mass goes as $1/R^3$), for a given reduction in

the primary body's radius, the restoring capability of the gravity force (its ability to pull the grain back into the surface) is reduced much more substantially than is the tangential velocity. As a result, grains are able to loft far enough away from the body that even grains lofting from both the sunrise and the sunset side are able to be carried away by solar radiation pressure. As a result, the remaining (smaller percentage) reimpacting grains which can't acquire sufficient height to escape the body, will land within smaller delta-longitude arcs (less than 1 degree for smaller grains, less than 6 degrees for larger grains).

Next, we examine the trends associated with initial longitude and grain mobility. Figure 5.19 shows the delta-longitude as a function of the initial longitude. Note that the axes have been transposed from the previous figure for visualization (delta-longitude is now plotted along the y-axis). Escaped particles are again plotted at ±50 degrees delta-longitude.

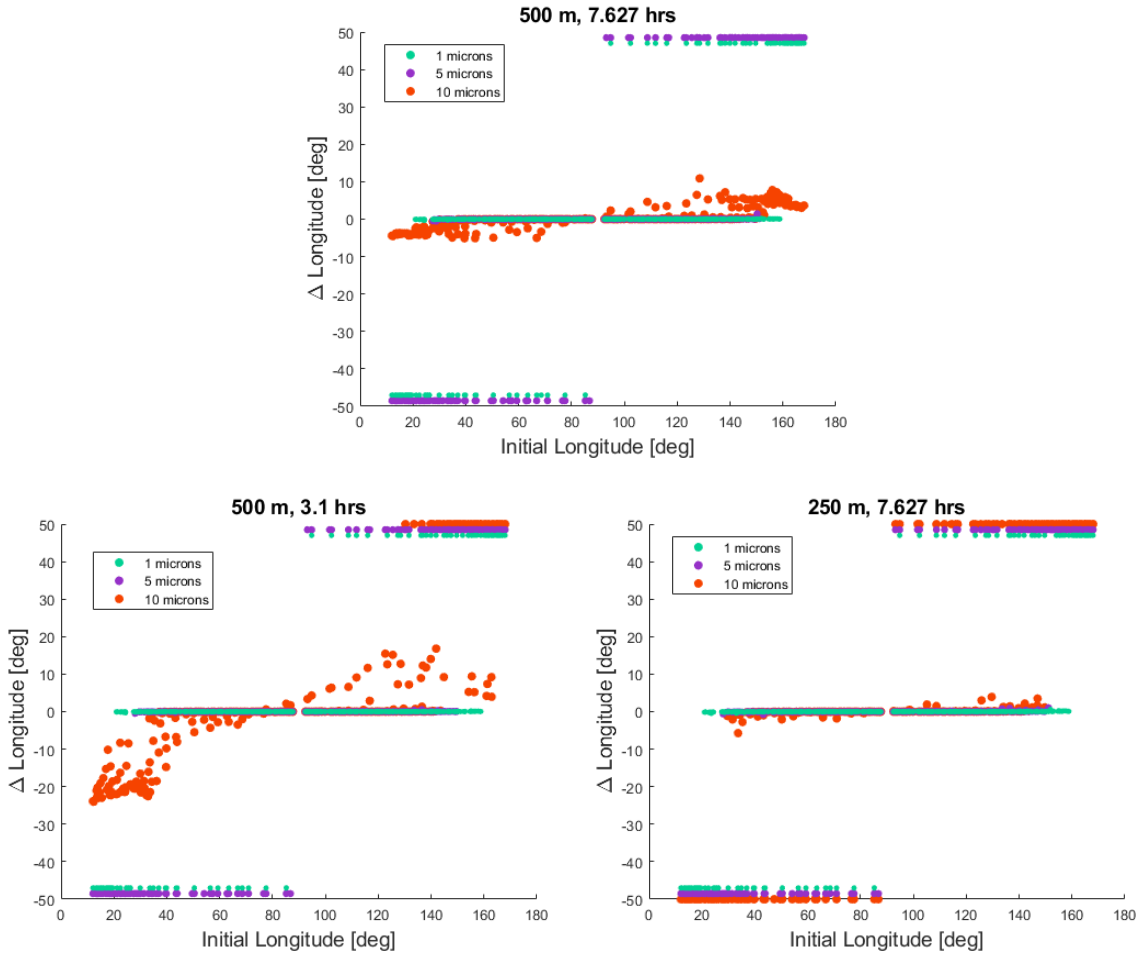

Figure 5.19: Delta-longitude as a function of initial longitude of dust grains lofting on a) a 500-meter spherical asteroid with 7.627-hour rotation period, b) a 500-meter spherical asteroid with 3.1-hour rotation period, and a c) 250-meter spherical asteroid with a 7.627-hour rotation period. 1 micron grains are shown in teal, 5 micron grains in purple, and 10 micron grains in orange. Note that escaped grains are plotted near ±50 degrees for visualization.

We again see that there does not appear to be a hard limit on initial longitudes that lead to particle escapes—all longitudes examined led to particle escapes for certain conditions. Looking at the baseline case (top plot of Figure 5.19), we see that grains lofted earlier in the day (smaller longitudes) travel westward, while grains lofted later in the day

(larger longitudes) travel eastward. This is consistent with the effect of solar radiation pressure discussed above and in Figure 5.3.

Looking at the faster rotating case (bottom left plot of Figure 5.19), we see that this relationship is exaggerated due to the extra rotational boost of the faster rotation. Additionally, we see that larger grains lofted later in the day tend to receive enough of a boost from the centripetal acceleration and solar radiation pressure that they are able to escape.

Finally, looking at the smaller body case (bottom right plot of Figure 5.19), we again see that many more lofted grains are able to escape, particularly larger grains on both the sunrise and sunset sides. The remaining reimpacting grains follow a similar trend to the baseline case but with even lower mobility (due to the higher percentage of escaping particles).

5.3.5 Summary & Implications

Our study establishes that, given the latest charging models for the surfaces of airless bodies, dust lofting may occur frequently and across a wide range of initial conditions for grains sizes of microns up to several tens of microns. We look at a range of particles sizes, locations, primary body sizes, and spin rates, and are able to examine the conditions when particles loft and escape frequently. We then compare these conditions to when particles are not very mobile at all (ineffective lofting) and identify a marginal set in between. In this way we can bracket the main quantities of interest and provide analysis of the desired populations of particles. For all cases and combinations of particle size and asteroid spin, we find that particles can loft for weakly cohesive surfaces.

Solar radiation pressure appears to be a driving force of lofted dust grain behavior in the near-surface environment. In fact, larger dust grains can achieve higher altitudes and

larger lateral distances than their smaller grain counterparts due to the role of solar radiation pressure more strongly retarding upward motion of smaller grains. This, in addition to a smaller electrostatic acceleration (due to the cubic dependence on grain radius), manifests in larger grains having more mobility (in general and up to a limit). However, larger mobility does not necessary mean larger escape rates, and in fact, the larger 10 micron particles may be the population that causes a dusty environment to persist at the surface if these particles are not able to escape but continue to reach high altitudes at various times throughout the local day.

For particles lofted near the terminator region at low solar elevation angles, solar radiation pressure acts to carry these grains farther from the surface where many are able to escape the small body completely. From our study of lofted grain escape events on spherical asteroids, we would not expect to find particles microns to several microns in size on the top layer of surface at bodies such as Ryugu and Bennu. And in fact, observations of these bodies confirm that there is no fine regolith on their surfaces [52], in contrast to asteroids such as Eros which has ponded dust deposits of fine regolith less than 50 microns in size [38]. There also exists an asymmetry in particle behavior depending on the initial location of lofting. Grains lofted from the sunrise side tend to travel westward and reimpact the surface due to solar radiation pressure acting against the grain's motion. Grains lofted from the sunset side tend to travel eastward and experience more grain escapes due to solar radiation pressure acting with grain motion. This implies that sunrise may provide a more hazardous and dusty working environment for mission operations on the surface of small bodies. Aiming to work around local noon appears to be the cleanest time of day on the surface.

Both faster rotation and smaller size of the primary body result in more particle loss events—one due to the additional rotational boost from an increased centripetal

acceleration (a 6x difference in our case) and the other due to lower gravitational attraction (a 8x difference in our case). If we assume past periods of rapid rotation occurred in a body's past [25], we likely wouldn't expect to find large populations of particles microns to several microns in size on the top layer surface due to the elimination of these populations by solar radiation pressure. However, as larger grains migrate and are transported across and off the surface in the present day, remnants of the smaller grain population may be uncovered from deeper layers in the regolith. In this way, these smaller grains may loft with behaviors observed in the slower rotating baseline case (i.e. present-day spin period of 7.627 hours) simulation.

The next iteration of this simulation, discussed in the following section, incorporates the complex geometries of specific asteroids such as Itokawa, Ryugu, and Eros. Modeling lofted grain motion in the near surface environment of both spherical and complex shaped asteroids is important in determining the affect that a small body's shape has on electrostatically-driven dust behavior.

5.4 Complex Itokawa, Ryugu, and Eros Simulations

In the final study, we survey electrostatic dust lofting on three primary bodies—Itokawa, Ryugu, and Eros—using their complex shape models. All bodies are simulated at a distance of 1 AU from the Sun. Dust grain radii range from 0.5 micron to 15 microns and a grain density of 2.4 g/cm^3 is used in all cases. All shape models use 1016 facets and 510 vertices in this study. We use the method of determining initial conditions developed in section 4.4. An effective gravity force is used in this study, which accounts for the centripetal acceleration of the rotating small body. Recall that the charging conditions are achieved quickly (on the order of 10^2 sec) and grains can loft at multiple times throughout the local day. Here we study this by looking at a snapshot in time of one sunlit face of the primary body at a time. Initial lofting locations within the sunlit face were chosen based on

the solar elevation angles. Facets with solar elevation angles larger than 10 degrees (limited by the plasma sheath model) on a given sunlit side and not shadowed by the concavity of the body's topography were chosen as lofting locations. For each sunlit facet, a dust grain is placed at the center and given relevant initial conditions at maximum charge, which enable it to electrostatically loft from the surface. In this way, dust grains at a variety of times throughout the local day are simulated. Note that in this study we assume a negative charge on the dust grain, as is consistent with electrostatic lofting due to grain-scale supercharging.

The surface is modeled using smooth facets; individual rocks and boulders are not explicitly modeled. Such features would provide interesting lighting conditions and post-lofting obstacles for mobile dust grains. For instance, a boulder may keep a dust grain in shadow longer than other sunlit regions in the area. This could lead to an accumulation of dust grains in the vicinity of larger boulders due to the inability of these grains to charge in sunlight for sufficient periods of time. Furthermore, any grains that are able to loft may be physically blocked from moving away by the boulder if their maximum altitudes are lower than the obstacle (or if they are too close to reach any appreciable height). Specific instances of how boulders and other features may affect lofting are discussed in the individual results sections for each of the different bodies examined, using what we know of their local surface conditions from exploration missions and observations.

Primary body density and rotation period are specific to each body studied, as are the calculated initial dust grain conditions. These values are provided in each of the individual asteroid sections below. For comparison between the bodies, Table 5.5 provides relevant parameters such as surface gravity, escape speed, and rotation period for the bodies under consideration.

Table 5.5: Relevant parameters for the small bodies of interest.
Parameter references for Itokawa [13], Ryugu [23, 52], and Eros [58, 64].

Body Name	Mass	Mean Radius	Surface Gravity	Surface Escape Speed	Rotation Period	Bulk Density
Itokawa	3.51×10^{10} kg	173 m	7.8×10^{-5} m/s^2	16 cm/s	12.1 hrs	1.9 g/cm^3
Ryugu	4.50×10^{11} kg	460 m	1.4×10^{-4} m/s^2	36 cm/s	7.63 hrs	1.2 g/cm^3
Eros	6.687×10^{15} kg	7311 m	8.3×10^{-3} m/s^2	11 m/s	5.27 hrs	2.67 g/cm^3

In our analysis of dust lofting on these bodies, we examine parameters such as maximum altitude, lateral distance traveled, and escape rate. Each of these parameters gives insight into the level of mobility of different dust grain populations. The maximum altitude and lateral distance parameters can be compared with the local topographical features of each body to see if dust grain ponding is possible; while the escape rate can be used to determine if different populations of grains are likely to be present on the surfaces, or if they are preferentially eliminated over long periods of time.

We begin by examining the results for the complex Ryugu shape model, as this case will most resemble the spherical Ryugu-like shape simulated in Section 5.3. We then analyze the more elongated shapes of Itokawa and Eros, and end with a discussion of all the implications.

5.4.1 Ryugu Results

Asteroid (162173) Ryugu was the destination of the JAXA Hayabusa2 mission, which analyzed the surface at close range using various rovers and landers and returned surface samples to Earth in 2020. It has a spinning-top shape with an equatorial ridge and an equatorial radius of 502 meters. Ryugu's shape is believed to be caused by a past period of rapid rotation whereby centrifugally induced deformation occurred [52]. Its low bulk density indicates a high porosity in the interior, while an abundance of large surface boulders suggests a rubble-pile structure [52]. The surface is dominated by large grains (>1 centimeter) and boulders (>25.6 centimeters) uniformly distributed across the entire surface, while no fine regolith particles are observed [52]. For comparison to Itokawa (and

Bennu), the number density of boulders larger than 20 meters is twice as large on Ryugu with a value of approximately 50/km^2 [30]. The largest boulder "Otohime" has dimensions 160 meters by 120 meters by 70 meters; however, boulders larger than 40 meters are rare on Ryugu [30]. Ryugu's spin axis is perpendicular to the ecliptic plane and its rotation direction is nearly retrograde [52]. While its distance from the Sun varies throughout its elliptical orbit from 0.9633 AU to 1.4159 AU, a circular orbit at a distance of 1 AU is used in the simulation here. Four cases were chosen which capture the different sunlit faces shown in Figure 5.20.

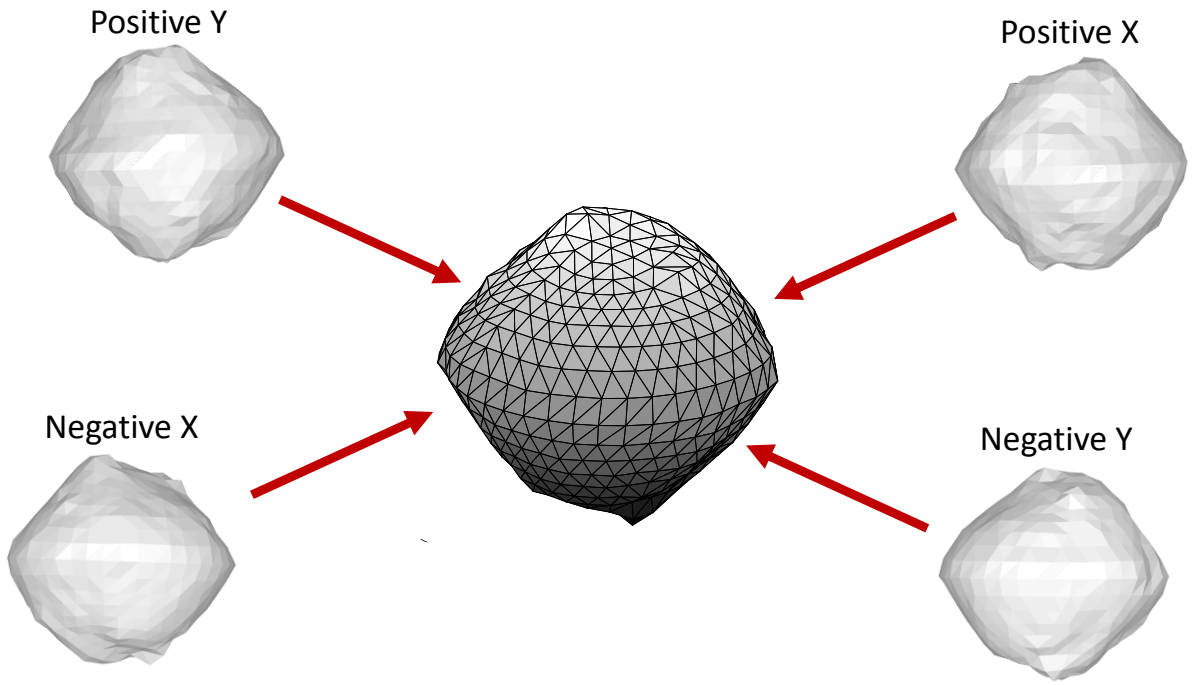

Figure 5.20: Complex shape model of asteroid Ryugu with the sunlit surfaces of the four cases of study shown.

Simulated dust grain sizes range from 1 to 10 microns. The associated ejection velocities and cohesive strengths at maximum gap electric field conditions are given in Table 5.6. Ryugu has a surface escape speed near 36 cm/s. Lofted dust grain speeds in this simulation are well below this value at 3-6 cm/s.

Table 5.6: Grain initial conditions on Ryugu using the grain-scale supercharging model.

Grain Radius	Initial Charge	Ejection Velocity	Cohesive Strength
1 μm	-2.889e-18 C	5.90 cm/s	1.3912 Pa
5 μm	-3.424e-17 C	4.02 cm/s	0.6464 Pa
10 μm	-9.331e-17 C	3.02 cm/s	0.3646 Pa

The trajectories of reimpacting dust grains are shown in Figure 5.21. The 5- and 10-micron grains appear to be the most mobile reimpacting populations with a few notable 5-micron trajectories reaching significant altitudes without escaping. The 1-micron particles tend to either have low mobility or escape.

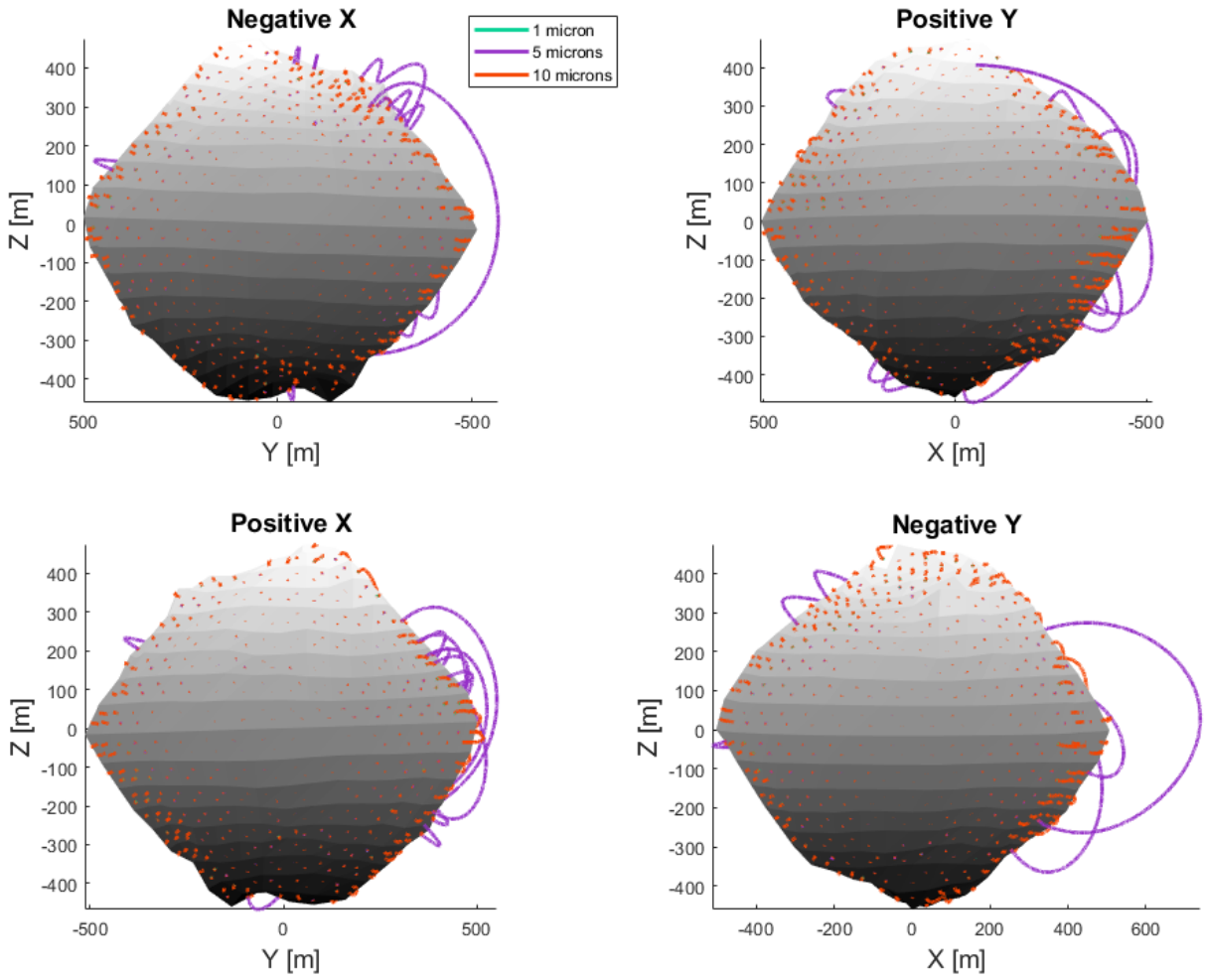

Figure 5.21: Reimpacting dust grain trajectories on Ryugu for (a) negative X face, (b) positive Y face, (c) positive X face, and (d) negative Y face. 1-micron grains are shown in teal, 5-micron grains in purple, and 10-micron grains in orange. Escaped particle trajectories are not shown.

The initial locations of escaped dust grains are shown in Figure 5.22. Again, we see that the escape locations tend to be around the periphery of the sunlit faces, suggesting a large role of solar radiation pressure in eliminating populations of dust grains from small bodies.

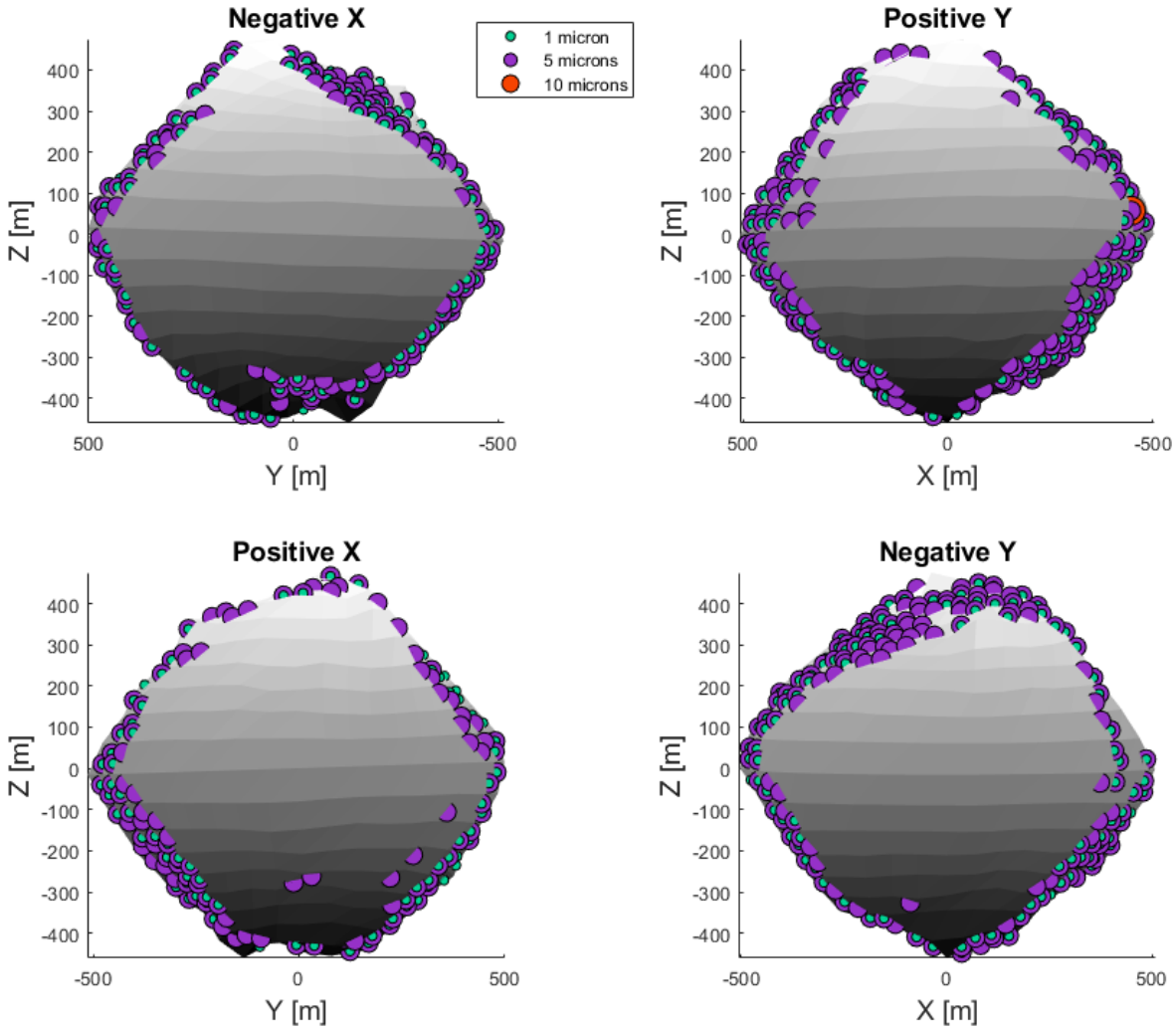

Figure 5.22: Escaped particle initial locations on Ryugu for (a) negative X face, (b) positive Y face, (c) positive X face, and (d) negative Y face. 1-micron grains are shown in teal, 5-micron grains in purple, and 10-micron grains in orange.

Specific particle escape event statistics are given in Table 5.7. Nearly a quarter (23%) of the population of 1-micron particles and even more (32%) of the 5-micron particles were able to escape. Only a single 10-micron grain escaped.

Table 5.7: Escaped particle statistics for Ryugu by particle size and sunlit face of body.

Face	Total Locations	1 micron	5 microns	10 microns
Negative X	431	103 (24%)	125 (29%)	0 (0%)
Positive Y	413	94 (23%)	143 (35%)	1 (0%)
Positive X	412	77 (19%)	112 (27%)	0 (0%)
Negative Y	426	114 (27%)	160 (38%)	0 (0%)
Overall	1682	388 (23%)	540 (32%)	1 (0%)

Next, we look at the maximum altitudes of lofted dust grains as a function of solar elevation angle in Figure 5.23. Note that escaped grains are plotted at 10^3 meters for visualization.

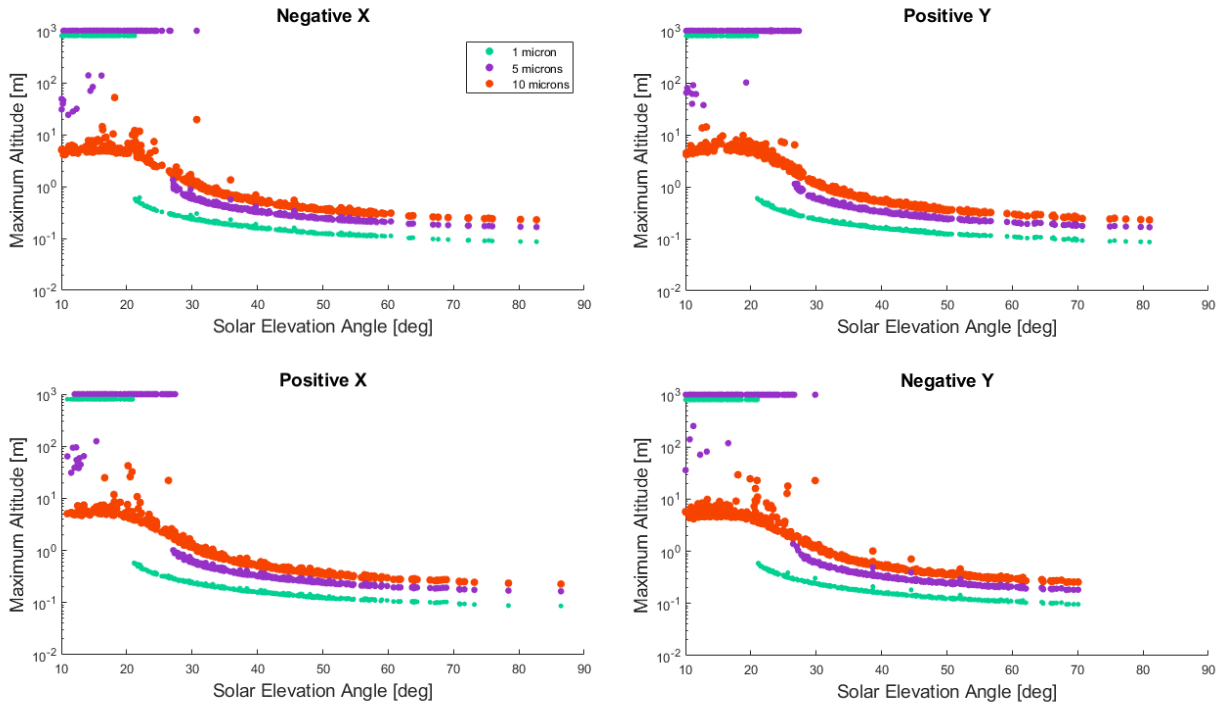

Figure 5.23: Maximum altitude reached as a function of initial solar elevation angle for dust grains lofting on Ryugu. Results shown for (a) negative X face, (b) positive Y face, (c) positive X face, and (d) negative Y face. 1-micron grains are shown in teal, 5-micron grains in purple, and 10-micron grains in orange. Escaped grains are plotted at 10^3 meters for visualization.

Similar to the results of the spherical Ryugu-like asteroid, we see that dust grains are more mobile at lower solar elevation angles (earlier and later in the day) and

particularly below 20-30 degrees solar elevation angle. This increased mobility at lower angles is due to the effect of solar radiation pressure. Note that average maximum altitudes and lateral distances will be discussed in the following paragraphs. These parameters are calculated above and below this inflection point in the data (usually around 20-30 degrees) to give a more accurate representation of grain behavior than if we were to average over the entire data set at once. In this way, we can more completely describe the behavior of lofted dust as a function of solar elevation angle. We also see that the larger 10-micron reimpacting grains are again able to reach higher altitudes than the smaller 1- and 5-micron grains due to the more significant effect of solar radiation pressure on the smaller grains.

As noted previously in Table 5.7, nearly all the larger 10-micron dust grains reimpact the surface (only one particle escapes). The 10-micron population overall has an average maximum altitude of 4.9 meters below 30 degrees and 54 centimeters above 30 degrees, which is smaller than many of Ryugu's boulders [52]. As a result of their limited mobility, thee dust grains may not be able to accumulate on the surface, and thus wouldn't be easily observed. This could explain why we don't see this population of grains on Ryugu. Additionally, recall from our spherical asteroid simulations that past periods of faster rotation likely eliminated the 10-micron grain population from the surface of Ryugu- and Bennu-like bodies.

Reimpacting 5-micron grains reach an average maximum altitude of 71 meters below 26 degrees and 37 centimeters above 26 degrees. Many (but not all) 5-micron grains below 27 degrees escape the body completely. A few of these grains at low solar elevation angles reach significant altitudes without escaping. This would imply that we might expect to find some small fraction of this population on the surface of Ryugu; however, as was the case with Itokawa, these electrostatic processes acting over millions of years will likely lead to this dust grain population being preferentially carried away from the surface by solar

radiation pressure. If any of these grains still existed on the surface (post preferential loss), perhaps underneath the top layer of regolith, they could contribute to a dusty working environment in the near-surface region.

Reimpacting 1-micron grains reach an average maximum altitude of 20 centimeters. However, all 1-micron grains below 20 degrees escape the body, implying that 1-micron grains would not remain on the surface long term (since solar elevation angle changes throughout the local day). Thus, we would not expect to find this population of particles on the surface of Ryugu today, which aligns with observations of no fine dust [52].

Next, we look at the distance traveled laterally by lofted dust grains as a function of solar elevation angle in Figure 5.24. Again, we plot escaped particles at 10^3 meters for visualization.

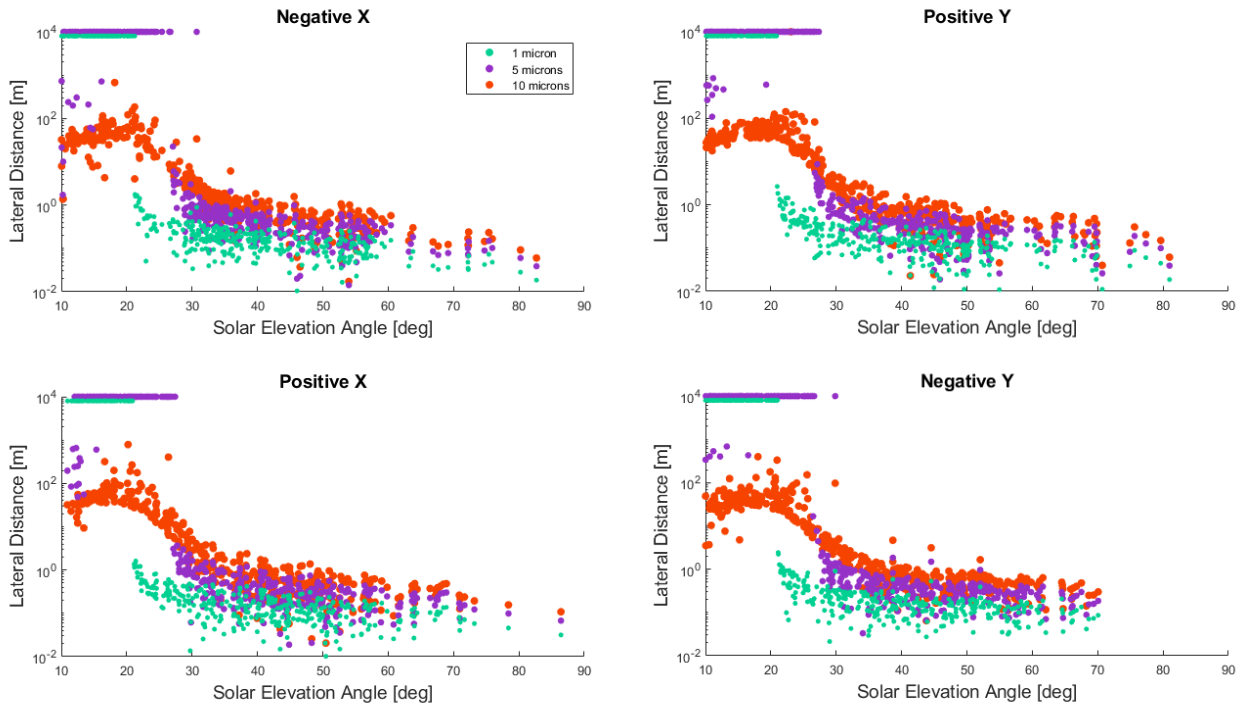

Figure 5.24: Lateral distance traveled as a function of initial solar elevation angle for dust grains lofting on Ryugu. Results shown for (a) negative X face, (b) positive Y face, (c) positive X face, and (d) negative Y face. 1-micron grains are shown in teal, 5-micron grains in purple, and 10-micron grains in orange. Escaped grains are plotted at 10^4 meters for visualization.

Here we see that reimpacting (nearly all) 10-micron grains move an average lateral distance of 42 meters below 30 degrees and 81 centimeters above 30 degrees. This distance could be limited, however, if larger boulders keep these reimpacting grains contained to their local area. Thus, if these particles were still present on Ryugu, we might find them in the vicinity of larger boulders. Reimpacting 5-micron grains move an average of 340 meters laterally below 26 degrees and only 53 centimeters above 26 degrees. This reinforces the idea that grains lofting at lower incidence angles are much more mobile than those lofting at higher incidence angles. Reimpacting 1-micron grains move an average lateral distance 21 centimeters. All 1-micron grains escape below 30 degrees solar elevation angle. These grains are more binary nature, meaning that they either escape or move very little away from their starting locations. Although as mentioned previously, the 5 micron and 10-micron dust populations have likely been eliminated completely from at least the topmost layer of surface material on the body by solar radiation pressure and periods of faster rotation.

5.4.2 Itokawa Results

Asteroid (25143) Itokawa was the target of the JAXA Hayabusa mission, which collected dust particles from the surface and returned them to Earth aboard a spacecraft in 2010. It has an elongated, peanut shape with dimensions of 535 meters by 294 meters by 209 meters [13]. Due to its low bulk density, high porosity, boulder-rich appearance and shape, Itokawa is considered to be a rubble-pile asteroid. It is believed to have experienced several large impacts, including an early collisional breakup followed by re-agglomeration into its current rubble pile state [13]. Surface material ranges in size from millimeter to centimeter scale up to 50 meters. The largest boulder, Yoshinodai, measures 50 meters by 30 meters by 20 meters [39]. The number density of boulders larger than 20 meters is approximately 25/km^2 [30]. Areas of smooth terrain are concentrated in local potential lows

such as the neck region, where millimeter to centimeter-sized gravel tends to settle [13]. Fine, powdery regolith particles (sub-millimeter in size) do not appear to be present on the surface of Itokawa [13]. Its spin axis is nearly perpendicular to the ecliptic plane and its rotation direction is retrograde. While Itokawa's distance from the Sun varies throughout its orbits (0.9530 AU to 1.6947 AU), a distance of 1 AU (circular orbit) was used in the simulation here. Four simulation cases were chosen which capture different unique sunlit faces, as shown in Figure 5.25.

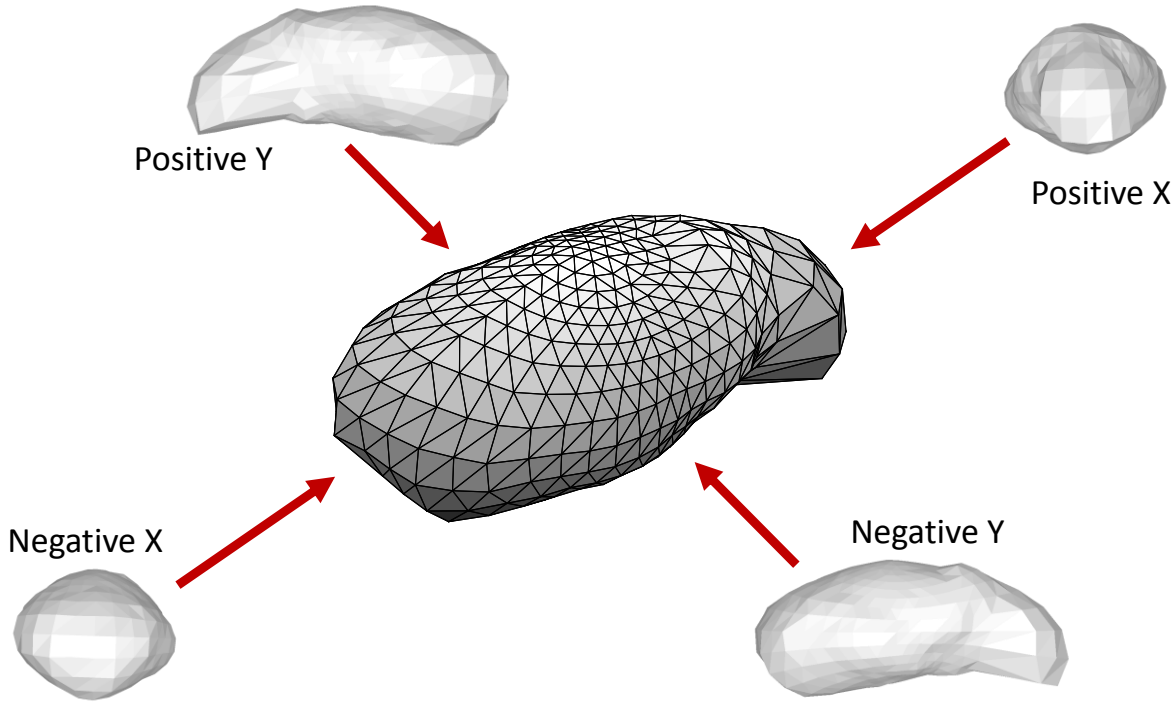

Figure 5.25: Complex shape model of asteroid Itokawa with the sunlit surfaces of the four cases of study shown.

Dust grain sizes simulated range from 5 to 15 microns. The associated ejection velocities and cohesive strengths at the maximum gap electric field condition are given in Table 5.8. Itokawa is smaller than Ryugu and much more elongated in shape. It has a surface escape speed near 16 cm/s. Lofted grain speeds in this simulation remain below this value near 2-4 cm/s.

Table 5.8: Grain initial conditions on Itokawa using the grain-scale supercharging model.

Grain Size	Initial Charge	Initial Velocity	Cohesive Strength
5 μm	-3.424e-17 C	4.02 cm/s	0.6464 Pa
10 μm	-9.331e-17 C	3.02 cm/s	0.3646 Pa
15 μm	-1.632e-16 C	2.45 cm/s	0.2395 Pa

The trajectories of reimpacting dust grains are shown in Figure 5.26. The 10 and 15 micron grains appear to be the most mobile of the reimpacting grains. The smaller 5 micron grains have a few higher trajectories, but overall appear to move the least.

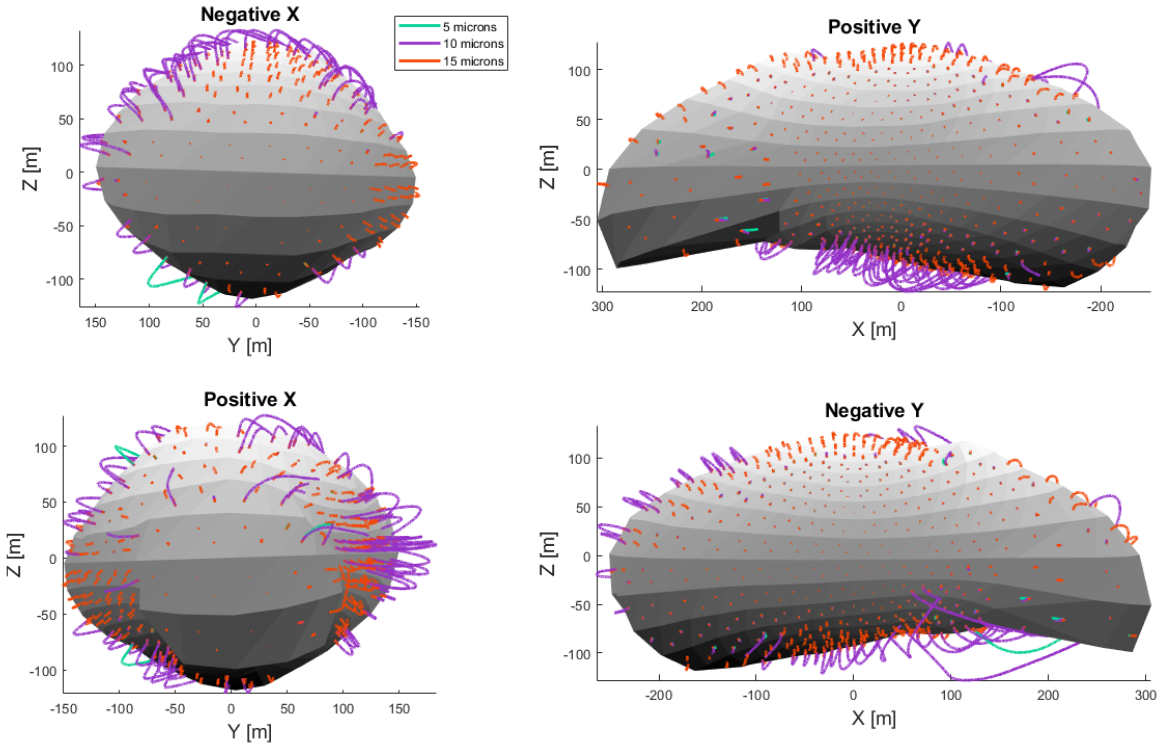

Figure 5.26: Reimpacting dust grain trajectories on Itokawa for (a) negative X face, (b) positive Y face, (c) positive X face, and (d) negative Y face. 5 micron grains are shown in teal, 10 micron grains in purple, and 15 micron grains in orange. Escaped particle trajectories are not shown.

The initial locations of escaped dust grains are shown in Figure 5.27. Unsurprisingly the locations tend to be around the periphery of the sunlit faces, suggesting that solar radiation pressure plays a major role in eliminating these grains from the surface of the body. In particular, we note that the few escaping 15-micron grains tend to be on the sunset

side of the body. As discussed in our spherical simulation results previously, this is due to the fact the solar radiation pressure is acting with grain motion on this side of the body, and thus is able to carry these larger grains farther from the body where some are able to escape completely.

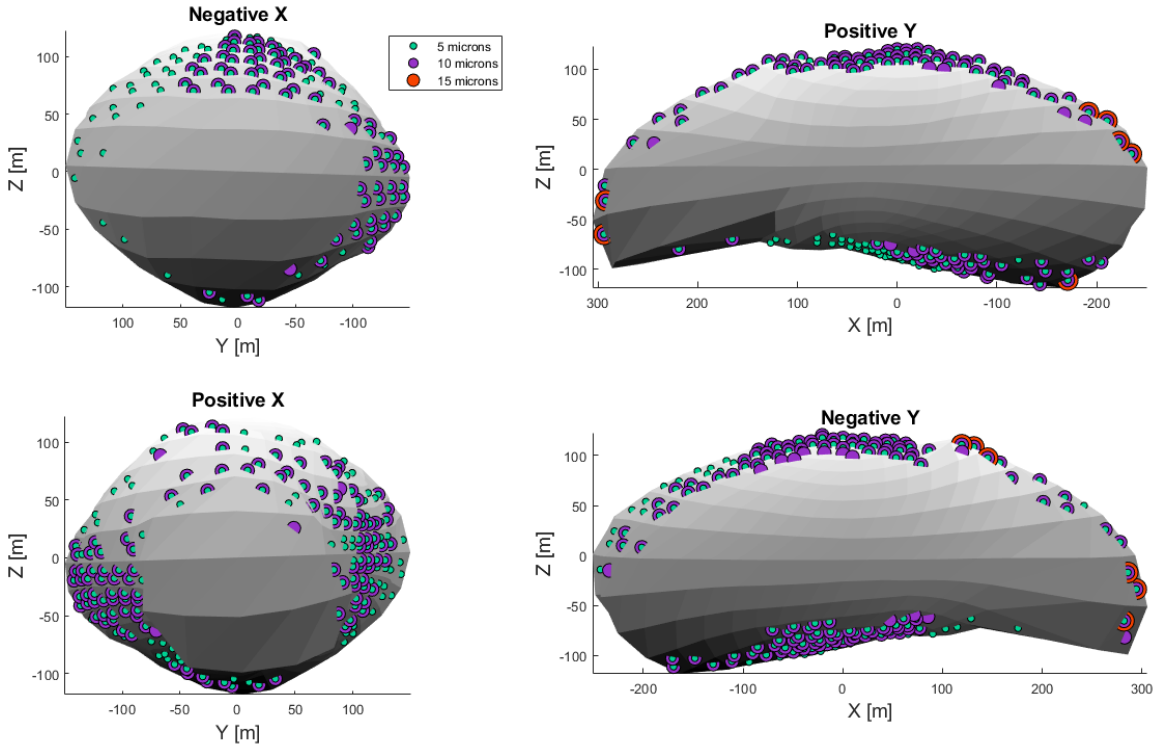

Figure 5.27: Escaped particle initial locations on Itokawa for (a) negative X face, (b) positive Y face, (c) positive X face, and (d) negative Y face. 5 micron grains are shown in teal and 10 micron grains in purple.

Particle escape event statistics are given in Table 5.9. We see that nearly half (47%) the population of 5 micron grains escape and 35% of the 10 micron grains escape. Very few of the 15-micron grains (1%) escape. Given the high escape rates of 5- and 10-micron grains, we would not expect to find these population on the surface of Itokawa.

Table 5.9: Escaped particle statistics for Itokawa by particle size and sunlit face of body.

Face	Total Locations	5 microns	10 microns	15 microns
Negative X	181	124 (69%)	77 (43%)	0 (0%)
Positive Y	428	140 (33%)	109 (25%)	7 (2%)
Positive X	238	184 (77%)	122 (51%)	0 (0%)
Negative Y	432	158 (37%)	139 (32%)	6 (1%)
Overall	1279	606 (47%)	447 (35%)	13 (1%)

It's also interesting to note that the X-faces tend to have higher escape rates for both 5 micron and 10-micron grains. This could be an artifact of the smaller X-faces having less surface area, particularly in the center where facets with intermediate to high solar elevation angles would populate the region. When compared to the elongated Y-faces, which have a greater percentage of facets populating the intermediate and high solar elevation angle space, the smaller X-faces have a much lower percentage of high solar elevation angle facets in this space. This results in the observed bias of higher escape rates on X-faces since lower solar elevation angles correlate with higher particle escapes. The higher escape rate could also be affected by the fact that the X-faces are situated at a longer distance from the rotational axis, and thus grains lofting from there gain an additional boost in velocity.

Next, we look at the maximum altitudes of lofted dust grains as a function of solar elevation angle in Figure 5.28. Here we plot escaped grains at 10^3 meters for visualization.

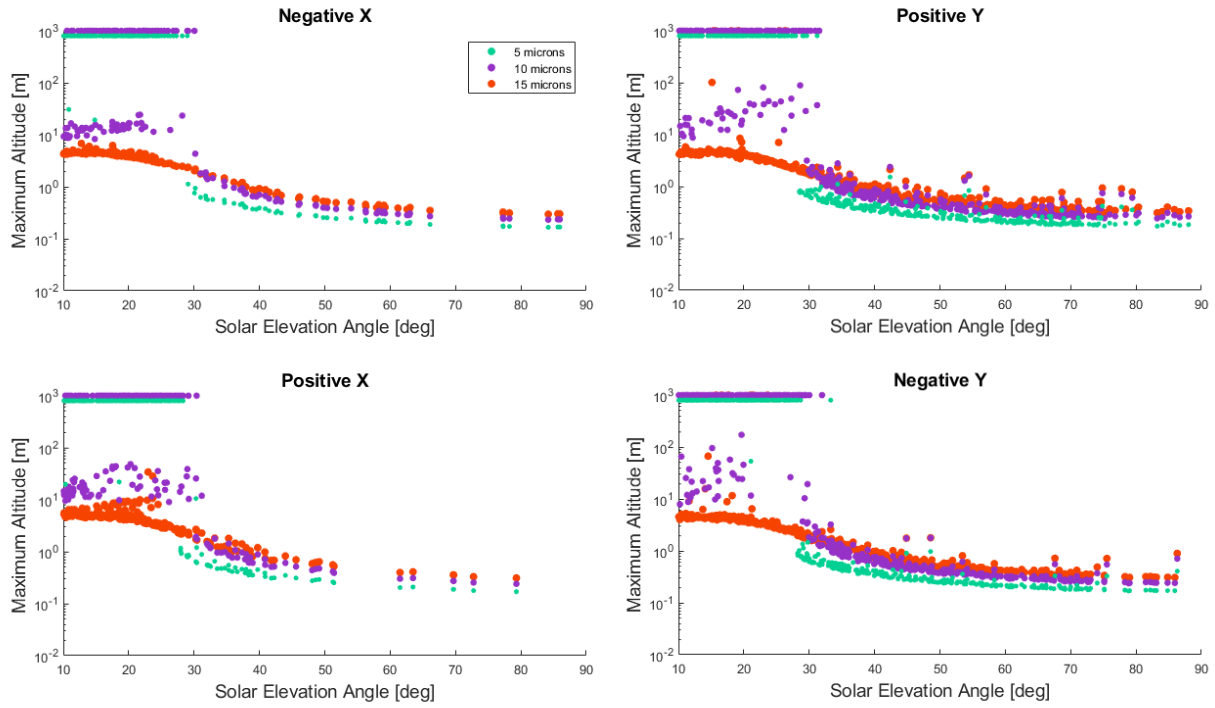

Figure 5.28: Maximum altitude reached as a function of initial solar elevation angle for dust grains lofting on Itokawa. Results shown for (a) negative X face, (b) positive Y face, (c) positive X face, and (d) negative Y face. 5 micron grains are shown in teal, 10 micron grains in purple, and 15 micron grains in orange. Escaped grains are plotted at 10^3 meters for visualization.

Overall, we see that dust grains are more mobile at lower solar elevation angles (earlier and later in the day) and particularly at angles below 30 degrees. The larger 15-micron reimpacting grains reach higher altitudes than their smaller 5-micron counterparts. As was shown in the spherical asteroid simulations (Figure 5.17), this is directly related to solar radiation pressure and its more significant role in decelerating smaller grains back toward the surface. Interestingly and unlike our previous results, we see that some of the 10-micron grains are able to reach higher maximum altitudes than the 15-micron grains at low solar elevation angles. We started to see this behavior appear in the complex Ryugu case, but it is more accentuated for the body here due to its elongated geometry and slower spin rate (12.1-hour period).

Looking at the 15-micron grains, nearly all 15-micron grains reimpacted the surface. The average maximum altitude of these particles is 2.9 meters (4.7 meters below 30 degrees and 78 centimeters above 30 degrees), which is smaller than many boulder's on Itokawa's surface [13]. This could affect movement of this population of grains and keep them from accumulating so that observation is possible. There is also the possibility that these grains were eliminated from the surface during past periods of faster rotation.

Reimpacting 10-micron grains reach an average maximum altitude of 21 meters below 30 degrees and 1.7 meters above 30 degrees. It's interesting to note that many of these grains at lower solar elevation angles do not escape and are quite mobile. However, given the high percentage of particle escapes for this grain population and the long evolutionary history of asteroids, most of these particles would have been eliminated from the surface over time.

Reimpacting 5-micron grains reach an average maximum altitude of 4.6 meters below 30 degrees and 35 centimeters above 30 degrees. However nearly all the 5 micron grains below 30 degrees escape the body—only a few do not. Thus, we would expect that this population of dust would have been preferentially eliminated over time and would not be present in larger numbers on the upper surface of Itokawa.

Finally, we look at the lateral distance traveled by lofted dust grains as a function of solar elevation angle in Figure 5.29. Again, we plot escaped particles at 10^3 meters.

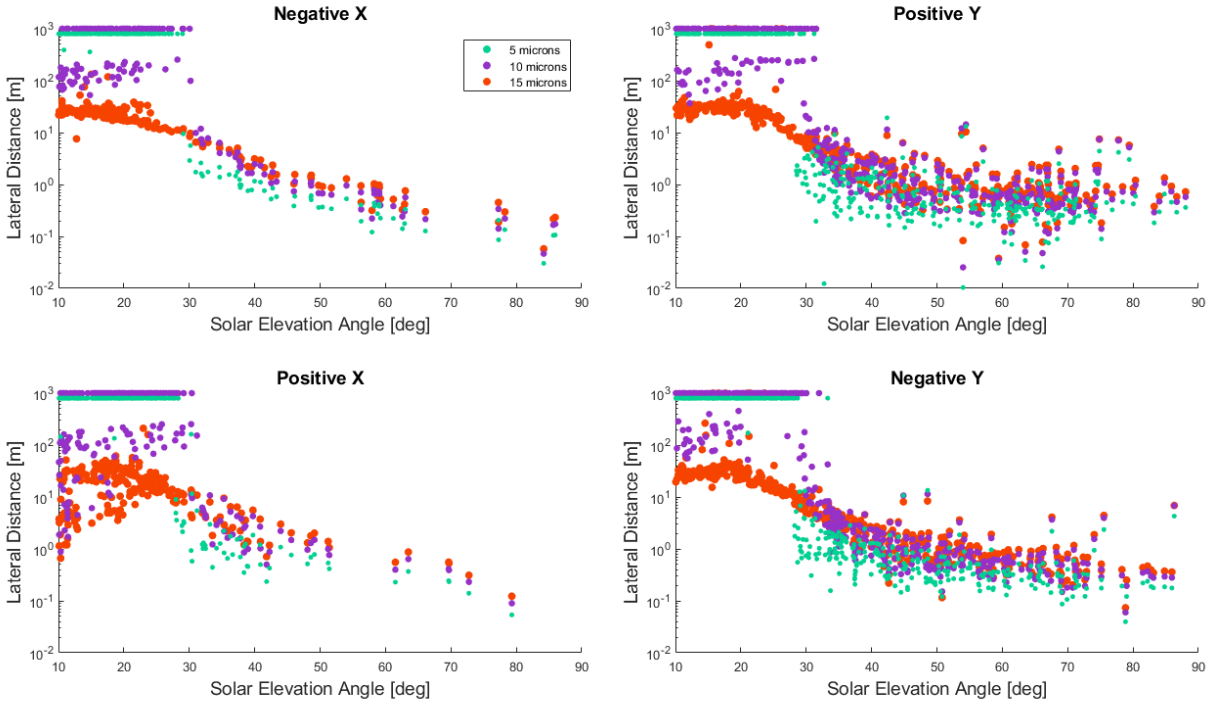

Figure 5.29: Lateral distance traveled as a function of initial solar elevation angle for dust grains lofting on Itokawa. Results shown for (a) negative X face, (b) positive Y face, (c) positive X face, and (d) negative Y face. 5 micron grains are shown in teal, 10 micron grains in purple, and 15 micron grains in orange. Escaped grains are plotted at 10^3 meters for visualization.

Overall, we see that grains appear to move more laterally than they do vertically; however, this is likely affected by the existence of large boulders on the surface. For example, we see that reimpacting (nearly all) 15-micron grains move an average lateral distance of 24 meters (35 meters below 30 degrees and 2.1 meters above 30 degrees). With a maximum altitude less than 5 meters, these grains will have difficulty moving freely around large boulders and other features on the surface.

Reimpacting 10-micron grains move an average lateral distance of 366 meters below 30 degrees and 58 meters above 30 degrees. This grain population tends to be very mobile on Itokawa at lower solar elevation angles, with many moving hundreds of meters away from their starting location. If any of this grain population still exists on the surface of Itokawa, they may deposit into gravitational lows.

Reimpacting 5-micron grains move an average lateral distance of 35 meters below 30 degrees and 1.1 meters above 30 degrees. This population tends to be more binary in its behavior with grains below 30 degrees escaping and those above 30 degrees moving less than a meter from their initial location. As mentioned above, this grain population has likely been eliminated from the surface completely, which agrees with observations of no fine dust on the surface of Itokawa [13].

5.4.3 Eros Results

Asteroid (433) Eros was visited by the NEAR Shoemaker spacecraft in 1998, becoming the first asteroid studied in detail from orbit. It has an elongated, peanut shape with dimensions 34 kilometers by 11 kilometers by 11 kilometers [49] and is the second largest near-Earth object. It is much more massive than Itokawa, Bennu, and Ryugu discussed previously. The largest features are a 5.5-kilometer crater (0.9 kilometers in depth) and an irregularly shaped saddle depression 10 kilometers across [49]. The surface has a variety of grooves, ridges, and lineations that run across it, some of which suggest compressive failure from a large impact [49]. The depressions have depths of a few tens of meters [49]. The surface is also covered in craters, with crater densities nearing the empirically derived saturation limit of heavily cratered terrains [49]. An exception to this is the saddle region, which has crater densities lower than the average by a factor of 10, suggesting that the surface in this region is affected by processes other than impacts [49]. Observations of the surface overall suggest that it is covered in a fine regolith [49].

Of special interest are the ponded deposits at the bottom of craters on Eros [38]. In the visible range, the ponds appear bluer than the surrounding material, which suggests very fine grains sizes (< 50 microns) [38]. The depths of the ponded deposits are only a few meters, while the surrounding non-pond material tends to be rich in boulders (centimeters to meters in diameter) [38]. The vast majority of ponds (91%) are distributed within 30

degrees of the equator, and particularly in regions where the gravitational potential is lowest [38]. Eros's obliquity (88 degrees) results in the equator of the asteroid being in terminator-like lighting conditions a large percentage of the time, which could explain how electrostatically-driven dust motion creates ponds preferentially in this region [38].

While Eros's distance from the Sun varies from 1.13 AU to 1.73 AU throughout its orbit [49], a value of 1 AU (circular orbit) is used here. Eros has a unique spin axis inclined 88 degrees to the normal of the ecliptic plane. At certain points in its orbit, Eros has a single face toward the Sun, while at other points it rotates along its short axis with multiple faces going through sunlight. As a result of this unique rotation, we identified 6 cases to simulate, which capture the different orientations and sunlit faces the body experiences throughout its orbit. These six cases are shown in Figures 5.30 and 5.31 below. The true anomaly (TA) angle is used to track the body's motion around the Sun (assuming a circular orbit here), while the rotation angle (ϕ) is used to track the body's rotation about its own spin axis.

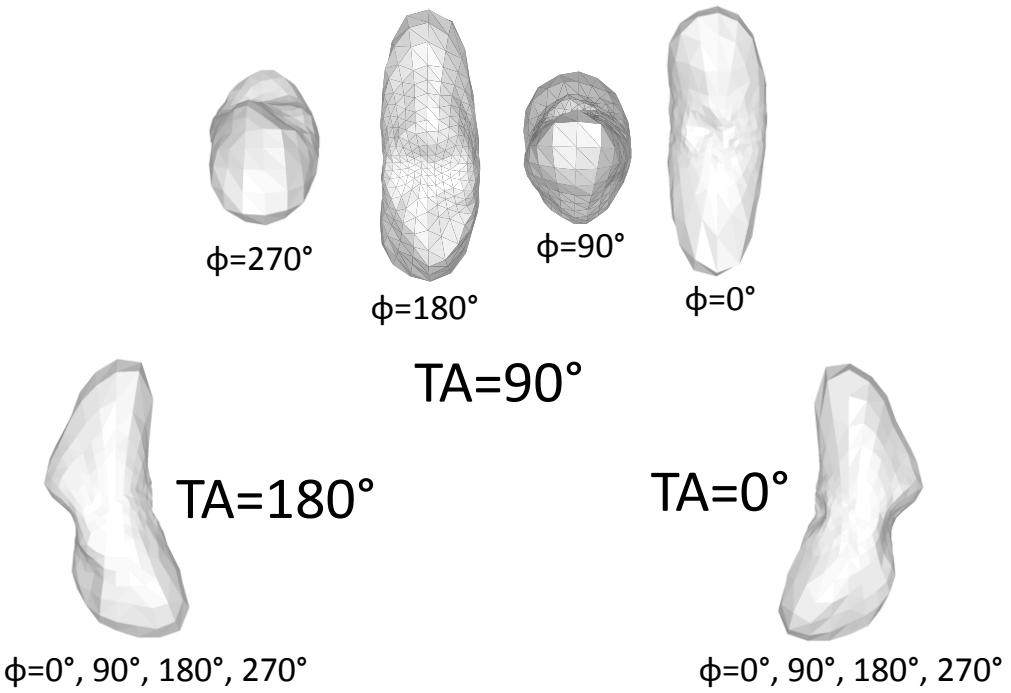

Figure 5.30: Six orientations of Eros as it travels in its orbit around the Sun. The true anomaly (TA) angle tracks the asteroid in its orbit about the Sun, while the phi (φ) angle tracks the asteroids rotation about its own spin axis. Note that the cases for TA=0 degrees and TA=180 degrees rotate with a single face toward the Sun for all phi angles.

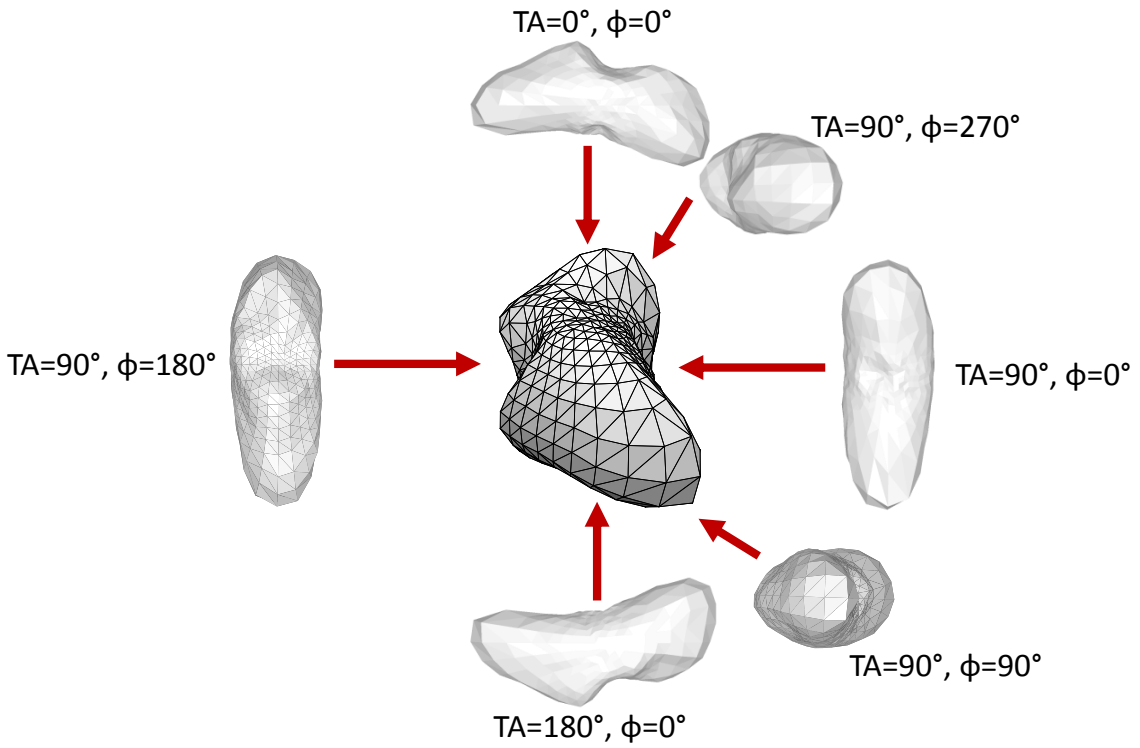

Figure 5.31: Complex shape model of asteroid Eros with the sunlit surfaces of the six cases of study shown.

Dust grain sizes simulated range from 0.5 micron to 10 microns. The associated ejection velocities and cohesive strengths at maximum gap electric field condition are given in Table 5.10. Eros is much more massive than either Ryugu or Itokawa and has an escape speed of 11 m/s. Lofted dust grain velocities in this simulation are well below this at 3-6 cm/s.

Table 5.10: Grain initial conditions on Eros using the grain-scale supercharging model.

Grain Size	Initial Charge	Initial Velocity	Cohesive Strength
0.5 μm	-9.451e-19 C	6.29 cm/s	1.5832 Pa
1 μm	-2.889e-18 C	5.90 cm/s	1.3912 Pa
5 μm	-3.424e-17 C	4.02 cm/s	0.6464 Pa
10 μm	-9.331e-17 C	3.02 cm/s	0.3646 Pa

The trajectories of reimpacting dust grains are shown in Figure 5.32. Here we see that the most mobile reimpacting particles are 0.5 and 1 micron in size; however, there are very few larger trajectories off the surface (as was seen for Itokawa and Ryugu). Both the 5

micron and 10-micron dust populations tend to move very little from their starting locations, at least in terms of the relative size of dust motion on the larger body.

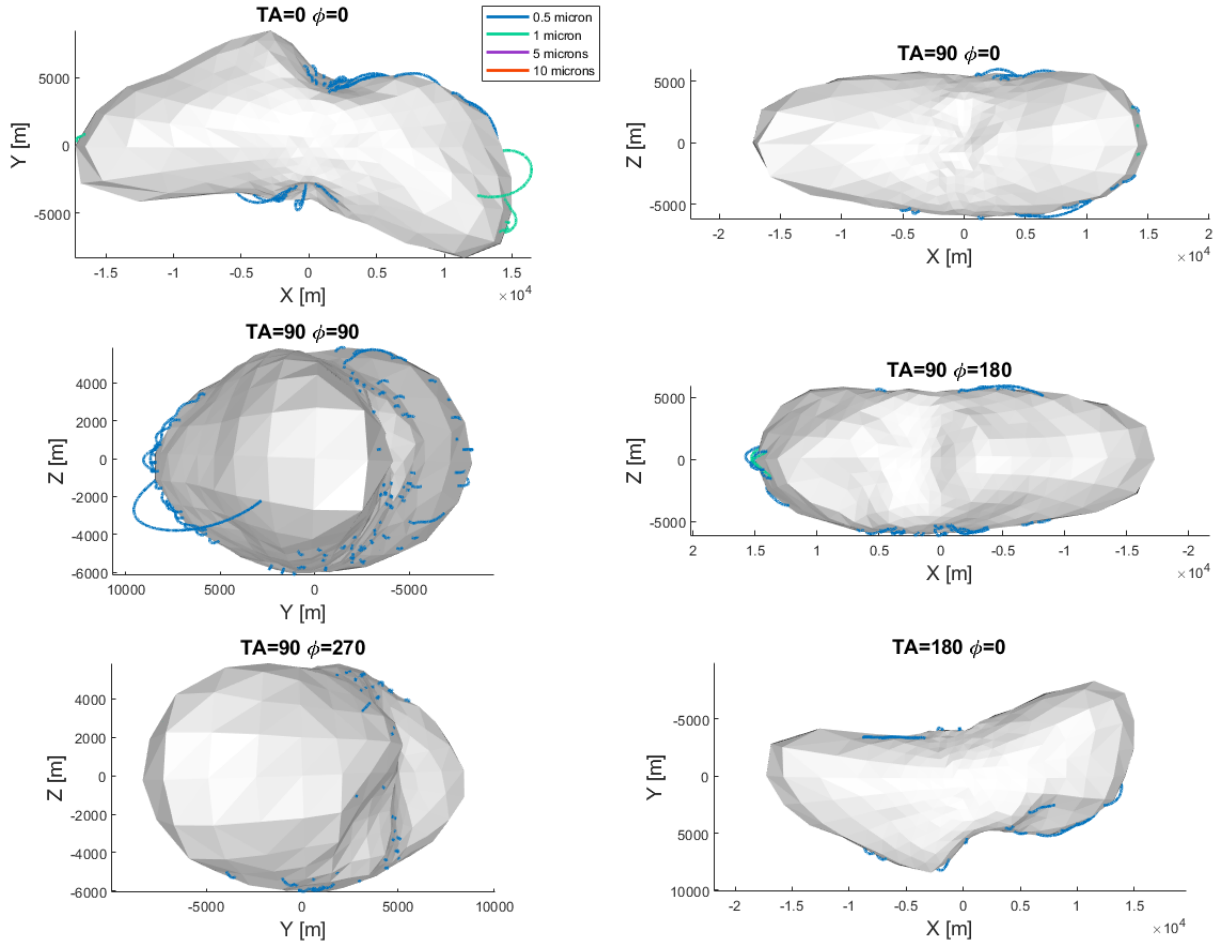

Figure 5.32: Reimpacting dust grain trajectories on Eros for (a) TA = 0 deg and phi = 0 deg, (b) TA = 90 deg and phi = 0, (c) TA = 90 and phi = 90 deg, (d) TA = 90 deg and phi = 180 deg, (e) TA = 90 deg and phi = 270 deg, and (f) TA = 180 deg and phi = 0 deg. 0.5 micron grains are shown in blue, 1 micron grains in teal, 5 micron grains in purple, and 10 micron grains in orange. Escaped particle trajectories are not shown.

The initial locations of escaped dust grains are shown in Figure 5.33. Overall, we find there is very little fine dust loss from the surface of Eros. Any grains that do escape tend to be around the periphery of the sunlit faces due to the effect of solar radiation pressure.

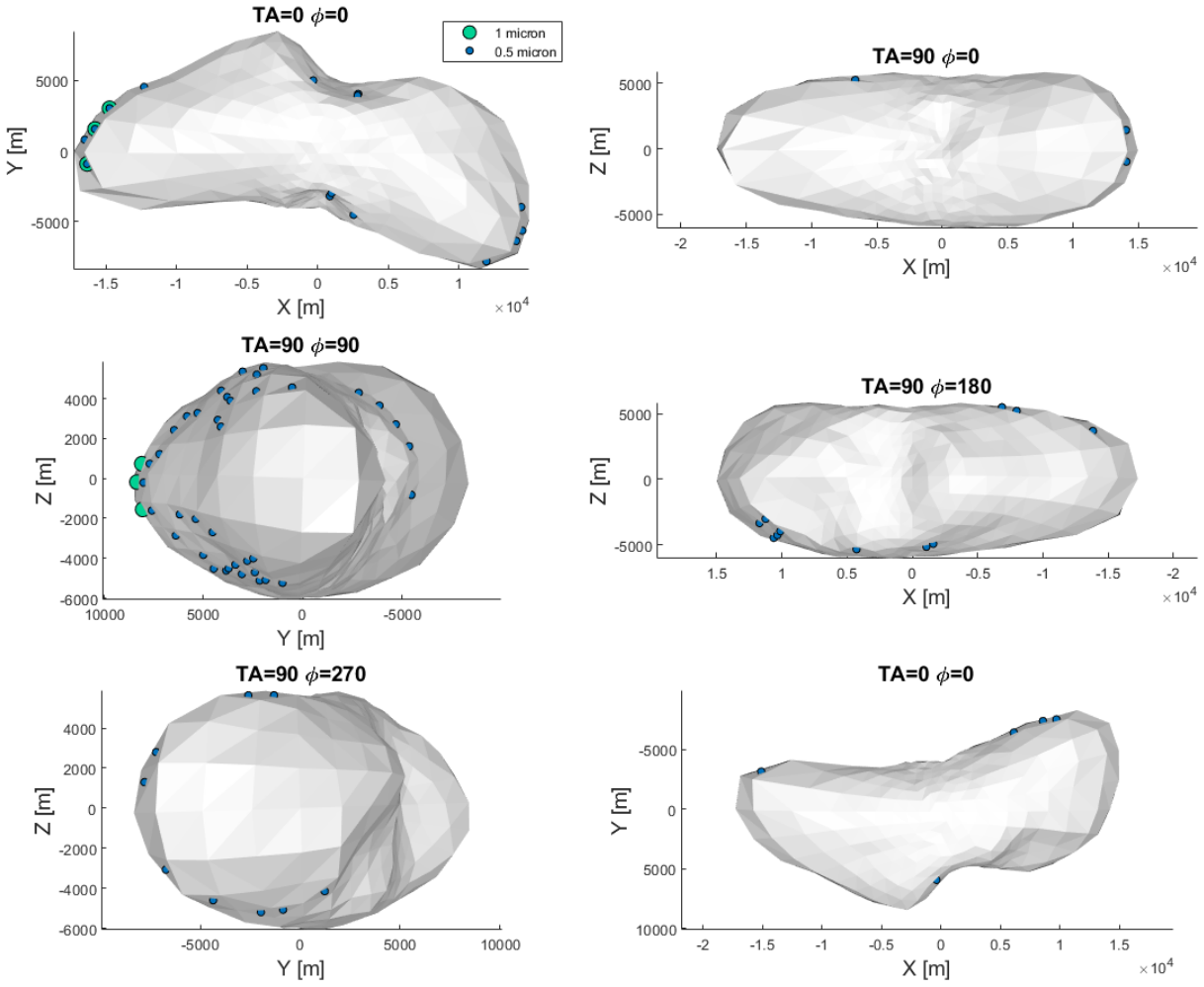

Figure 5.33: Escaped particle initial locations on Eros for (a) TA = 0 deg and phi = 0 deg, (b) TA = 90 deg and phi = 0, (c) TA = 90 and phi = 90 deg, (d) TA = 90 deg and phi = 180 deg, (e) TA = 90 deg and phi = 270 deg, and (f) TA = 180 deg and phi = 0 deg. 0.5 micron grains are shown in blue and 1 micron grains are shown in teal.

Particle escape event statistics for each population are given in Table 5.11. Very few (4%) of the population of 0.5-micron particles escape while even less (6 grains, 0%) of the 1-micron grains escape. We also note that again there is a slightly higher percentage of grain escapes off the smaller ends of the asteroid, as was seen for Itokawa due to the elongated shape. None of the grains in the 5 micron and 10 micron populations were able to escape. With a maximum escape rate of 4%, we would expect to find all of these grain populations

on the surface of Eros today. This aligns with the observation that Eros holds onto finer regolith particles [49].

Table 5.11: Escaped particle statistics for Eros by particle size and sunlit face of body.

Face	Total Locations	0.5 micron	1 micron	5 microns	10 microns
TA = 0, phi = 0	463	15 (3%)	3 (1%)	0 (0%)	0 (0%)
TA = 90, phi = 0	475	3 (1%)	0 (0%)	0 (0%)	0 (0%)
TA = 90, phi = 90	252	38 (15%)	3 (1%)	0 (0%)	0 (0%)
TA = 90, phi = 180	445	11 (2%)	0 (0%)	0 (0%)	0 (0%)
TA = 90, phi = 270	202	9 (4%)	0 (0%)	0 (0%)	0 (0%)
TA = 180, phi = 0	426	5 (1%)	0 (0%)	0 (0%)	0 (0%)
Overall	2263	81 (4%)	6 (0%)	0 (0%)	0 (0%)

We next look at the maximum altitudes of lofted dust grains as a function of solar elevation angle in Figure 5.34. Here, escaped grains are plotted at 10^5 meters for visualization. As was the case for the previous two bodies, we see that dust does appear to be more mobile at lower solar elevation angles. However, the angle that this transition occurs at seems to decrease (closer to 15 degrees) in the case of Eros. Perhaps this is a function of the size of the primary body, whereby the transition of solar elevation angles between facets is more gradual than on the smaller bodies. As a result, for a given solar elevation angle (say 30 degrees) there is more body for the dust grain to reimpact once it is lofted and carried back by solar radiation pressure. In the case of the previous two smaller asteroids, there was less body behind the grain, and it was able to escape more easily without reimpact.

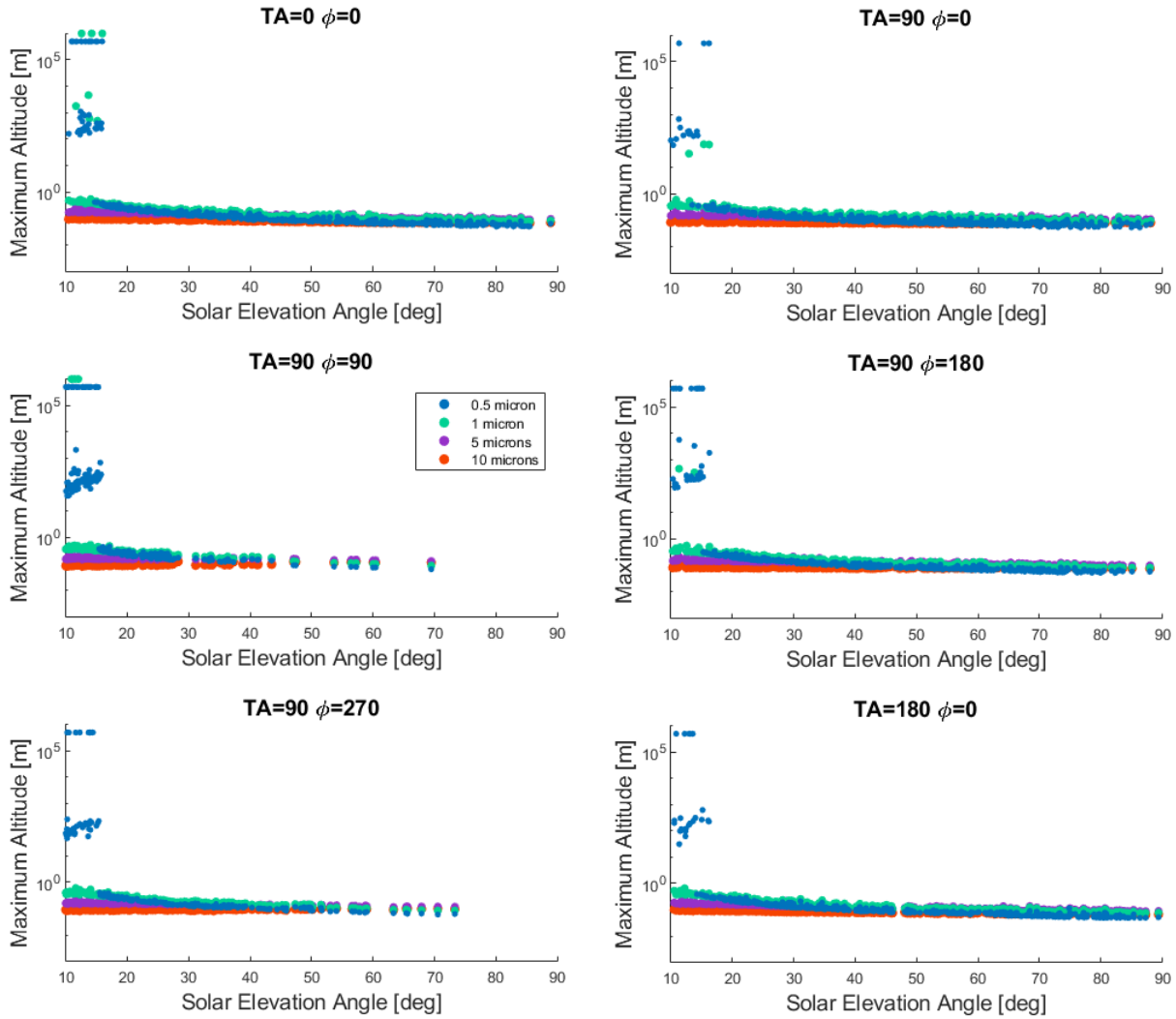

Figure 5.34: Maximum altitude reached as a function of initial solar elevation angle for dust grains lofting on Eros. Results shown for (a) TA = 0 deg and phi = 0 deg, (b) TA = 90 deg and phi = 0, (c) TA = 90 and phi = 90 deg, (d) TA = 90 deg and phi = 180 deg, (e) TA = 90 deg and phi = 270 deg, and (f) TA = 180 deg and phi = 0 deg. 0.5 micron grains are shown in blue, 1 micron grains in teal, 5 micron grains in purple, and 10 micron grains in orange. Escaped grains are plotted at 10^5 meters for visualization.

As mentioned previously, all the larger 5 and 10 micron dust grains reimpact the surface with no particle escapes. Overall, the 5- and 10-micron populations have average maximum altitudes of 14 centimeters and 8.7 centimeters, respectively. These populations of particles likely wouldn't be able to transport out of the deep craters on Eros. Reimpacting 1-micron grains reach an average maximum altitude of 28 meters below 16 degrees and 19

centimeters above 16 degrees. Several of these grains escape at low solar elevation angles, but most do not. A few 0.5-micron grains are able to escape under 16 degrees solar elevation angle; however most do not. Reimpacting 0.5-micron grains reach an average maximum altitude of 210 meters below 16 degrees and 1.3 meters above 15 degrees. These grains are highly mobile and would likely redistribute themselves into the gravitational lows on the surface of Eros where they would become trapped (such as Eros's large crater with a depth of 0.9 kilometers).

Overall, the smaller grains with average altitudes of 30-200 meters would likely have the ability to transport themselves easily into gravitational lows where they could be observed in dusted ponds. The larger grains only reach average altitudes of 9-14 centimeters and would most definitely be trapped in craters and other topographical depressions.

Next, we look at the distance traveled laterally by lofted dust grains as a function of solar elevation angle in Figure 5.35. Escaped particles are again plotted at 10^5 meters for visualization.

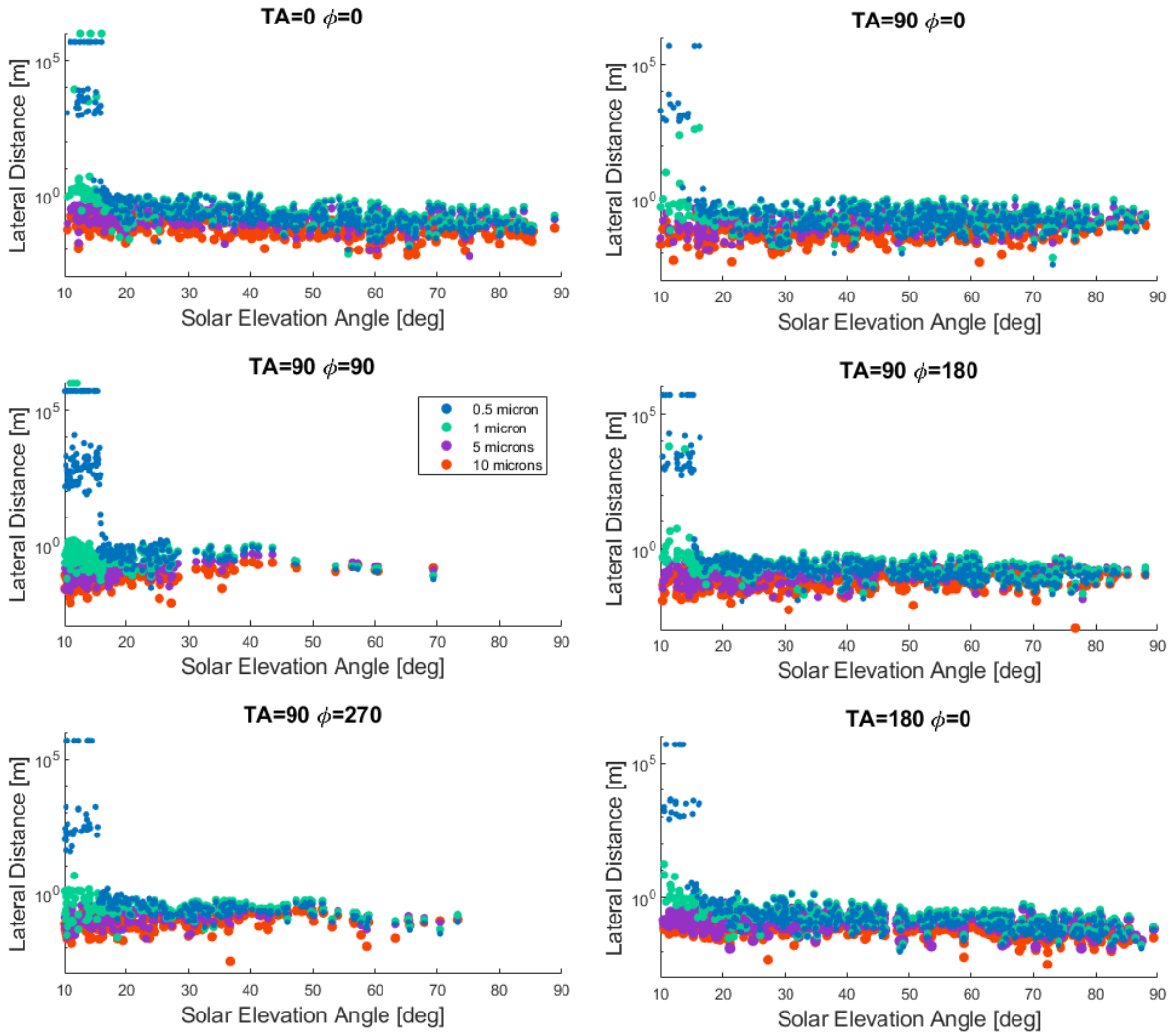

Figure 5.35: Lateral distance traveled as a function of initial solar elevation angle for dust grains lofting on Eros. Results shown for (a) TA = 0 deg and phi = 0 deg, (b) TA = 90 deg and phi = 0, (c) TA = 90 and phi = 90 deg, (d) TA = 90 deg and phi = 180 deg, (e) TA = 90 deg and phi = 270 deg, and (f) TA = 180 deg and phi = 0 deg. 0.5 micron grains are shown in blue, 1 micron grains in teal, 5 micron grains in purple, and 10 micron grains in orange. Escaped grains are plotted at 10^5 meters for visualization.

We see that reimpacting (all) 5 micron and 10-micron grains move an average lateral distance of 16 centimeters and 8.9 centimeters, respectively. These grains would not be able to escape craters on Eros with average depths of a few meters and would result in ponded deposits [38]. Reimpacting 1-micron grains move an average lateral distance of 113 meters below 15 degrees and 3.1 meters above 15 degrees. Reimpacting 0.5-micron grains

move an average lateral distance of 1649 meters below 15 degrees and 32 meters above 15 degrees. These smaller grains are much more mobile and easily transported across the small body surface and into gravitational lows. Overall, the same grains that were seen to escape on Itokawa and Ryugu are shown to remain on the surface of Eros and have motion limited by crater depths. This aligns with observations of a fine regolith-covered surface and ponded dust deposits on Eros [38].

5.4.4 Comparisons

When comparing the results of dust lofting on each body, we note the following key findings. Examining first the results of Itokawa and Ryugu, we find that the transition between particle escape to minimal surface motion appears to be quite steep as a function of grain size. Simply doubling the grain size cuts down mobility by a large factor. Thus, even if there are larger (~15 micron) grains on the surfaces of these bodies, they cannot move across the surface and accumulate in particular low gravity regions. In contrast, smaller grains (~1-5 microns) appear to loft and escape easily from the surfaces of these bodies. This may explain why we do not see ponded deposits of these particles on rubble-pile bodies such as Itokawa, Bennu, and Ryugu. Larger grains cannot transport large enough distances to accumulate, while smaller grains escape the body completely.

On Eros, these results change due to the primary body's increased size and mass. While a few of the smallest 0.5 micron grains are seen to escape, there is a sizeable fraction of mobile grains (>1 micron) that loft but don't easily escape the body. These grains are free to be transported, rearranged, and accumulated yet still trapped and restricted to the surface. These results may explain the ponded dust deposits we observe on Eros.

Finally, we note the correlation between dust particle size mobility and small body gravity. As the primary body increases in size and its surface gravity increases, the grain size of mobile dust populations decreases. This means that populations of grains with

high mobility on smaller bodies such as Itokawa and Ryugu will be less mobile on larger bodies such as Eros.

5.4.5 Implications

Overall, we find that dust grains electrostatically lofting from locations with lower solar elevation angles are more mobile. They reach higher altitudes, move larger lateral distances, and have higher escape rates. This implies that more hazardous dusty times of day are likely in the mornings and evenings. Mid-day would be better for near-surface exploration operations. There also appears to exist a transition point around 30 degrees solar elevation angle, below which grains are more mobile than above it. Solar radiation pressure can sweep these lower solar elevation particles farther distances and some to escape. On Eros we noted that this transition angle is shifted to 15 degrees, likely dependent on the body size (and indirectly on the slope of the surface). Both are concerned with the relative altitude particles can achieve away from the surface, enabling solar radiation pressure to sweep them farther from their initial lofting locations.

Itokawa's rough, boulder-rich surface is comprised of rubble ranging in size from millimeter to centimeter-sized particles up to 50 meter-sized boulders [13]. No fine regolith particles are observed on the surface. This aligns with the results of our simulation where smaller 5 micron grains experience a high escape rate, and both 5 micron and 10 micron grains are likely eliminated over the long timescale of asteroid evolution. Additionally, larger 15 micron grains do not escape but are also not able to travel large distances from their lofting locations. Thus, this population of dust cannot accumulate into gravity lows where they could be readily observed and identified. Reinforcing this idea, the larger 10 and 15 micron particles that reimpact the surface reach maximum altitudes which are lower than some of the larger boulders. This implies that these particles may be trapped in local

areas if they cannot overcome these larger features. Low potential regions exist near the neck and northern regions of the asteroid [13].

Ryugu's surface is dominated by large grains (> 1 centimeter) and boulders (< 40 meters). No large craters or fine regolith is observed. This aligns well with our simulation results where smaller 1 micron and 5-micron grains are seen to escape the body at lower solar elevation angles with escape rates of 23% and 32%, respectively. Over time scales of the body's evolution, these grains will be eliminated completely from the surface. Larger 10 micron particles are not able to escape the body and do not move large distances from their lofting locations. For reimpacting dust grains, overcoming boulders < 40 meters and even the larger grains would likely prove difficult. This implies, as was the case for Itokawa, that these larger particles are not very mobile and are not able to accumulate in areas of gravitational potential lows. Thus, this population of particles would not be easily observed on the surface as a result, which reinforces the observations of no dust deposits on Ryugu.

Eros's surface has a variety of features—from lineations such as ridges and grooves, to areas with a high density of boulders up to 100 meters across, to the smoother saddle area where impacts are less prevalent. Most strikingly, however, is that the surface appears to be covered in a fine grain regolith and ponded dust deposits dominate near the equator. Such observations are not seen on other asteroids such as Itokawa and Ryugu. From our simulations, we find that the smaller dust grains observed to escape from Itokawa and Ryugu appear to be trapped on Eros. This would seem to support the idea that larger bodies such as Eros have regolith covered surfaces, while smaller rubble-pile bodies such as Itokawa, Bennu, and Ryugu do not. Ponded crater depths are a few meters deep on Eros. From our results we find that reimpacting grains likely would be trapped by such features and would accumulate in these potential lows. From our analysis, we find that ponded dust deposits are possible on Eros because there exist populations of lofted dust

grains that are mobile without escaping and that become gravitationally trapped to accumulate on the surface.

5.6 Summary and Conclusions

Overall, in this chapter we have presented the results of several different studies that examine electrostatically-driven dust motion on small bodies in the Solar System.

In the first study, particles of various sizes at a range of locations on the surface of asteroid 1992SK were given an upward initial charge and velocity using experimental results from Wang et al. [51]. This initial launching velocity represents a force imparted to the grain from any number of exploration activities. Overall we found that 1) smaller particles more easily escape than larger particles, 2) larger particles reach greater altitudes but tend to return to the surface to create a dusty working environment, and 3) sunset may be a cleaner working area than sunrise because particles are able to escape more quickly and more frequently there. However, the charging rate of a dust grain and its relation to when and where on a body the dust grain lofts were not examined. This was investigated in later studies.

In the second study, we examined the same particles at the same surface locations but varied the initial charge until a nonzero lofting velocity was found. The effect of cohesion was not modeled in this simulation. Overall, we found that the charge required for dust lofting is dependent on the grain size and there is a range of charges over which lofting is possible. The most striking result, however, were the magnitudes of charges required for lofting, which were orders of magnitude larger than those provided in Wang et al. [51]. Thus, even without consideration to cohesion, some other grain-scale mechanism is needed to loft grains naturally from the surface of small bodies. This missing mechanism was provided by Zimmerman et al. [62] in the form of a grain-scale supercharging model that was examined in the third study.

In the third study, we surveyed dust lofting conditions and behavior on spherical bodies of different sizes and rotation periods. Cohesion was considered and grain-scale supercharging was used to determine grain initial conditions. Overall, we found that both faster rotation and smaller size of the primary body result in more particle loss events. Assuming that bodies such as Bennu and Ryugu underwent past period of rapid rotation, we would expect smaller dust grains to have been preferentially eliminated from their surfaces, as is consistent with observations of no fine regolith on these bodies today. Furthermore, we identified solar radiation pressure as a driving force in lofted dust grain behavior. Particle loss events in general tend to occur more frequently at lower solar elevation angles where solar radiation pressure carries these particles farther from the surface. Most interestingly, larger dust grains were seen to achieve higher altitudes and larger lateral distances (up to a point) than their smaller counterparts due to the stronger effect of solar radiation pressure on smaller grains.

In the final study, we extended the spherical results to survey dust lofting conditions and behavior on the complex shape models of Itokawa, Ryugu, and Eros. Cohesion was again considered, and grain-scale supercharging was used to determine initial conditions. Overall, we found that smaller dust grains (<5-10 microns) are preferentially lost on smaller rubble-pile asteroids such as Itokawa and Ryugu, while they remain trapped on the surface of larger bodies such as Eros, where ponded deposits of dust are observed. Additionally, we find that grains electrostatically lofted from locations with lower solar elevation angles are more mobile—reach higher altitudes, move larger lateral distances, and have higher escape rates—implying that local morning and evening are more dusty times of day. Regardless if dust is lofted naturally or disturbed artificially, this has implications for mission operations near the surface of small bodies.

Chapter 6

Conclusions and Future Work

This thesis investigates electrostatically-driven dust lofting and migration on small bodies in the Solar System. We put forth development of a small body environment model which is able to model the complex interactions that electrostatically-driven dust grains undergo in the near-surface region of small bodies. We investigated grain-scale supercharging models which are better able to predict the elevated grain charges and electric fields required to overcome both cohesion and gravity at the surface. We used these models to develop a method of bounding initial conditions such as grain charge, ejection velocity, and the maximum cohesion a given grain on a given body can electrostatically overcome. These bounds were used as initial conditions for a variety of numerical studies that simulated launched and lofted dust grain behavior within the small body environment. From these simulations, we found trends in dust grain motion and made predictions about the behaviors of different dust populations on the surfaces of various small bodies such as Itokawa, Bennu, Ryugu, and Eros. In this way, we were able to examine electrostatically-driven dust lofting and transport on various small bodies under a variety of surface conditions.

While the work in this thesis provides a novel framework from which to simulate and analyze electrostatically-driven dust grain behavior, there are a number of avenues for future work. The most significant ones are outlined below.

In this thesis, we solved for the cohesive strength a give dust grain could overcome given local surface and grain-scale supercharging conditions (at maximum gap electric

field). We used this cohesive strength to solve for the associated ejection velocity of a lofted dust grain and studied the subsequent behavior. In reality, a given asteroid surface is not expected to have a uniform value for cohesive strength, and in fact the cohesion that any surface particle feels will depend strongly on their shape and placement on the surface, the mechanisms that have distributed them to their current location, and other factors. Thus, a given asteroid surface may have a wide range of cohesions that apply to particles on the surface. Future work should investigate other cohesive strengths and the subsequent effect on lofted dust grain behavior.

Incorporation of higher resolution topography such as large boulders and deep craters could also prove useful in constraining dust transport across the surface of specific bodies. Here we used smooth facets to loft dust grains, but even a statistical study on an example patch of rougher terrain that includes larger features could provide more specific information on the limits of dust grain mobility on these surfaces.

Additionally, lofting angles other than normal to the surface should be examine. Here we examined force balance in the surface normal direction and assumed that dust motion would also occur along this same line. However, experimental work by Orger et al. [32] found that dust lofting angles have peak distribution at 45 degrees to the normal. Depending on the direction of ejection, the grain will either get a boost or a reduction in its initial speed. In general, we expect these to average out in three dimensions, but future work should include a more detail exploration to investigate this.

Future work should also include incorporation of more complete electric field and grain charging models, such as that presented in Nitter et al. [31]. A simpler model was used in this thesis for computational efficiency, but future simulations would benefit from using a non-monotonic potential profile, as well as incorporation of current contributions from solar wind ions, which were neglected in the model we used. Additionally, inclusion of

the tangential electric field would provide a more complete picture of electrostatically-driven dust motion in the near-surface region. Perhaps even a global solution to the electric field could be computed, saved, and sampled at each location along a grain's trajectory to account for both the surface normal and tangential fields simultaneously while using minimal computation.

Similarly, it is becoming increasingly important to understand and more accurately model the terminator and night side of a small body. Typically, the electrostatic force is set to zero once a particle passes into the shadowed region of the night side [7, 27]. A method similar to that formulated in this thesis could be used to determine grain-scale supercharging conditions on the nightside using secondary electron emission in place of photoemission. A nightside wake formulation of the potential field [40] with incorporation of a Debye sheath and grain charging given by [10] could be used to dynamically model grain behavior in this region. To date, a study like this has not be completed. A similar formulation applied to a crater- or boulder-scale simulation could also provide interesting insight into dust behavior in the vicinity of these surface features [59, 60]. Additionally, the terminator region is thought to be one of the most promising sites for lofting due to adjacent patches of lit and shadowed regions on the surface [8, 9, 50], and thus modeling this region and subsequent dust behavior should be examined in future work. The plasma sheath model C developed by Nitter et al. [31] could be used to model this region of low photoemission, along with grain charging in an unthermalized plasma.

Bibliography

[1] Barker, M. K., E. Mazarico, T. P. McClanahan, X. Sun, G. A. Neumann, D. E. Smith, M. T. Zuber, J. W. Head. 2019, *Journal of Geophysical Research: Planets*, 124: 2728-2744, "Searching for Lunar Horizon Glow with the Lunar Orbiter Laser Altimeter."

[2] Berg, O. E., F. F. Richardson, & H. Burton. 1973, *Apollo 17 preliminary science report*, Chapter 16: "Lunar Ejecta and Meteorites Experiment", NASA.

[3] Budenstein, P.P. 1980, IEEE Trans. Electr. Insul., EI-15(3): 225-240, "On the mechanism of dielectric breakdown of solids."

[4] Burns, J. A., P. L. Lamy, and S. Soter. 1979, *Icarus*, 40: 1-48, "Radiation Forces on Small Particles in the Solar System."

[5] Busch, M., S. J. Ostro, L. A. M. Benner, J. D. Giorgini, R. F. Jurgens, R. Rose, C. Magri, P. Pravec, D. J. Scheeres, S. B. Broschart. 2006, *Icarus*, 181: 145-155, "Radar and Optical Observations and Physical Modeling of Near-Earth Asteroid 10115 (1992 SK)."

[6] Carroll, A., N. Hood, R. Mike, X. Wang, H.-W. Hsu, M. Horányi. 2020, *Icarus*, 352: 113972, "Laboratory measurements of initial launch velocities of electrostatically lofted dust on airless planetary bodies."

[7] Colwell, J. E., A. A. S. Gulbis, M. Horányi, and S. Robertson. 2005, *Icarus*, 175: 159-169, "Dust transport in photoelectron layers and the formation of dust ponds on Eros."

[8] Criswell, D. R. & B. R. De. 1977, *Journal of Geophysical Research*, 82(7): 1005-1007, "Intense localized photoelectric charging in the lunar sunset terminator region: 2. supercharging at the progression of sunset."

[9] De, B. R. & D. R. Criswell. 1977, *Journal of Geophysical Research*, 82(7): 999-1004, "Intense localized photoelectric charging in the lunar sunset terminator region: 1. development of potentials and fields."

[10] Farrell, W. M., T.J. Stubbs, J.S. Halekas, R.M. Killen, G.T. Delory, M.R. Collier, and R.R.Vondrak. 2010, *Journal of Geophysical Research*, 115: E03004, "Anticipated electrical environment within permanently shadowed lunar craters."

[11] Feldman, P. D., D. A. Glenar, T. J. Stubbs, K. D. Retherford, G. R. Gladstone, P. F. Miles, T. K. Greathouse, D. E. Kaufmann, J. W. Parker, S. A. Stern. 2014, *Icarus*, 233: 106-113, "Upper limits for a lunar dust exosphere from far-ultraviolet spectroscopy by LRO/LAMP."

[12] Frederickson, A. R., D. B. Cotts, J. A. Wall, & F. L. Bouquet. 1986, AIAA, University of Michigan, New York, "Spacecraft Dielectric Material Properties and Spacecraft Charging."

[13] Fujiwara, A., J. Kawaguchi, D. K. Yeomans, M. Abe, T. Mukai, T. Okada, J. Saito, H. Yano, M. Yoshikawa, D. J. Scheeres, O. Barnouin-Jha, A. F. Cheng, H. Demura, R. W. Gaskell, N. Hirata, H. Ikeda, T. Kominato, H. Miyamoto, A. M. Nakamura, R. Nakamura, S. Sasaki, K. Uesugi. 2006, *Science*, 312:1330-1334, "The rubble-pile asteroid Itokawa as observed by Hayabusa."

[14] Glenar, D. A., T. J. Stubbs, J. E. McCoy, R. R. Vondrak. 2011, *Planetary and Space Science*, 59: 1695-1707, "A reanalysis of the Apollo light scattering observations, and implications for lunar exospheric dust."

[15] Glenar, D. A., T. J. Stubbs, J. M. Hahn, Y. Wang. 2014, *Journal of Geophysical Research: Planets*, 119: 2548-2567, "Search for a high-altitude lunar dust exosphere using Clementine navigational star tracker measurements."

[16] Grard, R. J. L. & J. K. E. Tunaley. 1971, *Journal of Geophysical Research*, 76(10): 2498-2505, "Photoelectron sheath near a planar probe in interplanetary space."

[17] Halekas, J. S., D. L. Mitchell, R. P. Lin, L. L. Hood, M. H. Acuña, A. B. Binder. 2002, *Geophysical Research Letters*, 29 (10): 1435, "Evidence for negative charging of the lunar surface in shadow."

[18] Halekas, J. S., R. P. Lin, D. L. Mitchell. 2003, *Geophysical Research Letters*, 30(21): 2117, "Inferring the scale height of the lunar nightside double layer."

[19] Hartzell, C. M. & D. J. Scheeres. 2011, *Planetary and Space Science*, 59: 1758-1768, "The role of cohesive forces in particle launching on the Moon and asteroids."

[20] Hartzell, C. M. & D. J. Scheeres. 2013, *Journal of Geophysical Research: Planets*, 118: 116-125, "Dynamics of levitating dust particles near asteroids and the Moon."

[21] Hartzell, C.M., X. Wang, D. J. Scheeres, & M. Horányi. 2013, *Geophysical Research Letters*, 40: 1038-1042, "Experimental demonstration of the role of cohesion in electrostatic dust lofting."

[22] Hartzell, C.M. 2019, *Icarus*, 333: 234-242, "Dynamics of 2D electrostatic dust levitation at asteroids."

[23] Hasegawa, S., T. G. Müller, K. Kawakami, T. Kasuga, T. Wada, Y. Ita, N. Takato, H. Terada, T. Fujiyoshi, M. Abe. 2008, *Astronomical Society of Japan*, 60: S399-S405, "Albedo, size, and surface characteristics of Hayabusa-2 sample-return target 162173 1999 JU3 from AKARI and Subaru observations."

[24] Havnes, O., C. K. Goertz, G. E. Morfill, E. Grun, & W. Ip. 1987, *Journal of Geophysical Research*, 92(A3): 2281-2287, "Dust charges, cloud potential, and instabilities in a dust cloud embedded in a plasma."

[25] Hirabayashi, M., E. Tatsumi, H. Miyamoto, G. Komatsu, S. Sugita, S. Watanabe, D.J. Scheeres, O. Barnouin, P. Michel, C. Honda, T. Michikami, Y. Cho, T. Morota, N. Hirata, N. Hirata, N. Sakatani, S. Schwartz, R. Honda, Y. Yokota, S. Kameda, H. Suzuki, T. Kouyama, M. Hayakawa, M. Matsuoka, K. Yoshioka, K. Ogawa, H. Sawada, M. Yoshikawa and Y. Tsuda. 2019*, The Astrophysical Journal Letters*, 874: L10, "The western bulge of 162173 Ryugu formed as a result of a rotationally driven deformation process."

[26] Hood, N., A. Carroll, R. Mike, X. Wang, J. Schwan, H.W. Hsu, and M. Horányi.2018, *Geophysical Research Letters*, 45:13206-13212, "Laboratory investigation of rate of electrostatic dust lofting over time on airless planetary bodies."

[27] Hughes, A. L. H., J.E. Colwell, & A. W. DeWolfe. 2008, *Icarus*, 195: 630-648, "Electrostatic dust transport on Eros: 3D simulations of pond formation."

[28] Lauretta, D.S., D. DellaGiustina, C. Bennett, D. Golish, K. Becker, S. Balram-Knutson, O. Barnouin, T. Becker, W. Bottke, W. Boynton, H. Campins, B. Clark, H. Connolly, Jr., C. d'Aubigny, J. Dworkin, J. Emery, H. Enos, V. Hamilton, C. Hergenrother, E. Howell, M. Nolan, B. Rizk, H. Roper, D.J. Scheeres, P. Smith, K. Walsh, C. Wolner, M. Izawa, H. Kaplan. 2019, *Nature*, 568: 55-60, "The Unexpected Surface of Asteroid (101955) Bennu."

[29] Lee, P. August 1996, *Icarus*, 124: 181-194, "Dust levitation on asteroids."

[30] Michikami, T., C. Honda, H. Miyamoto, M. Hirabayashi, A. Hagermann, T. Irie, K. Nomura, C. M. Ernst, M. Kawamura, K. Sugimoto, E. Tatsumi, T. Morota, N. Hirata, T. Noguchi, Y. Cho, S. Kameda, T. Kouyama, Y. Yokota, R. Noguchi, M. Hayakawa, N. Hirata, R. Honda, M. Matsuoka, N. Sakatani, H. Suzuki, M. Yamada, K. Yoshioka, H. Sawada, R. Hemmi, H. Kikuchi, K. Ogawa, S. Watanabe, S. Tanaka, M. Yoshikawa, Y. Tsuda, S. Sugita. 2019, *Icarus*, 331:179-191, "Boulder size and shape distributions on asteroid Ryugu."

[31] Nitter, T., O. Havnes, & F. Melandso. 1998, *Journal of Geophysical Research*, 103: 6605-6620, "Levitation and dynamics of charged dust in the photoelectron sheath above surfaces in space."

[32] Orger, N. C., K. Toyoda, H. Masui, M. Cho. 2021, *Advances in Space Research*, 68: 1568-1581, "Experimental investigation on particle size and launch angle distribution of lofted dust particles by electrostatic forces."

[33] Piquette, M., M. Horányi. 2017, *Icarus*, 291: 65-74, "The effect of asymmetric surface topography on dust dynamics on airless bodies."

[34] Poppe, A., and M. Horányi. 2010, *Journal of Geophysical Research*, 115: A08106, "Simulations of the photoelectron sheath and dust levitation on the lunar surface."

[35] Poppe, A., J. S. Halekas, M. Horányi. 2011, *Geophysical Research Letters*, 38: L02103, "Negative potentials above the dayside lunar surface in the terrestrial plasma sheet: evidence of non-monotonic potentials."

[36] Poppe, A., M. Piquette, A. Likhanskii, M. Horányi. 2012, *Icarus*, 221: 135-146, "The effect of surface topography on the lunar photoelectron sheath and electrostatic dust transport."

[37] Rennilson, J. J. & D. R. Criswell. 1974, *The Moon*, 10: 121-142, "Surveyor observations of Lunar Horizon Glow."

[38] Robinson, M. S., P. C. Thomas, J. Veverka, S. L. Murchie, & B. Carcich. 2001, *Nature*, 413: 396-400, "The nature of ponded deposits on Eros."

[39] Saito, J., H. Miyamoto, R. Nakamura, M. Ishiguro, T. Michikami, A. M. Nakamura, H. Demura, S. Sasaki, N. Hirata, C. Honda, A. Yamamoto, Y. Yokota, T. Fuse, F. Yoshida, D. J. Tholen, R. W. Gaskell, T. Hashimoto, T. Kubota, Y. Higuchi, T. Nakamura, P. Smith, K. Hiraoka, T. Honda, S. Kobayashi, M. Furuya, N. Matsumoto,

E. Nemoto, A. Yukishita, K. Kitazato, B. Dermawan, A. Sogame, J. Terazono, C. Shinohara, H. Akiyama. 2006, *Science*, 312:1341-1344, "Detailed images of asteroid 25143 Itokawa from Hayabusa."

[40] Samir, U., K.H. Wright, and N.H. Stone. 1983, *Geophysics and Space Physics*: 21(7):1631-1646, "The expansion of a plasma into a vacuum: basic phenomena and processes and applications to space plasma physics."

[41] Sánchez, P. & D. J. Scheeres. 2014, *Meteoritics and Planetary Science*, 49(5): 788-811, "The strength of regolith and rubble pile asteroids."

[42] Scheeres, D. J., C. M. Hartzell, P. Sánchez, & M. Swift. 2010, *Icarus*, 210: 968-984, "Scaling forces to asteroid surfaces: the role of cohesion."

[43] Sheridan, T. E., J. Goree, Y.T. Chiu, R.L. Rairden, and J.A. Kiessling. 1992, *Journal of Geophysical Research*, 97(A3):2935-2942, "Observation of dust shedding from material bodies in a plasma."

[44] Schwan, J., X. Wang, H. W. Hsu, E. Grun, & M. Horányi. 2017, *Geophysical Research Letters*, 44: 3059-3065, "The charge state of electrostatically transported dust on regolith surfaces."

[45] Sickafoose, A. A. and J.E. Colwell. 2002, *Journal of Geophysical Research*, 107(A11):1408, "Experimental levitation of dust grains in a plasma sheath."

[46] Smith, D. E., M. T. Zuber, G. A. Neumann, F. G. Lemoine. 1997, *Journal of Geophysical Research*, 102(E1):1591-1611, "Topography of the Moon from the Clementine lidar."

[47] Sørensen, J., D. Rodgers, K. Ryden, P. Latham, G. Wrenn, L. Levy, & G. Panabiere. 2000, 5th European Conference on Radiation and Its Effects on Components and Systems, IEEE: 27-33, Fontevraud, France, "ESA's tools for internal charging."

[48] Vallado, D. A. 2013, *Fundamentals of Astrodynamics and Applications*, Chapter 8.6.4, 4th Ed.: 578-582, Microcosm Press, "Solar-radiation pressure."

[49] Veverka, J., M. Robinson, P. Thomas, S. Murchie, J. F. Bell III, N. Izenberg, C. Chapman, A. Harch, M. Bell, B. Carchich, A. Cheng, B. Clark, D. Domingue, D. Dunham, R. Farquhar, M. J. Gaffey, E. Hawkins, J. Joseph, R. Kirk, H. Li, P. Lucey, M. Malin, P. Martin, L. McFadden, W.J. Merline, J. K. Miller, W. M. Owen Jr., C. Peterson, L. Prockter, J. Warren, D. Wellnitz, B. G. Williams, D. K. Yeomans. 2000, *Science*, 289:2088-2097, "NEAR at Eros: Imaging and Spectral Results."

[50] Wang, X., M. Horányi, Z. Sternovsky, S. Robertson, & G. Morfill. 2007, *Geophysical Research Letters*, 34: L16104, "A laboratory model of the lunar surface potential near boundaries between sunlit and shadowed regions."

[51] Wang, X., J. Schwan, H. W. Hsu, E. Grun, & M. Horányi. 2016, *Geophysical Research Letters*, 43: 6103-6110, "Dust charging and transport on airless planetary bodies."

[52] Watanabe, S., M. Hirabayashi, N. Hirata, N. Hirata, R. Noguchi, Y. Shimaki, H. Ikeda, E. Tatsumi, M. Yoshikawa, S. Kikuchi, H. Yabuta, T. Nakamura, S. Tachibana, Y. Ishihara, T. Morota, K. Kitazato, N. Sakatani, K. Matsumoto, K. Wada, H. Senshu, C. Honda, T. Michikami, H. Takeuchi, T. Kouyama, R. Honda, S. Kameda, T. Fuse, H. Miyamoto, G. Komatsu, S. Sugita, T. Okada, N. Namiki, M. Arakawa, M. Ishiguro, M. Abe, R. Gaskell, E. Palmer, O. S. Barnouin, P. Michel, A. S. French, J. W. McMahon,

D. J. Scheeres, P. A. Abell, Y. Yamamoto, S. Tanaka, K. Shirai, M. Matsuoka, M. Yamada, Y. Yokota, H. Suzuki, K. Yoshioka, Y. Cho, S. Tanaka, N. Nishikawa, T. Sugiyama, H. Kikuchi, R. Hemmi, T. Yamaguchi, N. Ogawa, G. Ono, Y. Mimasu, K. Yoshikawa, T. Takahashi, Y. Takei, A. Fujii, C. Hirose, T. Iwata, M. Hayakawa, S. Hosoda, O. Mori, H. Sawada, T. Shimada, S. Soldini, H. Yano, R. Tsukizaki, M. Ozaki, Y. Iijima, K. Ogawa, M. Fujimoto, T.-M. Ho, A. Moussi, R. Jaumann, J.-P. Bibring, C. Krause, F. Terui, T. Saiki, S. Nakazawa, Y. Tsuda. 2019, *Science*, 364: 268-272, "Hayabusa2 arrives at the carbonaceous asteroid 162173 Ryugu – A spinning top-shaped rubble pile."

[53] Werner, R. & D. Scheeres. 1997*, Celestial Mechanics and Dynamical Astronomy*, 65: 313-344, "Exterior gravitation of a polyhedron derived and compared with harmonic and mascon gravitation representations of asteroid 4769 Castalia."

[54] Wieczorek, M. A., B. L. Jolliff, A. Khan, M. E. Pritchard, B. P. Weiss, J. G. Williams, L. L. Hood, K. Righter, C. R. Neal, C. K. Shearer, I. S. McCallum, S. Tompkins, B. R. Hawke, C. Peterson, J. J. Gillis, B. Bussey. 2006, *Reviews in Mineralogy and Geochemistry*, 60:221-364, "The constitution and structure of the lunar interior."

[55] Willis, R.F., M. Anderegg, B. Feuerbacher, B. Fitton. 1973, *Photon and Particle Interaction with Surfaces in Space*, 369-387, Dordrecht Reidel, "Photoemission and secondary electron emission from lunar surface material."

[56] Xie, L., X. Zhang, L. Li, B. Zhou, Y. Zhang, Q. Yan, Y. Feng, D. Guo, S. Yu. 2020, *Geophysical Research Letters*, 27, "Lunar Dust Fountain Observed Near Twilight Craters."

[57] Xin, X., D. J. Scheeres, & X. Hou. 2016, *Celestial Mechanics and Dynamical Astronomy*, 126: 405-432, "Forced periodic motions by solar radiation pressure around uniformly rotating asteroids."

[58] Yeomans, D. K., P. G. Antreasian, J.-P. Barriot, S. R. Chesley, D. W. Dunham, R. W. Farquhar, J. D. Giorgini, C. E. Helfrich, A. S. Konopliv, J. V. McAdams, J. K. Miller, W. M. Owen Jr., D. J. Scheeres, P.C. Thomas, J. Veverka, B. G. Williams. 2000, *Science*, 289:2085-2088, "Radio science results during the NEAR-Shoemaker spacecraft rendezvous with Eros."

[59] Zimmerman, M. I., W. M. Farrell, T. J. Stubbs, J. S. Halekas, T. L. Jackson. 2011, *Geophysical Research Letters*, 38: L19202, "Solar wind access to lunar polar craters: feedback between surface charging and plasma expansion."

[60] Zimmerman, M. I., T. L. Jackson, W. M. Farrell, T. J. Stubbs. 2012, *Journal of Geophysical Research*, 117: E00K03, "Plasma wake simulations and object charging in a shadowed lunar crater during a solar storm."

[61] Zimmerman, M. I., W. M. Farrell, A. R. Poppe. 2014, *Icarus*, 238: 77-85, "Grid-free 2D plasma simulations of the complex interaction between the solar wind and small, near-Earth asteroids."

[62] Zimmerman, M. I., W. M. Farrell, C. M. Hartzell, X. Wang, M. Horányi, D. M. Hurley, & K. Hibbitts. 2016, *Journal of Geophysical Research: Planets*, 121:2150-2165, "Grain-scale supercharging and breakdown on airless regoliths."

[63] Zook, H. A. & J. E. McCoy. 1991, *Geophysical Research Letters*, 18(11): 2117-2120, "Large scale lunar horizon glow and a high altitude lunar dust exosphere."

[64] Zuber, M. T., D. E. Smith, A. F. Cheng, J. B. Garvin, O. Aharonson, T. D. Cole, P. J. Dunn, Y. Guo, F. G. Lemoine, G. A. Neumann, D. D. Rowlands, M. H. Torrence. 2000, *Science*, 289:2097-2101, "The shape of 433 Eros from the NEAR-Shoemaker Laser Rangefinder."